Spring 5-26-2017

The Investigation and Characterization of the Reaction of 2-Methylfuran and 2-Methyl-3-Buten-2-Ol with O(3P) and the Photodissociation of Xylyl Bromide Isomers

Yasmin Fathi
University of San Francisco, y.fathi92@yahoo.com

The Investigation and Characterization of the Reaction of 2-Methylfuran and 2-Methyl-3-Buten-2-Ol with O(^{3}P) and the Photodissociation of Xylyl Bromide Isomers

A Thesis presented to the Faculty of the

Department of Chemistry at the

University of San Francisco

in partial fulfillment of the requirements for the

Degree of Master of Science in Chemistry

Written by

Yasmin Fathi

Bachelor of Science in Biochemistry
Sonoma State University

05/26/2017

The Investigation and Characterization of the Reaction of 2-Methylfuran and 2-Methyl-3-Buten-2-Ol with O(^{3}P) and the Photodissociation of Xylyl Bromide Isomers

Thesis written by Yasmin Fathi

This thesis is written under the guidance of Faculty Advisory Committee,
and approved by all its members, has been accepted in
partial fulfillment of the requirements of the degree of

**Master of Science in Chemistry
at
the University of San Francisco**

Thesis Committee

Giovanni Meloni, Ph.D.
Research Advisor

Ryan West, Ph.D.
Assistant Professor

Janet Yang, Ph.D.
Assistant Professor

Marcelo Camperi, Ph.D.
Dean, College of Arts and Sciences

Acknowledgements

As I encompassed my journey as a graduate student at the University of San Francisco, I never imagined learning as much as I have, specifically in the field of Physical Chemistry. I always liked research, but my passion has been teaching and it was the main reason I went to further my education. Little did I know, being a part of Dr. Giovanni Meloni's research group would simply change my perspective. The last two years, my passion for teaching has grown even more and it is something I enjoy the most. However, the research I have done has really sparked my interest to becoming a scientist. The last two years I have gained an immense amount of research experience and I extremely grateful to Dr. Giovanni Meloni for giving me the opportunity to work in his research lab, be his teaching assistant, and give me the role of mentoring undergraduate research students through research. These opportunities have really shaped me as a future scientist. I would also like to thank the collaborators at the Paul Scherrer Institute in Villigen, Switzerland and University of Pacific for their guidance and efforts in the PEPICO experiments.

What has made the last two years such a growing experience was the wonderful Chemistry Department at USF. A sincere thank you to my Thesis committee, Dr. Ryan West and Dr. Janet Yang, for taking the time to help guide me and put resourceful inputs into my thesis. A special thank you to Dr. Lawrence Margerum for further growing my passion and teaching me even more about how to help students critically think. I would like to also thank Deidre Shymanski, for always helping me and answering any questions I had. Thank you to this wonderful chemistry department for two wonderful growing years.

I would like to sincerely and immensely thank my family for their constant love and encouragement throughout my entire academic experience. My parents and sister especially have really helped guide me and have been a constant support system throughout the last two years. Without them, I would not have made it and I truly thank them for everything. A special thank you to my best friend Niki, who has always encouraged me and fueled the passion I had for teaching and learning even more. A big thank you to my research lab for their collaboration and positive support during stressful times and my fellow graduate students.

Table of Contents

6. Photoionization and Photodissocation of Xylyl (Methylbenzyl) Bromide Radicals using VUV
Synchrotron Radiation

Abstract

This thesis has studied the oxidation behavior of different biofuels or additives, 2-methyl-3-buten-2-ol and 2-methylfuran, in combustion experiments at the Chemical Dynamics Beamline held at the Advanced Light Source of the Lawrence Berkley National Laboratory. The oxidation of these fuels were initiated through $O(^3P)$ and the combustion experiments were analyzed using a multiplexed chemical kinetics photoionization mass spectrometer with tunable synchrotron radiation. Products of the different reactions were identified using kinetic profiles and further characterized using the photoionization spectra. The amount of each species was calculated using branching fractions.

Additionally, the unimolecular dissociation of the xylyl bromide isomers was studied using imaging and double imaging photoelectron photoion coincidence spectroscopy to obtain accurate thermochemical data. These experiments were conducted using the Swiss Light Source held at the Paul Scherrer Institute in Villigen, Switzerland.

The importance of biofuels, fuel additives, and aromatic hydrocarbons is discussed in detail in Chapter 1 of this thesis. Further, the specific experimental components of the beamlines used at the ALS and the SLS are thoroughly explained in Chapter 2. The theory behind the experiments and the computational methods to analyze the substantial experimental findings from both experimental apparatuses are explained in Chapter 3. The two combustion systems, 2-methyl-3-buten-2-ol and 2-methylfuran with $O(^3P)$ are presented in Chapter 4 and 5. Lastly, the photodissociation dynamics of the xylyl bromide isomers is presented in Chapter 6, where a specific program, miniPEPICO, is used to determine the accurate appearance energy of the daughter ion and to calculate thermochemical data.

Chapter 1- Introduction

1.1 Climate Change and Greenhouse Gas Emission

To this day, the Earth's temperature is constantly rising. According to the Environmental Protection Agency (EPA), within the past century the planet has warmed up by 1.5 ^{0}F.[1] Due to these statistics, researchers of the EPA have estimated another rise in the Earth's temperature of around 0.5-8.6 ^{0}F over the next hundred years.[1] This ongoing rise in temperature has a direct effect on the climate, thus harming the environment; for instance, the oceans become more acidic, some areas see less rainfall resulting in droughts, some areas see increased rainfall resulting in flooding.[2] When CO_2 is continually pumped into the atmosphere, some leaks into the ocean dropping the overall pH therefore carbonate concentration begins to acidify the ocean.[2] The ocean absorbs 30% of CO_2 emissions caused from human activity and about 85% over a long period of time, as water and air mix at the ocean's surface.[2] Due to the use of fossil fuels, humans are acidifying the ocean and primarily changing its extremely delicate geochemical balance. Global warming is therefore directly related to climate change.

One of the main sources that causes the climate to continuously change is the release of greenhouse gases.[3] Although, greenhouse gases are essential to a controlled climate temperature, the accumulation of the gases can be detrimental to the climate over a long period of time. In the norm, the release of greenhouse gases run in a cycle; light absorbed from the sun heats up the surface of the Earth, from which some light is reflected back as infrared radiation in order to cool the surface back again.[4] This cycle (Figure 1-1) keeps the temperature of the Earth's surface roughly constant, not too cold and not too hot. However, the increase of greenhouse gases disturb this cycle from occurring at a comfortable and safe rate.[4] Levels of greenhouse gases are determined through sources and sinks, which are processes that, either destroy or create greenhouse gases.[5] Specifically, human activity introduces new sources or the activity that interferes with natural sinks.[5]
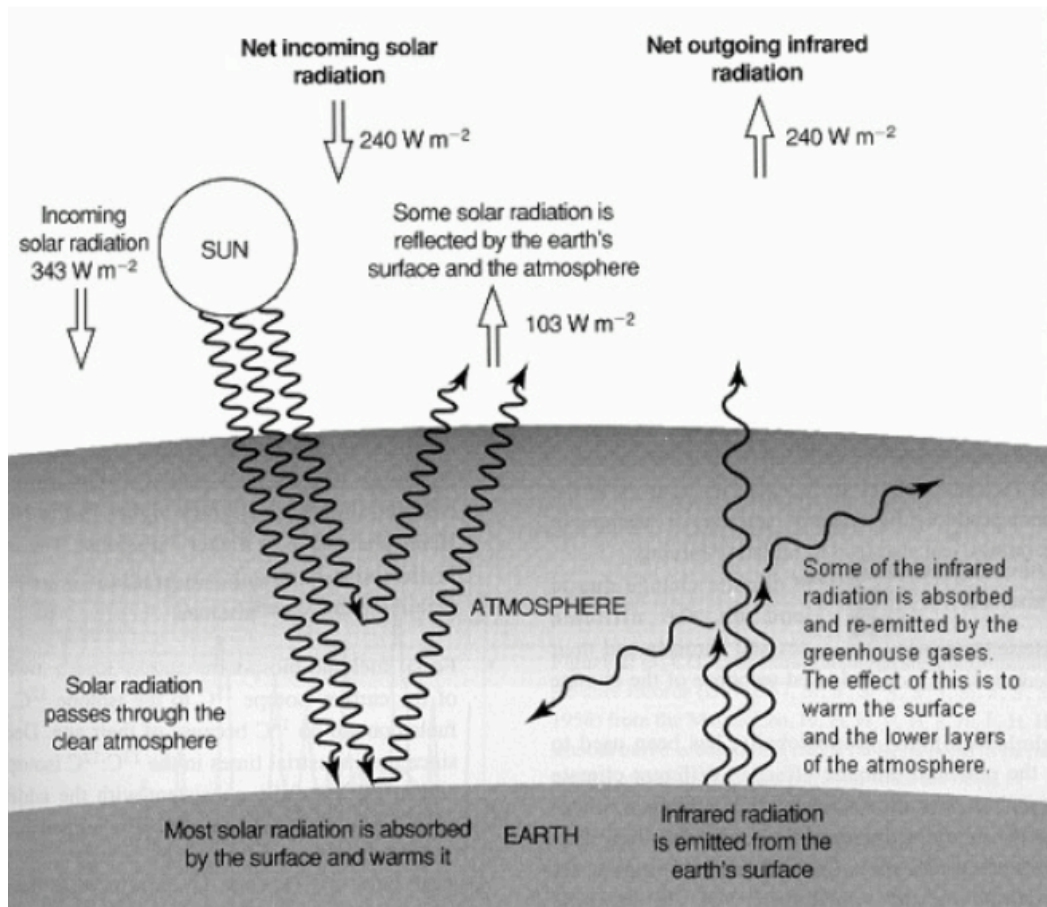
Figure 1-1. A schematic diagram showing the cycle of the global long-term radiative balance of the atmosphere from the light absorbed by the sun.[5]

The major greenhouse gases that accumulate in the atmosphere are: carbon dioxide (CO_2), methane (CH_4), nitrous oxide (N_2O), chlorofluorocarbons (CFCs), and ozone (O_3).[5] When more and more greenhouse gases are released in the atmosphere, the heat given off from the sun becomes "trapped" in the atmosphere. The accumulation of greenhouse gases does not allow for the infrared radiation to be reflected back.[4] This keeps all of the heat within the Earth's surface and thus drastically increases its temperature.[4] The United States Environmental Protection agency reported the amount of greenhouse gases emitted in 2014, Figure 1.[6] The major greenhouse gas emitted into the atmosphere is CO_2, mainly due to the burning of fossil fuels such as coal, natural gases, and oil.[6]
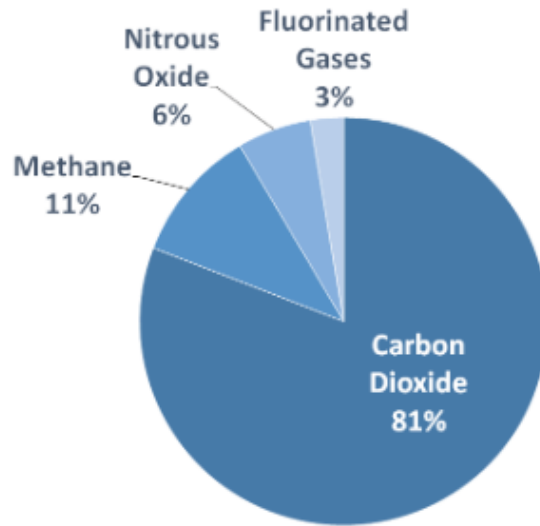
Figure 1-2. EPA report of total US Greenhouse Gas Emissions in 2014.[6]

1.2 Fossil Fuels

The primary source of the excessive release of greenhouse gases throughout the past century is due to human activity, specifically the burning of fossil fuels (coal, natural gas, petroleum, bitumen). To this day, the burning of fossil fuels is used as the main form of energy for electricity and transportation. As visualized in Figure 1-3, the primary source contributing to the release of greenhouse gases into the atmosphere comes from electricity production.[7] The EPA reports that around 67% of the electricity used in everyday life come directly from the burning of fossil fuels. Leading close behind is transportation, where almost 90% of the fuel used is petroleum-based (gasoline and diesel).[7] The combustion of fossil fuels itself releases nitric oxides (NO_x), volatile organic compounds (VOCs), nitrogen dioxide (NO_2), carbon dioxide (CO_2), and soot. The other primary sources are also related to the burning of fossil fuels, however, they do not have a large contribution.[7]
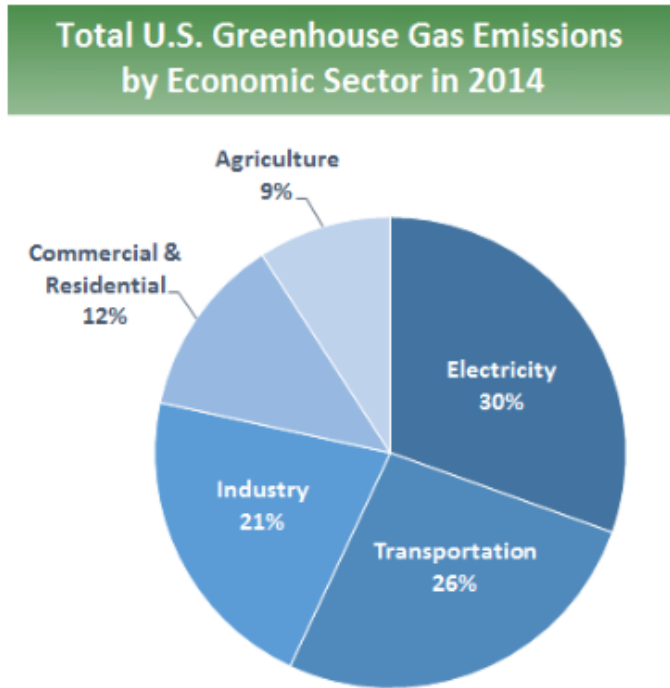
Figure 1-3. Total contribution of primary sources of greenhouse gas emissions in 2014.[7]

Fossil fuels are made from the remains of once living organisms and are not readily available; they take centuries to form. The three types of fossil fuels burned for energy are coal, oil, and natural gases.[8] Once these fossil fuels are burned, power plants convert this energy into electricity used in everyday life. In the past, fossil fuels were more available, however, nowadays they are running out of supply, becoming a serious threat to producing overall needed electricity.[8]

Another harmful emitted class of substances is particulate matter (PM), which has been found to cause severe health problems, such as respiratory and cardiovascular diseases.[9] NO_x poses high risks in human health as well, such as respiratory infection, airway resistance in asthmatics and decreases in pulmonary function.[10,11,12] Due to these harmful effects, for example the state of New England has passed on regulations forcing many different facilities to reduce overall NO_x emissions through modifying the combustion process and installing air pollution control equipment.[13] Additionally, gasoline itself is made of organic compounds resulting from the distillation of petroleum (a form of fossil fuels) very harmful to the environment. In 2015 researchers found that 1.1 billion metric tons of CO_2 in the United States were released into the atmosphere from combustion of transportation.[14]

1.3 Combustion

Due to the continuous increase in the warming of the Earth's climate and emission of hazardous greenhouse gases, researchers have been trying to find ways to incorporate renewable energy and lessen the overall use for the burning of fossil fuels. Combustion is a series of exothermic chemical reactions occurring between an oxidant and some type of fuel. These chains of reactions consist of molecular bond breaking, converting reactants to products, and thus releasing heat into the atmosphere. Around 90% of the energy needed to support everyday life comes from combustion. In a perfect world, when automobiles are ignited, the ideal combustion of hydrocarbons should only release carbon dioxide (CO_2), water (H_2O), and heat, seen in equation 1.

$$\text{Fuel (hydrocarbons)} + O_2 \rightarrow xCO_2 + yH_2O + \text{Heat} \tag{1}$$
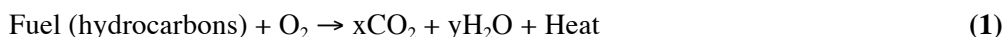
However, the combustion of natural gases actually releases many different species (see Fig. 1-4 below for the combustion of methane). Combustion of hydrocarbons is initiated through the abstraction of hydrogen atoms. In most cases, incomplete combustion causes byproducts, intermediates, and polycyclic aromatic hydrocarbon (PAHs) are formed and released into the atmosphere. The OH radical and $O(^3P)$ radical play essential roles in the oxidation process occurring throughout combustion. The reaction of $O(^3P)$ with two biofuels is studied in this thesis.
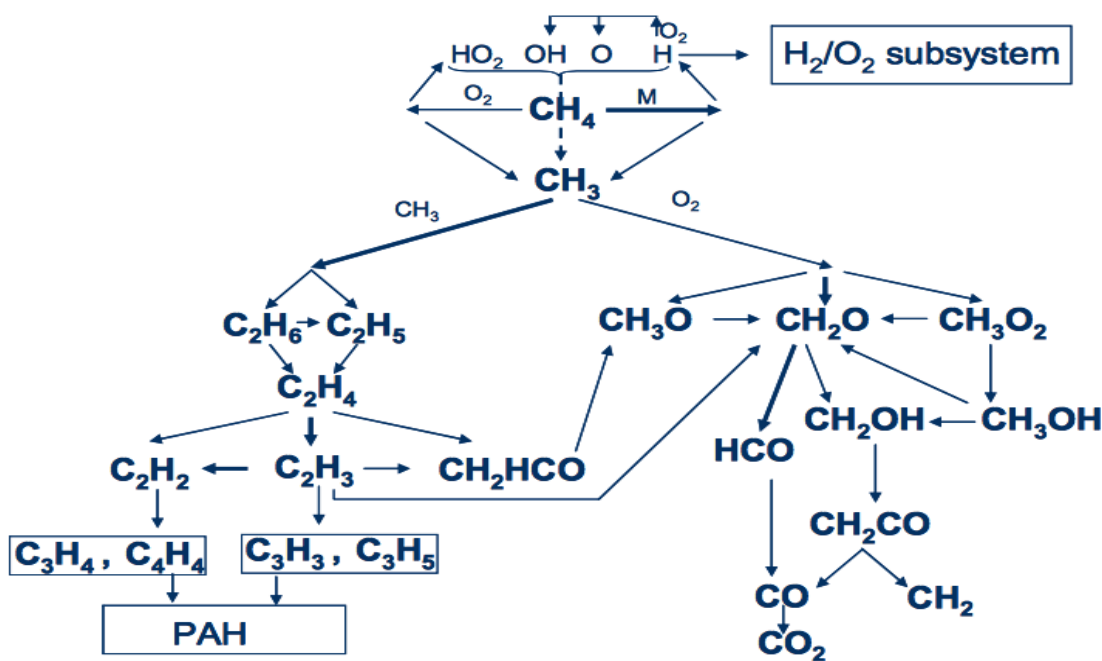
Figure 1-4. Schematic of a mechanism forming throughout combustion of methane at room temperature.[15]

The intermediates and byproducts vary with the fuel itself as well as the engine. Most common engines used for transportation are powered by gasoline or diesel. Most engines consist of similar parts, such as an ignition source (happens with a spark or a resistor) and a combustion chamber (consisting of cylinders). In all engines there is one point of ignition with one propagation front. Engine knocking occurs when there is incomplete combustion; unburnt gases are expanded therefore autoigniting the propagation front,[16] damaging the engine. For this reason, the amount of air and fuel mixture has to be stoichiometrically feasible and the compression has to have a ratio of 10:1 to avoid any potential engine knocking from occurring.[17] This ratio is common in gasoline engines, whereas diesel engines have a larger compression ratio of 18:1 contributing to higher fuel efficiency.[18-19] Also, a major benefit of diesel engines is less unburnt hydrocarbon production and release of carbon monoxide gas. However, PM, soot, and NO_x emissions are still in high occurrence.[20]

Comparable to the benefits of diesel engines are homogeneous charged compression ignition (HCCI) engines with higher efficiencies (Figure 1-5).[21] What makes these engines more attractive are lower emissions of PM and NO_x. They can be described as a combination of spark ignition gasoline engines and compressed ignition diesel engines.[22] In contrast with other engines, the HCCI engines does not use a spark to ignite, yet it is ignited through accurate timing of the reaction of air and fuel, auto-ignition of multiple sites under high temperature, 1000–2800 K, and high pressure, 40-140 MPa. In this engine, autoignition occurs at multiple sites at the same time forcing the reaction mixture (air and fuel) to burn simultaneously. However, the process is hard to control. In order to understand the function of the HCCI engine, researchers have been studying the control of ignition and combustion, specifically the timing of each, hydrocarbon emissions and performance of a larger load of different mixtures.
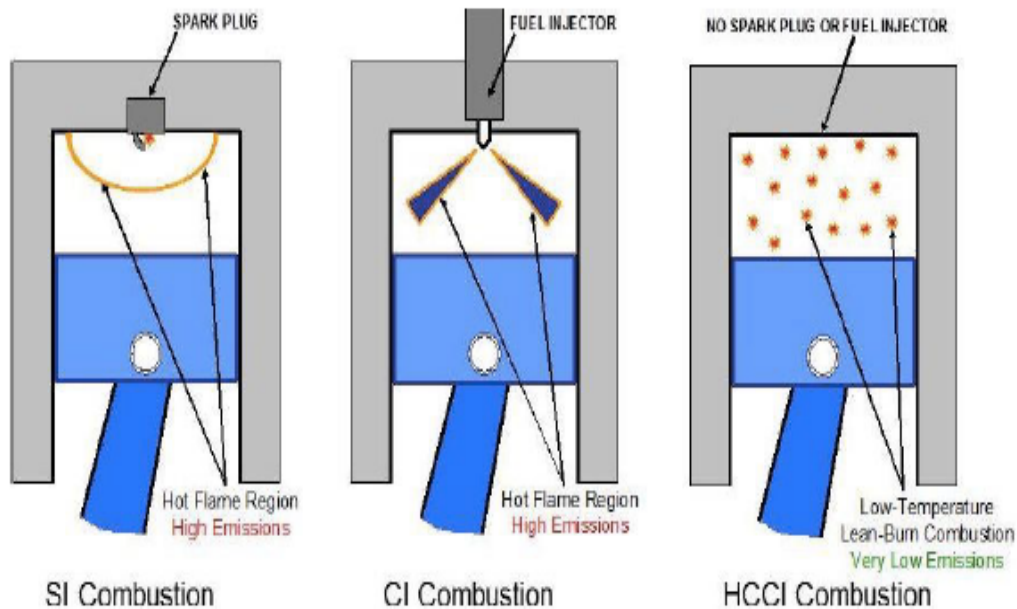
Figure 1-5. Diagram expressing the differences between SI, CI, and HCCI engines where it is visible that HCCI engine has several ignition points not just a single one.[23]

1.4 Biofuels and Fuel Additives

The demand for energy is huge; therefore, in the last few years, great research efforts have been delegated to find renewable sources of energy. Some of the reliable, renewable energy sources are biofuels, wind, geothermal, and solar energy. Biofuels and fuel additives have increasingly become of interest due to their high octane numbers, which have a direct impact on decreasing any chance of engine knocking. In particular, oxygenated fuel additives have the potential to improve the fuel mixture, providing fuel with properties further lessening the chances of engine knocking. Engine performance is directly related to the combustion speed of a particular fuel or fuel blend as well as pollutant emission. This speed is represented by its cetane number (CN); the higher the number the faster the ignition of the engine upon fuel injection. Often, different fuel additives are added to fuel to diminish the undesirable effects that the burning of fossil fuels causes to the environment, especially those with ignition delay.

In general, biofuels are interesting because they are derived from natural plant biomass and with low sulfur, nitrogen, and more oxygen content.[24] For instance, different known types of biofuels are biodiesel, bioethanol, biogas, biosynthetic gas (bio-syngas), bio-oil, bio-char, and bio hydrogen.[25] Most fossil fuels essentially have zero oxygen content, whereas biofuels are biodegradable and have 10-45% oxygen content offering a cleaner burning compared to petroleum based fuels.[26] These

8

properties help reduce the emissions of hazardous gases such as sulfur oxides (SO_x), carbon dioxide (CO_2),[27] and nitrogen oxides (NO_x).[28] Biofuels can be derived using many different techniques. Sugar cane or starch (corn or maize) can be fermented to produce ethanol that is often used as a fuel.[29] Plant oils (soybean or algae) can be burned directly in a diesel engine or blended with petroleum to make biodiesel.[29] Wood can also be burned into solid fuels.[29] Another one way of making biofuels is transesterfication, which is shown in Figure 1-6 below.
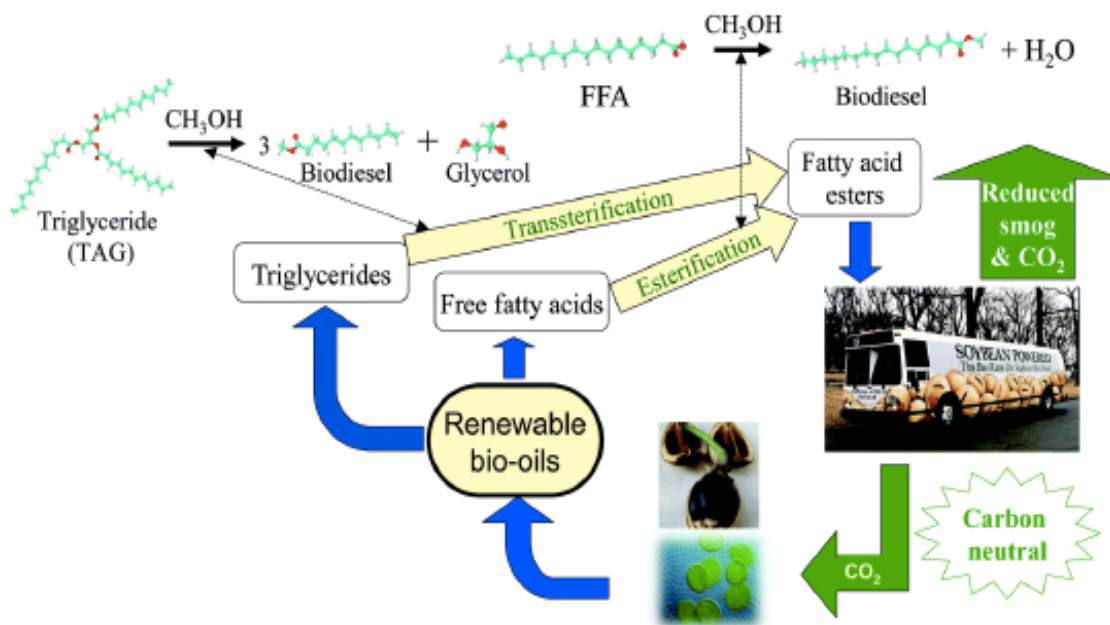
Figure 1-6. Mechanism showing the process of forming biofuels from oils and fats through transesterfication.[30]

Alternatively to biofuels, different additives have been found to be helpful to add to petroleum-based fuel such as gasoline to lessen its bad effects on human health and the environment. For instance, lead (though still harmful to the environment) has been found to reduce engine knock, helping to ensure that the engines do not pre-ignite.[14] Engine knocking can be reduced when a certain engine can have higher power, also known as a higher octane rating. Aromatic hydrocarbons have been found to reduce engine knocking due to their high energy density and high octane ratings, making them attractive fuel additives because these properties help decrease engine knock.[31]

1.5 An Overview of this Thesis

This thesis presents the investigation of two systems reacting with $O(^3P)$, 2-methyl-3-buten-2-ol and 2-methylfuran. The reaction of $O(^3P)$ with different biofuels has not been studied in much detail compared to other types of combustion reactions. This particular type of reaction is interesting because two main pathways occur: hydrogen abstraction and oxygen addition to the unsaturated C atoms. This "adduct" (addition product) then undergoes intersystem crossing (ISC) to form the primary products in the singlet state. In order to analyze the combustion behavior of these two biofuels, the experiments presented in this thesis are carried out at the Advanced Light Source (ALS) of the Lawrence Berkley National Laboratory, where experiments are performed using a multiplex time- and energy-resolved photoionization mass spectrometer.

Along with studying combustion reactions, it is also important to analyze unimolecular reactions to reveal bonding characteristics that can influence combustion behavior. Another part of this thesis is focused of the photodissociation dynamics behavior of three isomeric compounds: ortho-methylbenzyl bromide, meta-methylbenzyl bromide, and para-methylbenzyl bromide. The photodissociation of these isomers is examined using double imagining photoelectron photoion coincidence spectroscopy (i^2PEPICO), as well as just imaging photoelectron photoion coincidence spectroscopy (iPEPICO) for meta-methylbenzyl bromide. The choice of these species is related to the analysis of the dissociation dynamics of these isomers in forming the xylyl ion and finding their accurate thermochemistry from measured appearance energies. The experiments were carried out using the VUV beamline at the Swiss Light Source of the Paul Scherrer Institute.

1.6 References

1. Agency, E. P. Climate Change. **2016**. https://www.epa.gov/climatechange
2. Brewer, P. G. Rising Acidity in the Ocean: The Other CO_2 Problem. https://http://www.scientificamerican.com/article/rising-acidity-in-the-ocean/.
3. Agency, E. P. Climate Change Indicators: Greenhouse Gases. **2016** https://http://www.epa.gov/climate-indicators/greenhouse-gases.
4. Windows to the Universe. The Greenhouse Effect & Greenhouse Gases. http://www.windows2universe.org/earth/climate/greenhouse_effect_gases.html.
5. Climateoligical Information. What is Greenhouse Effect? http://www.hko.gov.hk/prtver/pdf/docs/cis/climchange/grnhse_e.pdf.
6. Agency, E. P., Greenhouse Gas (GHG) Emissions. **2014**. https://www.epa.gov/ghgemissions
7. Agency, E. P. Sources of Greenhouse Gas Emissions. https://http://www.epa.gov/ghgemissions/sources-greenhouse-gas-emissions.
8. Commission, C. E., Chapter 8- Fossil Fuels - Coal, Oil, and Natural Gas. **1994-2012**.
9. Agency, E. P. Motor Vehicle-Related Air Toxis Study. https://nepis.epa.gov/Exe/ZyNET.exe/
10. Agency, E. P. Motor Vehicle Related-Air Toxics Study. *Office of Mobile Services* Ann Arbor, MI, **1993**.
11. Murakami, Y. Oguchi, T.; Hashimoto, K; Nosaka, Y. Density Functional Study of the High-Temperture Oxidation of o-,m- and p-Xylyll Radicals. *J. Phys. Chem. A.* **2009,** *113*, 10652-10666.
12. Walsh, M. P.; McGranahan, G.; Murray, F. Vehicle Emissions and Health in Developing Countries. *Eds. Earthscan Publications: Sterling VA* **2003**, 146-175.
13. Agency, E. P. Nitrogen Oxides (NOx) Control Regulations. **2014**. https://www3.epa.gov/region1/airquality/nox.html
14. Ronald F. Colwell, P. E. Benzene in Gasoline. http://www.processengr.com/ppt_presentations/msat_regulation_options.pdf
15. Slavinskaya, N.A. and O.J. Haidn, Kinetic Mechanism For Low Pressure Oxygen / Methane Ignition and Combustion, in 49th AIAA Aerospace Sciences Meeting including the New Horizons Forum and Aerospace Exposition. 2011, American Institute of Aeroneutics and Astronautics, Inc.: Orlando, Florida.
16. Zador, J.; Taatjes, C.A; Femandes, R. X. Kinetics of elementary reactions in low-temperature autoignition chemistry. *Prog. Energ. Combust.* **2011,** *37*, 371-421.
17. Kobayashi, T.; Nagakura, S. Photoelectron spectra of substituted benzenes. *Bull. Chem. Soc. Jpn* **1974,** *47*, 2563.
18. Palmer, M. H.; Williams, M.; Speirs, M. The electronic structure of substituted benzenes; ab initio calculations and photelectron spectra for phenol, the methyl- and fluoro- derivatives, and the dihydroxybenzenes. *J. Mol. Struct.* **1979,** *52*, 293.
19. Walington, T. J.; Potts, A.R.; Andino, J.M.; Siegl, W.O.; Zhang, Z.; Kurylo, M.J.; Kuie, R.E. Kinetics of the Reaction of OH Radicails with T-Amyl Ether Revisited. *Int. J. Chem. Kinet.* **1993,** *25*, 265-272.
20. Zeng, W.; Xie, M. A novel approach to reduce hydrocarbon emissions from the HCCI engine. *Chem. Eng. J.* **2008,** *139*, 380-389.
21. Oxley, J. C. et al. Fuel Combustion Additives: A Study of Their Thermal Stabilities and Decomposition Pathways. *Energy Fuels* **2000,** *14*, 1252.

22. Sandia National Laboratoes. HCCI/SCCI Engine Fundamentals **August 27 2015**. http://crf.sandia.gov/combustion-research-facility/engine-combustion/automotive/hcci-scci-engine-research/

23. Charalambides, A. G., Homogeneous Charge Compression Ignition-the future of IC engines? *Int. J. Vehicle Design* **2007,** *44* (1-2), 1-19.

24. Demirbas, A. Biodiesel: a realistic fuel alternative for diesel engines. *Springer*.

25. Demirbas, A. Biofuels sources, biofuel policy, biofuel economy and global biofuel projections. *Energy Conversion Management* **2008,** *49*, 2106-2116.

26. Puppan, D. Enviromental Evaluations of Biofuels. *Periodica Polyechnica Service Society Manuscript Science* **2002,** *10* (1), 95-116.

27. Rothenberg, G. Catalysis; Concepts and Green Applications. *WILEY-VCH* **2008**.

28. Escobar, J. C.; Electo, S. L.; Venturini, O. J.; Yanez, E. E.; Castillo, E. F.; Almazan, O. Biofuels: Environment, technology and food security. *Renewable and Sustainable Energy Reviews* **2009,** *13* (6-7), 1275-1287.

29. Department of Conservation. How Biofuel is Made. New York. http://www.dec.ny.gov/energy/44157.html.

30. Lee, A. F.; Bennet, J. A; Manayil, J. C.; Wilson, K. Heterogeneous Catalysis of   Sustainable Biodiesel Production via Esterfication and Transesterfication. *Chem Soc. Rev.* **2014,** *43*, 7887-7916.

31. ExxonMobil. Hydrocarbon & Oxygenated Fluids. http://www.exxonmobilchemical.com/Chem-English/productsservices/hydrocarbon-and-oxygenated-fluids.aspx

Chapter 2. Experimental

The experiments presented in this thesis are based on the study of elementary reactions relevant to the combustion and autoignition behavior of selected biofuels. In this work, 2-methyl-3-buten-2-ol (MBO) and 2-methylfuran (2-MeF) oxidation reactions were investigated using the multiplexed photoionization mass spectrometer (MPIMS) of the Chemical Dynamics Beamline 9.0.2 at the Advanced Light Source (ALS) of the Lawrence Berkeley National Laboratory. The schematic of Figure 2.1 portrays the ALS floor plan. In the first part of this chapter, the main ALS components and the experimental apparatus at the beamline endstation specific to this research will be described. Additionally, the second portion of this chapter explains the experimental details of the investigation of the unimolecular dissociation of xylyl isomers carried using the VUV beamline and the imaging and double imaging photoelectron photoion coincidence spectroscopy (PEPICO and i^{2}PEPICO, respectively) endstation at the Swiss Light Source (Paul Scherrer Institute) located in Villigen, Switzerland.

2.1 The Advanced Light Source Experiments

2.1.1 Sample Preparation

The biofuels studied in this work are commercially obtained from Sigma-Aldrich, and purified using the freeze-pump-thaw method to remove possible impurities. Liquid fuels are dispensed into a glass bubbler hooked up to a vacuum pump and with the help of a steel line in which vapors of different compounds are allowed to continually flow through. The fuel vapors are dispensed into a gas cylinder and equilibrated with helium gas in order to reach a partial pressure of approximately 1%. The total pressure in these cylinders is such that it permits each tank to last for several hours with constant flow of the gas in our reactor. The total He pressure in each tank is usually around 2,000 to 2,400 Torr. The gas cylinders are continually flushed with He and allowed to be pumped for hours before a second system is ready and prepared. The pressures of these experiments are controlled using a feedback controlled throttle valve using three types of vacuum pump systems: roots pumps, turbomolecular pumps, and scroll pumps described in detail later.

2.1.2 The Advanced Light Source

The ALS is a third generation synchrotron that uses a linear accelerator (Linac) to generate accelerating beams of electrons created to produce high intensity X-ray beams.[1] A general floor plan of the ALS is presented in Figure 2-1.
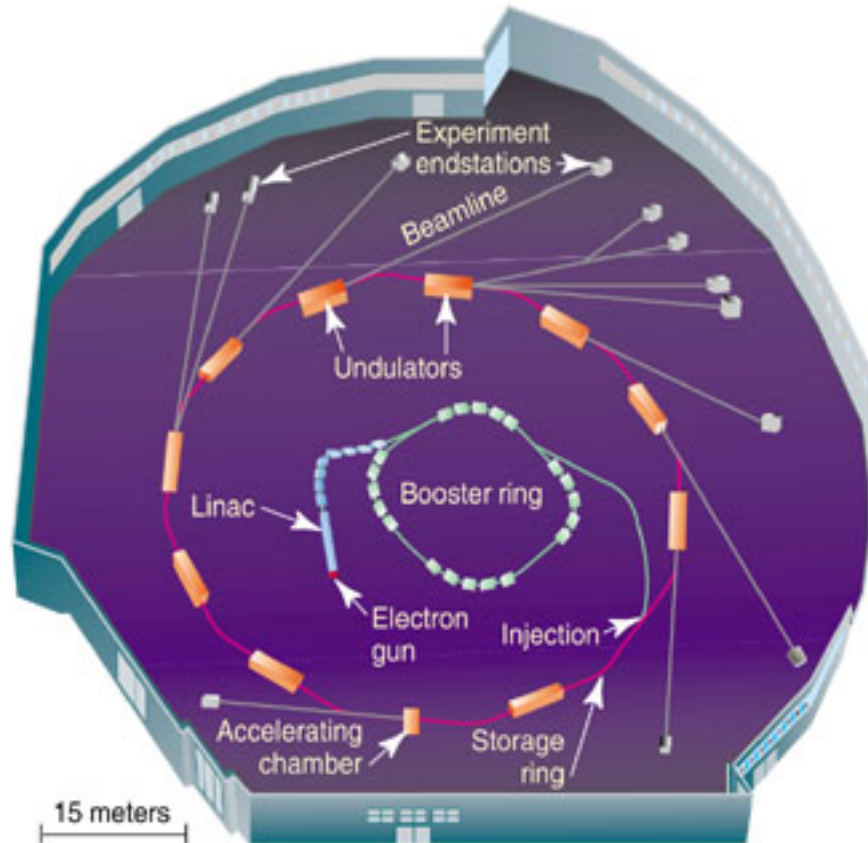
Figure 2-1. Advanced Light Source of the Lawrence Berkeley National Laboratory generated a general floor plan of the Advanced Light Source.[2]

The charged particles used to generate electromagnetic radiation at the ALS are electrons. They are produced by an electron gun that consists of cathode covered with a thermoionic material, barium aluminate, which upon heating releases electrons (thermionic effect). Due to a strong positive 500 MHz pulsed potential, the emitted electrons are attracted to the gate, passing through towards the anode, which in turn is circular, guiding the electrons to the buncher. This is part of the linear accelerator (Linac). By the application of microwave radiation (generated by a klystron[3]) the electron beam is accelerated reaching 60% of the speed of light. A klystron is a linear-beam vacuum tube that is used to amplify small signals up to higher power levels. These generated levels are then used in radar, deep-space satellite communications, and coherent RF power sources.[4] They create low-power reference signals for superheterodyne (converts received signal to fixed frequency) radar receivers and also generate high-power carrier waves for communications by being used as amplifiers.[5]

The electron beam (0.2 mm by 0.2 mm) is then injected into the booster ring, which operates at 1.9 GeV, serving as a "mini synchrotron" where the electrons essentially reach the speed of light. Finally, the relativistic electron beam is introduced into the 200 m diameter storage ring, where it

14

orbits and generates the synchrotron radiation.[6] Specific devices, called insertion devices, are used to maintain the electron beam in a circular path. These insertion devices, such as undulators, wigglers (both held at each straight section of the storage ring), and bending magnets, are responsible for keeping the electrons in the storage ring and generating the synchrotron radiation used in the various beamlines for experimentation. Undulators and wigglers have arrays of magnets with alternating poles. Wigglers produce synchrotron radiation with a broader spectrum compared to undulators. For clarification, the diagram below (Figure 2-2) shows the electron beam trajectory and the emitted electromagnetic radiation passing through undulator magnets. The electromagnetic radiation is generated due to the variation in distance between the opposite poles.
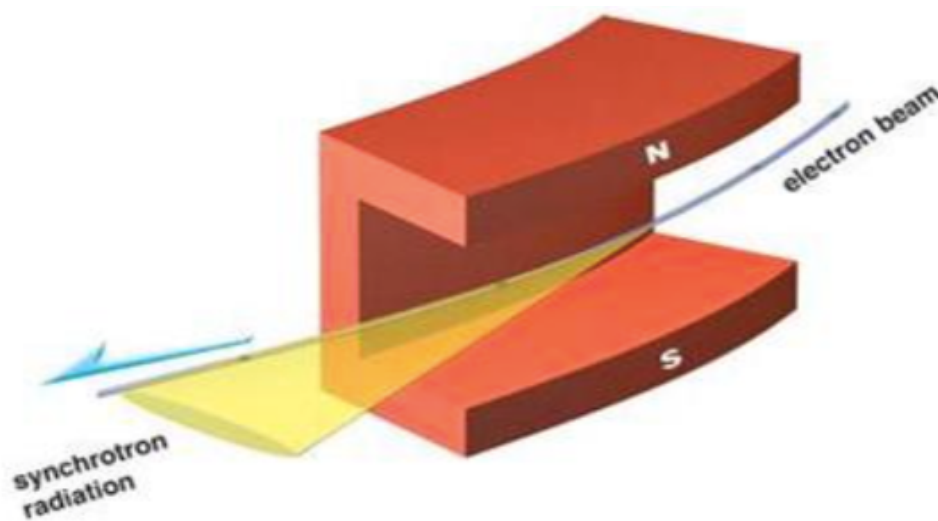
Figure 2-2. A diagram of generated synchrotron radiation through the electron beam passing in between magnetic poles.[7]

The ALS radiation has a high brightness, which defines the direction of the photons in the beam, compared to similar synchrotron sources all over the world. This synchrotron radiation is six orders of magnitude more intense that light produced from X-ray tubes alone. This difference allows the ALS to complete fast experiments. In Figure 2-3, the comparison of different light sources available in the United States is reported. Synchrotron tunability allows radiation to be changed at the different beamlines through monochromators, varying photon energies with a small energy uncertainty (high energy resolution) and giving broader ranges for different experiments.
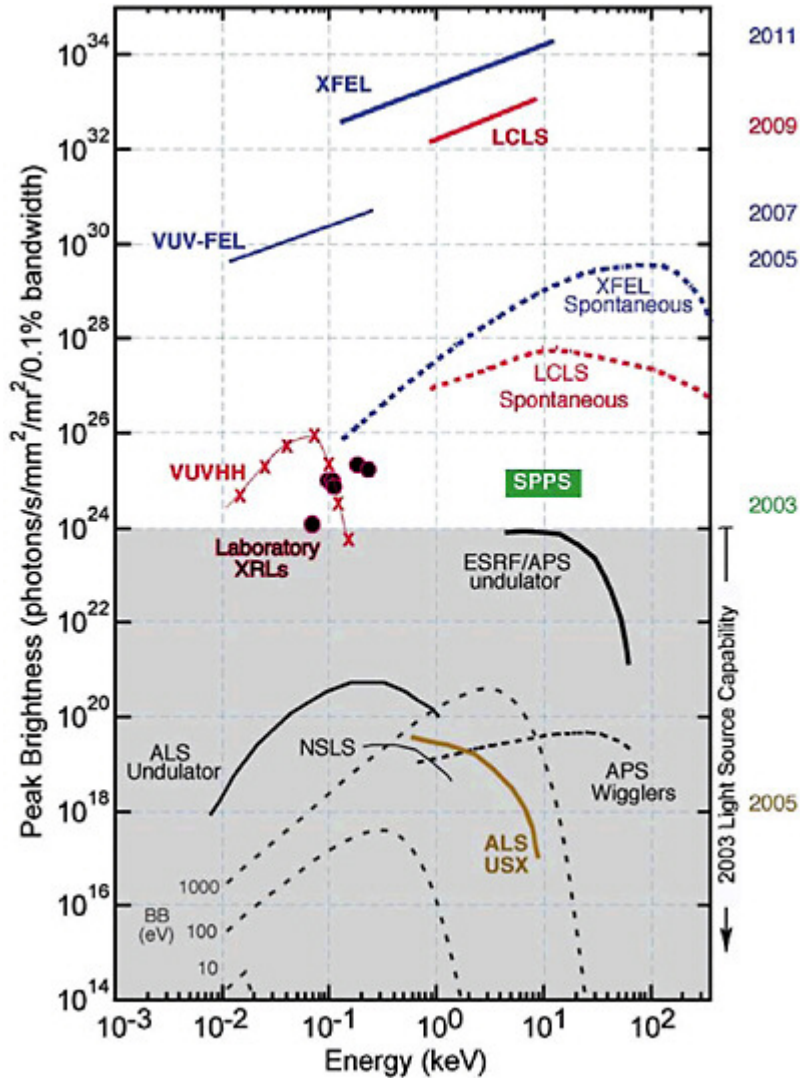
Figure 2-3. A graph reported by the Advanced Photon Source at the Argonne National Laboratory comparing the brilliance of different X-ray light sources within the United States.[8]

There are twelve straight sections in the storage ring; nine of these are used as insertion devices: undulators, wigglers, elliptically polarizing undulators (EPUs), and bending magnets. Each insertion device accelerates electrons through a long magnetic structure. During this continuous acceleration (change of travel direction), synchrotron radiation is emitted and directed towards the various beamlines (43 beamlines at the ALS). Undulators and wigglers are located at each straight section of the storage ring.[6] The photon energy of the undulator can be calculated using the equation 2.1 below, provided by Margaritondo.[9] This equation provides the overall energy that can be produced when there is small spacing between the magnets.[9] The photon energy of the undulator ($\hbar\varpi$), is expressed with the reduced Planck constant ($\hbar$), the speed of light (c), the beam energy (γ), the undulator period (λ_L), the wiggler strength parameter (K), and the light emission direction (θ_L).

16

$$\hbar\varpi \cong \left(\frac{4\hbar\pi c\gamma^2}{\lambda_L}\right)\left(\frac{1}{1+\frac{1}{2}K^2+\theta_L^2\gamma^2}\right) \qquad (2.1)$$

γ can be calculated separately using equation 2.2, where E is the electron energy and m_o is the mass of an electron at rest. K can be calculated using equation 2.3, where e represents the electron charge and B_L the magnetic field strength.

$$\gamma = \frac{E}{m_o c^2} \qquad (2.2)$$

$$\kappa = \frac{eB_L\lambda_L}{2\pi cm_o} \qquad (2.3)$$

2.1.3 Chemical Dynamics Beamline

The experiments of this thesis are carried out at the Chemical Dynamics Beamline 9.0.2. At 9.0.2 the undulator radiation passes through a narrow gas filter (filled with 30 Torr of either Ar or Kr gas). The gas filter is used to remove higher-order harmonic photons from the undulator. Beer's Law (equation 2.4) is used to calculate the extent of suppression of the higher-order harmonic photons (I represents transmitted photon intensity, I_0 is the incident photon intensity, N is the density of gas, σ is the photoabsorption cross section of either Ar and Kr, and l is the length of the gas cell).

$$\frac{I}{I_0} = e^{-\sigma IN} \qquad (2.4)$$

After the light passes through the gas filter, it reaches a 3 meter off-plane Eagle monochromator.[10] According to Bragg's Law (equation 2.5), photon energies[11] can be selected by a range though any incoming radiation that is reflected. Monochromators are essential in the selection of narrow bandwidths of different wavelengths from a wider input of the synchrotron light in the energy range of 7.2-25.4 eV.

$$n\lambda=2d\sin\theta \qquad (2.5)$$

where n is an integer and d is the spacing between two parallel atomic layers of the monochromator lattice (reflecting plane). Only a certain wavelength (λ) can be reflected from the incident radiation.

According to the equation above, it is visible that the angle difference between the monochromator surface and the incident synchrotron radiation (θ) allows the selection of different wavelength ranges. From there, the narrow bandwidth helps direct the light into the ionization chamber. The range of photon energies is wide enough to be able to characterize species during combustion experiments.

2.1.4 Experimental Apparatus

The actual apparatus used for the experiments presented in this thesis consists of four main parts, all under high vacuum: excimer laser, time-of-flight mass spectrometer (TOFMS), ionization chamber, and microchannel plates (MCP) detector.
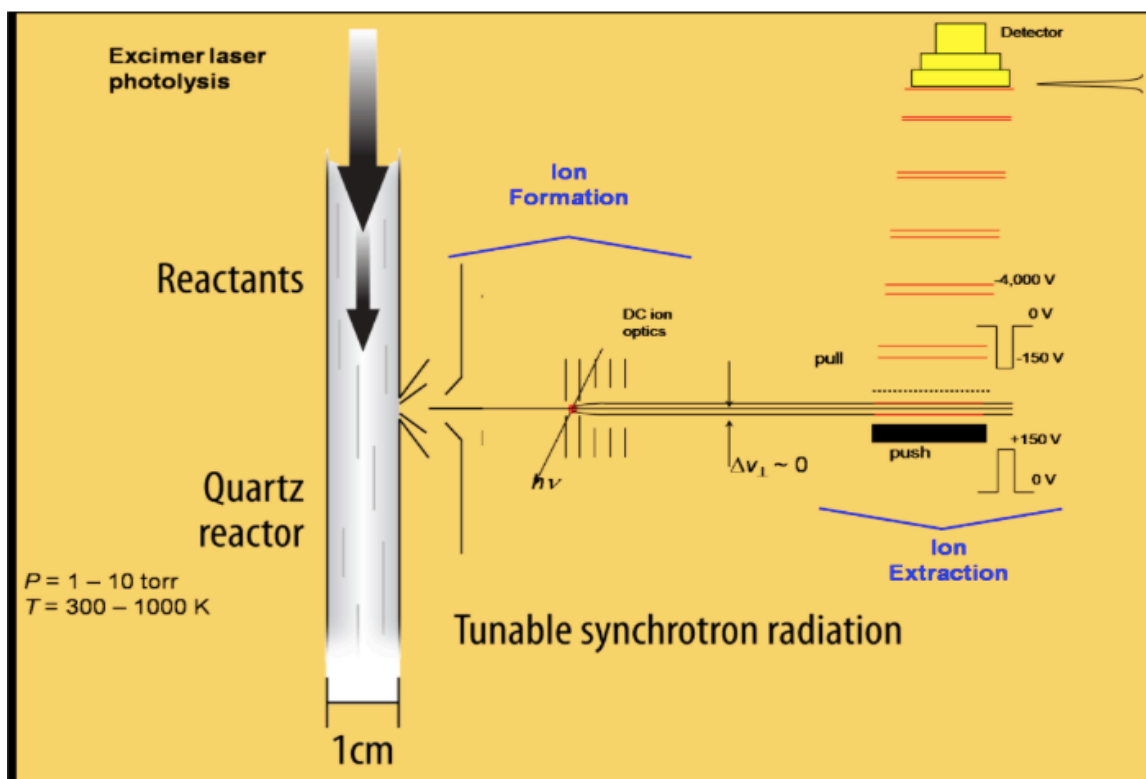
Figure 2-4. Multiplexed chemical kinetics orthogonal mass spectrometer schematic.[12]

When setting up the apparatus for experimentation several steps occur first. The apparatus is aligned with respect to the ALS radiation and a "polynomial" is obtained for the energy calibration. This calibration occurs due to the "energy alignment" between the monochromator and undulator. From this, the energy resolution can be measured through performing a calibration. This is done through running a mass spectrum of a noble gas, in our case Ar (15.76 eV), and a calibration gas (a gas consisting of known photoionization cross-sections; ethane, propene, and butene). The range of

photon energy for each run is based upon the adiabatic ionization energy (AIE) of the particular compound under investigation. The AIE can be found on the NIST chemical website or calculated using computational methods described later in this thesis. Usually, before analyzing a particular reaction it is essential to determine whether upon photoionization the particular species in question forms dissociative fragments. Photoionization spectra are taken for all the reaction species. Specifically, when this spectrum is not known for the reactant, an absolute photoionization spectrum is collected with no reaction, i.e., without the photolysis laser. In order to obtain this spectrum, a calibration gas containing ethene, propene, and 1-butene is used and ionized to determine relative fragmentation and photoionization cross-sections of the parent molecule of the particular compound of interest. This methodology is explained in detail in chapters 4 and 5 for the characterization of the oxidation reactions of two systems.

The reactions of these experiments are carried out in a heated 62 cm slow flow quartz reactor tube (insulated by a 18 μnm thick Nichrome tape ensuring temperature uniformity) with a 1.05 cm internal diameter.[10] The reactant species are introduced into the reaction cell using calibrated mass flow controllers (MFCs) and flow through a 650 μm pinhole on the reactor side into the ionization region, where they are photoionized through crossing tunable synchrotron radiation. Throughout these experiments, the temperature and pressure are constantly controlled. In this work the combustion reaction of 2-methyl-3-buten-2-ol and 2-methylfuran with $O(^3P)$ are analyzed at varying temperatures. The temperature is measured by thermocouples and varied using a closed-loop feedback circuit. The pressure in the reactor tube is held at 4 Torr at room temperature and increased to 7 Torr at higher temperatures. This is done in order to have comparable concentrations at different temperatures.

The pressure of these experiments are maintained by a capacitive manometer and controlled with closed-loop feedback valve in conjunction with the Roots pump. As the combustion reaction is happening, the flow rates of the mixture and particular gases are controlled using MFCs. From equation 2.6 it is possible to calculate the initial concentration of the reactants.

$$Concentration = (3.24 \times 10^{16})(P)\left(\frac{F_R}{F_T}\right)\left(\frac{T}{298.15}\right)^{-1} \tag{2.6}$$

where P is the pressure maintained inside the chemical reactor, F_R is the flow rate of the reactant (assuming 100% purity; otherwise, its purity should be used to have the correct initial concentration) in standard cubic centimeter per minute (sccm), F_T is the total flow rate of all compounds in sccm, and T is the temperature of the reactor in K. The experiments occur with a continuous gas flow rate of approximately 400 cm s^{-1} and 4 Hz repetition of the excimer laser so that the sample keeps pumping into the reaction tube.

The reaction mixture (consisting of the selected system, the photolytic precursor, and the carrier gas He) is flowed into the reactor tube and a 351 nm excimer laser generates the $O(^3P)$ from NO_2 photolysis. As the gas mixture flows through the pinhole described above, a molecular beam is formed and directed to the differentially pumped ionization chamber. Within the ionization chamber synchrotron radiation then ionizes the species (byproducts and reactive intermediates) forming from the reaction with $O(^3P)$. Each particular combustion reaction of the experiments presented in this work is set up with a different photon energy range and has a step size of 0.025 eV with ~250 laser shots at each photon energy.

2.1.4.1 The Excimer Laser

The oxidation reactions of the investigated system are carried out using a photolytic precursor. Specifically, in the presented experiments NO_2 is photolyzed using an unfocused excimer laser at 351 nm[13] to yield the wanted $O(^3P)$ reactant. Lasers operating principle is based on the fundamental concept of population inversion, which is defined by the population of a molecule at its excited electronic state being greater than the population it has at its ground state.[14] Thus, as the molecule relaxes to its ground state, a photon with energy equal to the gap (laser band) between the ground and excited state is emitted.

The wavelength of the light always depends on the specific mixture and the laser band between the excited and ground state. The experiments carried out in this work utilize 351 nm photons using a xenon fluoride (XeF) excimer (that stands for "excited dimer") laser. In a gas chamber, Xe and F_2 gases are pumped in, where an electrical discharge creates a spark that ionizes and excites Xe atoms that bond to flouring atoms creating XeF.

$$F_2 + Xe^* + M \rightarrow (XeF)^* + F \qquad\qquad (2.7)$$

This rare gas halide is referred to as excimer (excited dimer). The excimer exists only in the excited state. From this it is seen how the population inversion is easily achieved in this lasing system because the ground state of the molecule is unbound.

The excimer laser consists of a laser cavity that includes the gas mixture as well as a buffer gas where an electric current passes from the electrode through the gas exciting the electrons of the molecules.
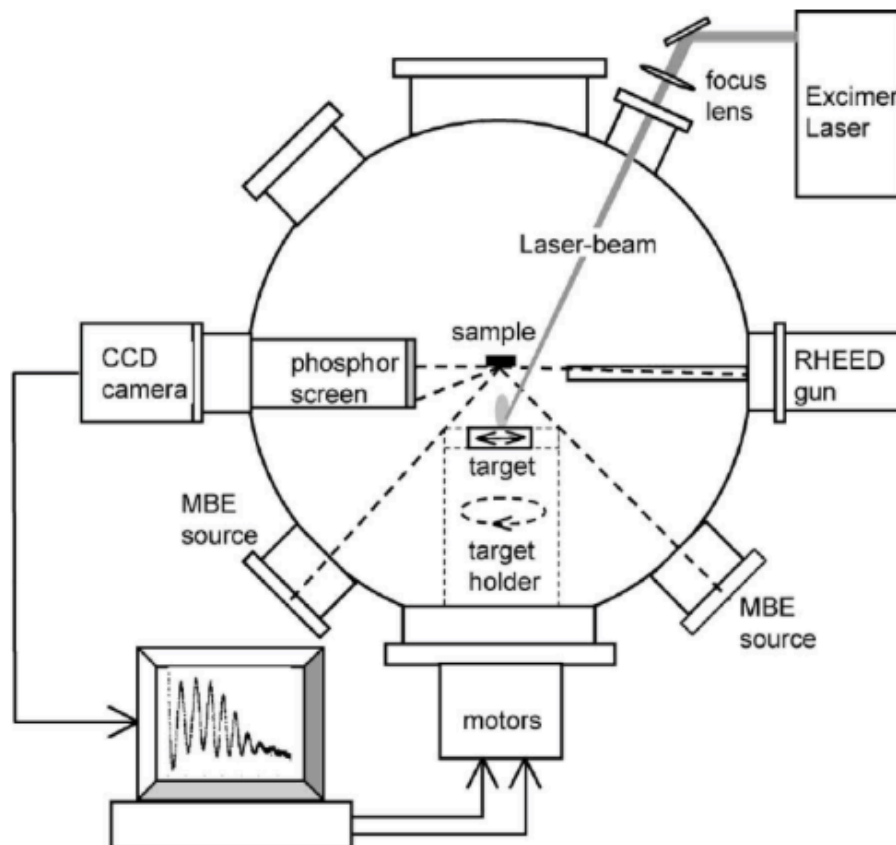
Figure 2-5. A general schematic of an excimer laser.[15]

The ground state oxygen atoms are generated through 351 nm photolysis of 1% NO_2 and helium gas ($NO_2 \rightarrow O(^3P) + NO$). At a wavelength below 398 nm, $O(^3P)$ has a reported absolute photoionization cross-section of 4.62 x 10^{-19} cm^2 according to Vandaele[16] and quantum yield of around 1.00.[17] The unfocused excimer laser in this work is fired at 4 Hz and has a pulsewidth of 20 ns and fluence of 170 mJ cm^{-2}.[10]

2.1.4.2 Vacuum Pumps

These experiments have three main vacuum pumps that are essential in ensuring that the reaction cell, the reaction chamber, the ionization region, and the TOF detector remain free of any contamination. These are root, turbomolecular, and scroll pumps.

There are three turbomolecular pumps with pumping speeds of 3200 Ls^{-1}, 1600 Ls^{-1}, and 600 Ls^{-1}. These pumps help gas molecules travel from inlet to outlet due to rotor and stator blades that transfer momentum to the gas molecules to continue to flow to the exhaust, maintaining the pressure of 10^{-8} Torr.[18] The 3200 Ls^{-1} turbomolecular pump is placed in the source chamber where the

molecular beam is formed. The 1600 Ls^{-1} is in charge of pumping the ionization region and the 600 Ls^{-1} pumps the detector region of the experimental apparatus.[19] A diagram presenting the main parts of the turbomolecular pumps is presented in Figure 2-6.
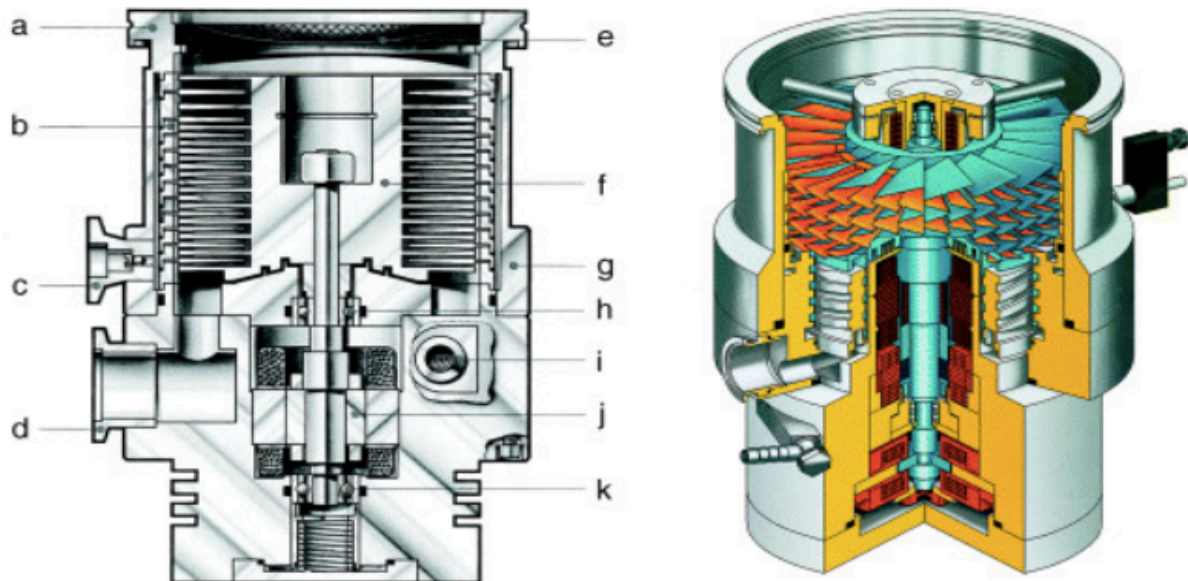
Figure 2-6. On the left is the inside view of a Turbomolecular pump; a) vacuum inlet, b) stator pack, b) venting flange, d) forevacuum flange, e) splinter guard, f) rotor, g) pump casing, h),k) ball bearing, i) cooling water connection, j) motor. The right is amore external view of the pump.[19]

The large main pump is coupled together with two other pumps; Roots pump and backing scroll pump located at the end of the slow flow reactor tube. Each scroll pump consists of two scrolls, where only one is moving.[18-21] As the rotating scroll orbits, the gas pockets are pushed toward the pump center letting out gases. The pressure of these pumps is held at 10^{-2} Torr with a speed ranging from ~6 to 13 Ls^{-1}.[23] Once the inlet is closed, the trapped gas is compressed until it reaches a higher pressure, and it can then escape at the center of the spiral for the next gas to come in (Figure 2-7).

Scroll pump design and performance

Inlet Region

Orbiting Rotor

Exhaust Region

Stator

Pumping speed
Ultimate pressure
Service & maintenance
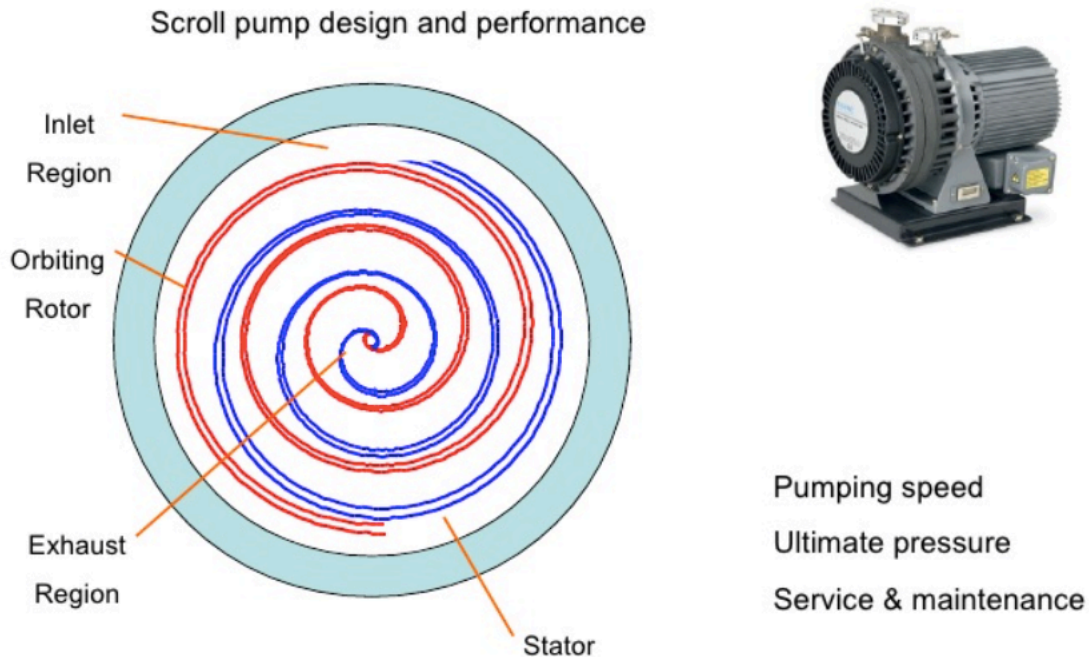
Figure 2-7. The inside view of a scroll pump and outside diagram.[24]

The root pump is a dry rotary displacement pump that is made up of two symmetrically shaped counter-rotating impellors that are synchronized by external gears and rotor bearings. These pumps obtain their fast rotation speed (1000-3000 rpm) from a pressure of $20\text{-}10^{-4}$ Torr. Their main job is to evacuate unwanted gases from the reactor tube. This is designed so that no physical contact occurs between the two impellors as they are rotating close together. The gas moves into the inlet of the roots pump and goes toward the outlet as the rotors rotate. Compared to the scroll pump, roots pump has a pressure ranging from 10 to 10^{-3} mbar and pumping speeds of ~21 to 8333 Ls^{-1} Figure 2-8 portrays a schematic of the function of the root pump.
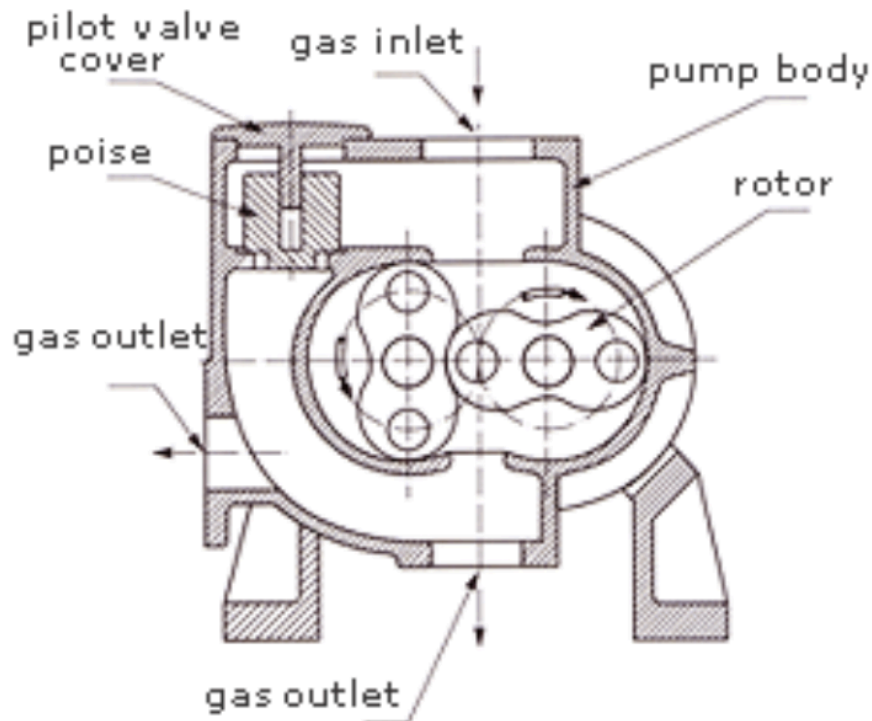
Figure 2-8. A diagram of a Roots pump.[25]

2.1.4.3 Time-of-Flight Mass Spectrometer and Microchannel Plates

Whenever the energy of light is higher than the ionization energy of a molecule, ionization occurs. The ionic species created throughout these experiments are focused and collimated with the aid of a series of electric fields towards the end of the first part of the flight. A positive 150 V electric field and a negative 150 V help change the initial ions direction by 90° to guide them towards the detector.[26] The focused ions enter the orthogonal accelerator at a velocity, v_{beam}, where the ion kinetic energy in the beam is in the range of 10-100 eV.[26] With a voltage of 5-10 kV, ions are pushed orthogonally (with respect to their initial direction) by a sharp pulse and accelerated to a velocity of v_{tof} into the TOF analyzer.[26] The angle between the orthogonally accelerated ions and ion beam can be calculated using the below equation. The velocity of the beam and TOF can be determined using the following equation;

$$\theta = tan^{-1}\left(\frac{v_{tof}}{v_{beam}}\right) \tag{2.8}$$

24

where e is the electron charge ($1.6021765 \times 10^{-19}$ C), z in the integer number of electron charges, U is the applied voltage, mass of ion (m_i), and K_i is the kinetic energy of the ions. Once the ions travel through the drift path to the TOF analyzer, a new set of ions come in. The ions created have the same kinetic energy and distance to the detector, however, the masses are separated based on their different velocities leading to their mass-to-charge ratio separation (m/z).

$$v = \sqrt{\frac{2ezU}{m_i}} = \sqrt{\frac{2K_i}{m_i}} \tag{2.9}$$

Once the gas mixture reaches the ionization region of the TOF analyzer, ions are extracted into a continuous beam until the heaviest ions reach the detector.[27]

At the ALS, the detector is made up of micro-channel plates (MCP) and time-of-flight digital converters (TDC) that raise the resolution and convert data output for experimental data analysis. The MCP are basically channel electron multipliers (CEM) present in an electrooptical ion detector (EOID).[28] CEM tubes are only one micrometer in diameter giving the advantage to be placed into an array close together. This increases the likelihood for created ions to hit them. This is important because the surface of CEMs is made up of semiconductors that, when hit with ions, create secondary electrons. In this work, Chevron configuration (V-stack) is used within the time-of-flight mass spectrometer that is made up of two stacked MCPs, which are responsible for transferring and intensifying the signal. Figure 2-9 shows a diagram of the three different types of MCP configurations.
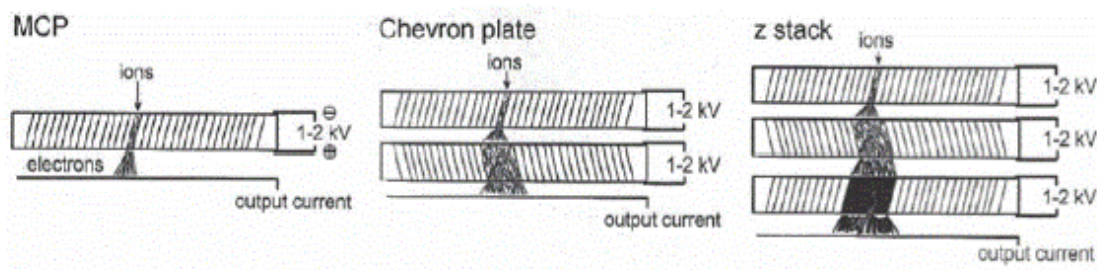
Figure 2-9. The middle represent a chevron-plate orientation with two MCPs, the left is one MCP with an array of CEMs, and the right is a "z stack" orientation of three or more MCPs.[29]

2.2 iPEPICO and i^{2}PEPICO at the Swiss Light Source

Photoelectron photoion coincidence spectroscopy (PEPICO) is an experimental method encompassing both photoelectron spectroscopy as well as photoionization mass spectrometry. Vacuum ultraviolet (VUV) radiation is used to ionize gas-phase molecules forming a cation and

photoelectron. Through time-of-flight (TOF) mass spectrometry, the masses of different photoions formed can be determined and velocity map imaging (VMI) is used to detect photoelectrons. The experiments presented in this work were performed using the X04DB vacuum ultraviolet (VUV) beam line at the Swiss Light Source (Paul Scherrer Institute) in Villigen, Switzerland. The time-of-flight for electrons are around three orders of magnitude smaller than the time-of-flight distributions for photoions. Ortho-xylyl bromide and para-xylyl bromide were measured using the double imaging photoelectron-photoion coincidence (i^2PEPICO) spectrometer. Meta-xylyl bromide, however, was measured using the imaging photoelectron-photoion coincidence (iPEPICO) spectrometer.

2.2.1 The Swiss Light Source

The SLS is a third generation synchrotron facility that produces electromagnetic radiation with very high brightness, wide wavelength spectrum, and very stable temperature conditions.[30] Radiation at the SLS is emitted at a horizontal angle of over 8 mrad through the X04DB bend magnet port. The SLS contains a 2.4 GeV electron storage ring operated at 400 mA current mode.[30] The VUV, similar to visible and infrared light, has a considerably wider radiation cone above the plane of the storage ring. Within the storage ring, synchrotron light is linearly polarized (within the plane) and elliptically polarized (above and below the plane). In the bend magnet, the electron beam is 45 μm FWHM vertically and 185 μm FWHM horizontally.[31] The possible endstations of the SLS are presented in the diagram below.
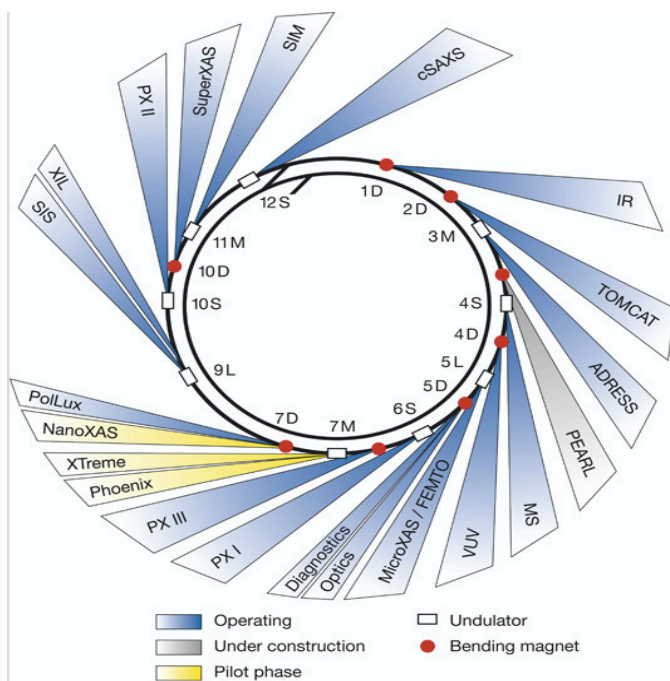
Figure 2-10. Diagram displaying the endstation layout of beamlines located at the SLS.[32]

2.2.2. VUV Beamline

The VUV beamline located at the SLS with a photon energy range from 5 to 30 eV is used to excite electrons and trigger photoionization and photodissociation.[33] This energy range has a resolving power of 10^4. VUV radiation is attractive due to its tunability over lasers and resolution over discharge lamps. The resolution is indeed sufficient to match almost accurate thermochemical data, 0.1 kJ/mol accuracy.[34] Another attractive feature of the particular VUV beamline at the SLS is an in-house designed rare gas filter that suppresses higher harmonic radiation to get rid of higher energy contributions. This gas filter was specifically designed to be more compact, easy to align and require less pumping power. The use of a good filter is essential for studies because the pressure has to be low enough at each end of the filter for the proper operation of each beamline and, yet, reach high-enough photoabsorption efficiency for the suppression of higher harmonics.[34] The gas filter is 0.90 m long and has a total of nine differentially pumped sections (Figure 2-11a and b), in which seven are exactly similar to one another.[34] Within the gas filter, section 7 holds the monochromator exit slit and section 6 is connected to the gas inlet.
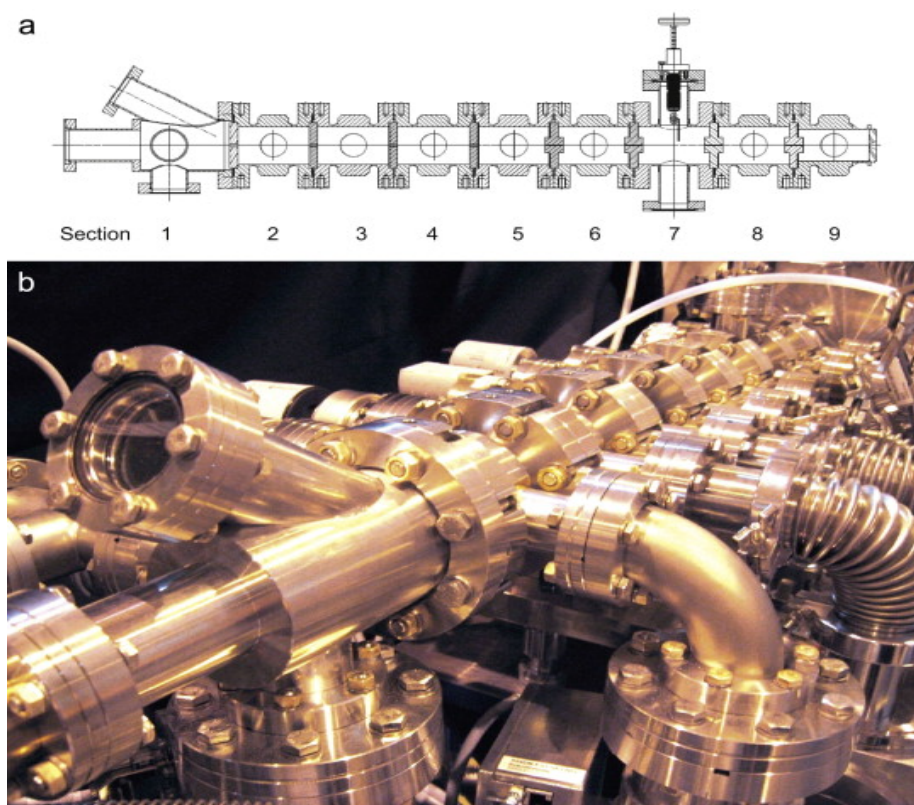
Figure 2-11. a) 90mm long gas filter diagram with all nine sections; VUV light enters from the left and endstation is attached right after section 9. b) Picture of the designed gas filter.[34]

The maximum pressure allowed within the transfer line to the storage ring is 10^{-8} mbar. To further prevent contamination, and in particular gas leakage, safety valves are placed. In front of section 1, a 1 m automated pneumatic valve is placed to prevent any gas leakage throughout experiments.

2.2.3 Experimental Apparatus

There are two coincidence apparatuses available at the SLS, an imaging photoelectron photoion coincidence experiments (iPEPICO) and a double imaging photoelectron photoion coincidence experiment (i^2PEPICO). Each gas-phase sample is cooled and ionized through monochromatic synchrotron VUV radiation. Upon ionization, a photoelectron is produced acting as start signal for the ion time-of-flight analysis, in which kinetic energy is analyzed using velocity map imaging on a Roentdek DLD40 position sensitive delay-line detector with sub-millielectronvolt kinetic energy resolution at threshold to record coincidences.[35] In the case of the iPEPICO, the photoelectron is velocity mag imaged onto a 40mm Roentdek delay line detector and photoions are mass analyzed through time-of-flight distributions. For i^2PEPICO however, both the photoelectrons and photoions are imaged in a symmetric setup. The four delay line signals from each detector are processed after constant fraction discrimination with the help of an 8-channel ATR 19 unit and recorded by a HPTDC8-PCI card.

Gas samples are processed from the headspace of a glass vial through a 6 mm Teflon tube into the ionization region of the experimental chamber, (pressure of 1-3 x 10^{-6} mbar).[36] The apparatus consists of a 2 mm x 2 mm interaction region, where VUV synchrotron radiation is dispersed in grazing incidence by a 600 grooves/mm laminar grating.[35-36] Within the gas filter, is a 10 cm long chamber is filled with 10 mbar of Ne-Ar-Kr mixture. Photoions and photoelectrons from opposite directions are extracted using a constant 40/120 V cm^{-1} electric field.[37] The iPEPICO has an extraction field available of 20-120 V cm^{-1} and the i^2PEPICO has a theoretical high limit of around 500 V cm^{-1}. The key feature of the iPEPICO experimental setup is to resolve threshold electrons up to 1.2 GeV imagines onto the detector measuring unimolecular dissociations rate constants. For i^2PEPICO, the experimental setup enables kinetic energy release in order to measure ion imaging and introduce second acceleration fields. Figure 2-12 represents a schematic of both endstations held at the VUV beamline at the SLS.

a)   b)
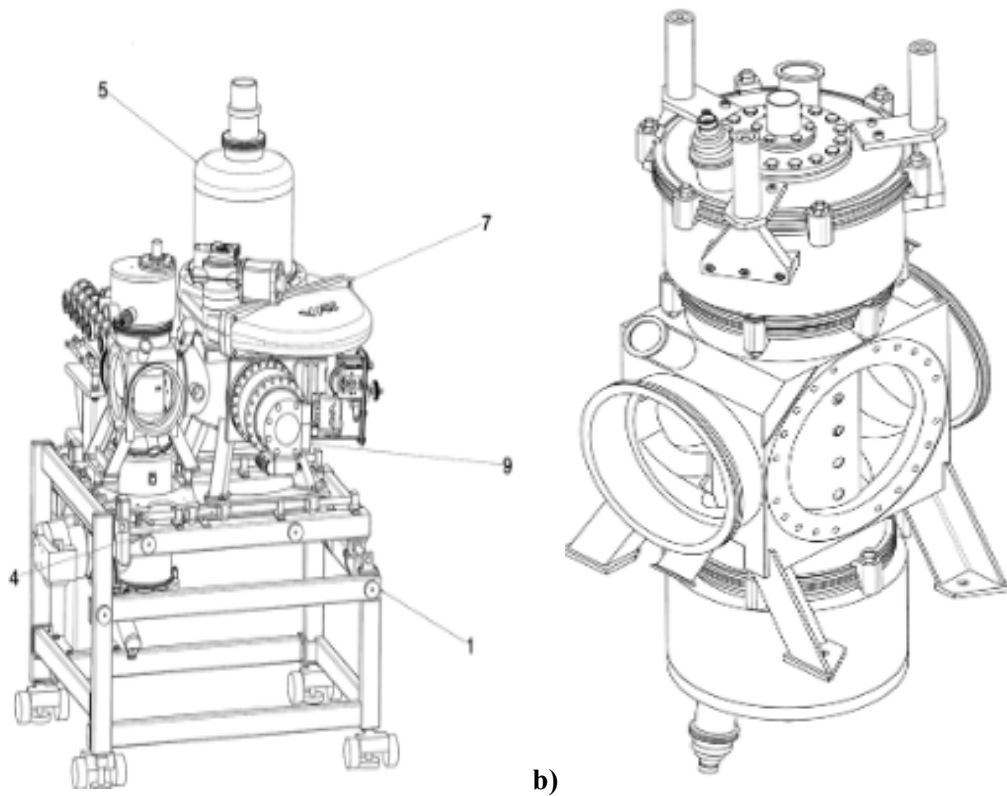
Figure 2-12. a) A schematic overview of the iPEPICO, b) schematic of the i^{2}PEPICO endstation.

The attractive features of the double imaging PEPICO apparatus are: easy grating exchange; reproducible switch between gratings; greater adjustment ranges for alignment; and increased pitch angle to increase the energy range. As visualized in Figure 2-13, the double imaging setup was simply designed as an extension of the iPEPICO experimental setup. The i^{2}PEPICO consists of an ionization chamber with a smaller size that allows mounting only one of the two pumps (2-6 x 10^{-6} mbar).[37] After the light passes through the gas filter, it travels 50 cm into the ionization region.[37] The light beam is 4x8 mrad^2 and the ionization chamber in the new setup is shifted 50 mm back to the center when compared to the original experimental setup.[37]
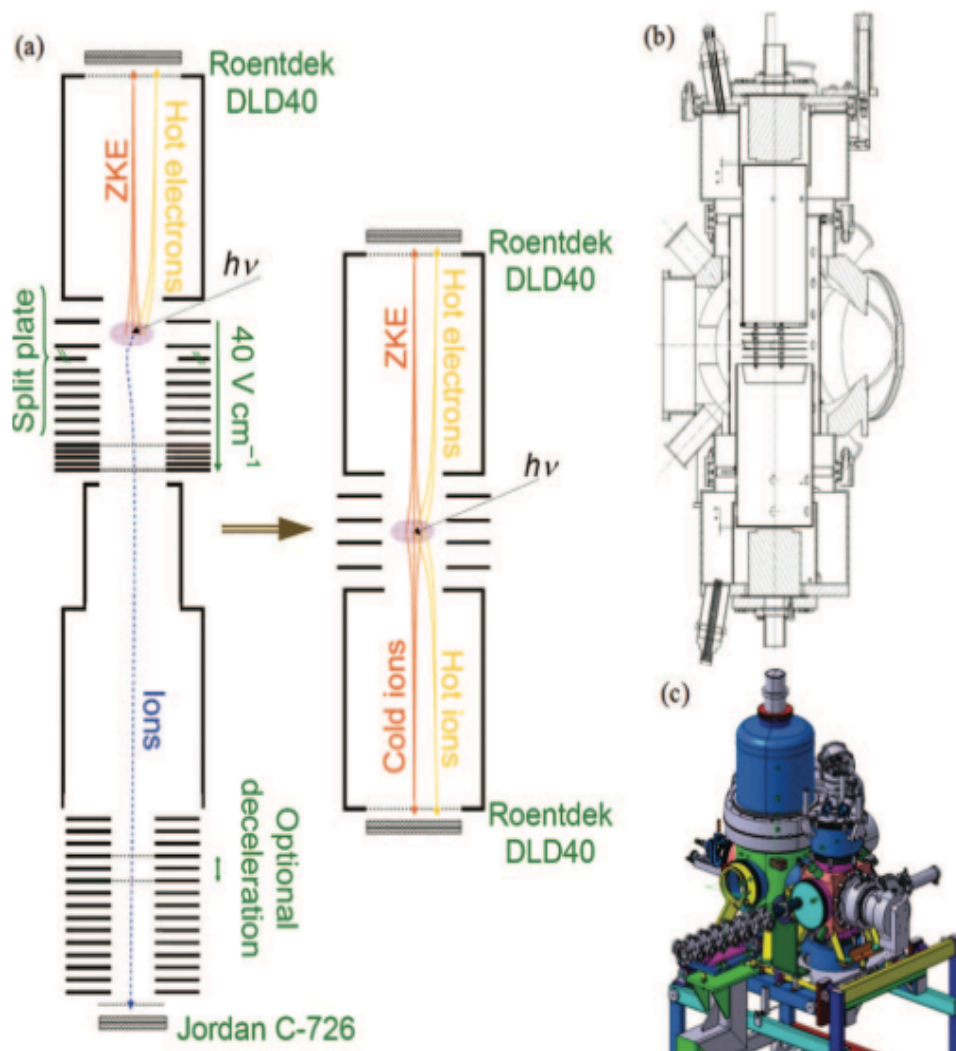
Figure 2-13. a) A diagram representing the changed from the velocity map imager/TOF analyzer of the iPEPICO set up to i^{2}PEPICO. b) Experimental diagram c) The set up of the light beam entrance through the gas filter into the ionization chamber.[37]

2.2.4 PEPICO Programs and Data Analysis

Each experimental apparatus has a specific program for data analysis. The two programs allow for the coincidence counts from both the center detector and ring detector to be listed in a series of numbers. The multi-channel analyzer (MCAS) points out the total number of active channels that give the number of points. The number of points created can be controlled through the script input for both programs. The points are split in half; half are the detection of electrons on the center while the second half refers to the detection of hot electrons on the ring. In order to obtain the necessary information from the data, the data is inputted into both programs and specific scripts will isolate the

hot electrons and help visualize the signal. Figure 2-14 shows examples of iPEPICO data analysis program, which includes the electron subtraction. The data is extrapolated and a weighted factor can be used to determine the count of zero kinetic energy electrons.
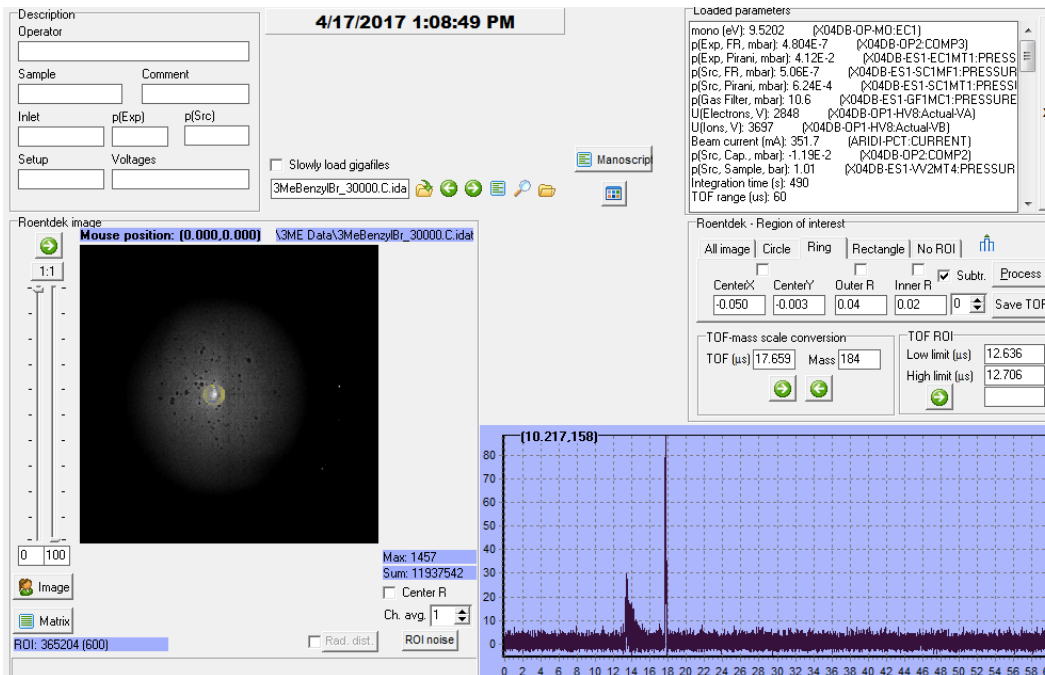
Figure 2-14. An example of the iPEPICO program; top right is the script, bottom right is the TOF and bottom left is the center and ring electron subtraction.

2.3 References

1. ALS Quick Facts and New Tools: Make New Investigations Possible. http://www-als.lbl.gov/index.php/about-the-als/quick-facts.html.
2. Probing the Liquid Water Surface Sci. Tech. Rev. http://www.llnl.gov/str/November01/Tobin.html.
3. Sessler, A. M.; Yu, S.S. Relativistic Klystron Two-Beam Accelerator *Phys. Rev. Letters* **1987,** *58*, 2439.
4. Varian, D. The Inventor and the Pilot: Russell and Sigurd Varian. *Pacific Books, extracts used with permission* **1983**.
5. InnovateUs. What is a Klystron Tube? **2006-2013**. http://www.innovateus.net/science/what-klystron-tube
6. Margaritondo, G. Introduction to Synchrotron Radiation; Oxford, University Press: New York, **1988**.
7. UNiST: News Center http://news.unist.ac.kr/kor/20160922-01/
8. Overview of the Aps. http://www.aps.anl.gov/About/APS_Overview/index.html.
9. Margaritondo, G. A Primer in Synchrotron Radiation: Everything You Wanted to Know About Sex (Synchrotron Emission of X-Rays) but Were Afraid to Ask. *J. Synch. Rad.* **1995,** *58*, 2439.
10. Osborn, D. L. et al. The Multiplexed Chemical Kinetic Photoionization Mass Spectrometer: A New Approach to Isomer-Resolved Chemical Kinetics. *Rev. Sci. Intrum.* **2008,** *79*, 104103.
11. Chemical Dynamics Beamline. Beamline 9.0.2 Mini-Tour. http://chemicaldynamics.lbl.gov/tour.html.
12. Ray, A. Characterization of Ethen + OH Products and Cyclohexene Ring Opening Mechanism Education Via Synchrotron Photoionization Mass Spectrometry. **2010,** *University of San Francisco, San Francisco*.
13. IPUAC Compendium of Chemical Terminology 2nd ed. *IUPAC* **2006**.
14. Khanin, Y. I. Fundamentals of Laser Dynamics; Cambridge International Science Publishing: Cambridge, **2006**.
15. Shen, J.; Gai, Z.; Krischner, J.Growth and Magnetism of Metallic Thin Films and Multilayers by Pulsed-Laser Deposition. *Surf. Sci. Rep.* **2004,** *52,* 163
16. Vandaele, A. C.; H.ermans, C.; Simon, P.C.; Carleer, M.; Colin, R.; Fally, S.; Merienne, M.F.; Jenouvrier, A.; Coquart, B. Measurements of the NO2 Absorption Cross-Section from 42000 cm-1 to 10000 cm-1 (238-1000nm) at 220 K and 294 K. *J. Quant. Spectrosc. Ra.* **1998,** *59*, 171-184.
17. Troe, J. Are Primary Quantum Yields of No2Photolysis at ^ < 398 Nm Smaller Than Unity? *Z. Phys. Chem.* **2000,** *214*, 573-581.
18. Lafferty, J. M. Foundations of Vacuum Science and Technology. *Wiley: New York* **1998**
19. Day, C. Vacuum Technology. Ullmann's Encyclopedia of Industrial Chemistry **2014,** 1-39
20. Enosawa, H.; Urano, C.; Kawashima, T.; Yamamoto, M. High Throughput Tandem Turbomolecular Pump for Extreme High Vacuum. *AVS* **1990,** *8*, 2768-2771.
21. Osborn, D. L. et al. The multiplexed chemical kinetic photoionization mass spectrometer: A new approach to isomer-resolved chemical kinetics. *Rev. Sci. Inst.* **2008**, 79.
22. Electron Microprobe Laboratory. *Instrumentation* **August 31, 2015**.
23. O'Hanlon, J. F. A User's Guide to Vacuum Technology. *Wiley-Interscience: Hoboken* **2003**.
24. iN SlideShare. A simple overview of the animated training workshop for pressure, vacuum, and flow technology.

https://www.slideshare.net/LukeHinkle/complex2-simple-vacuum-training-quick-demo-presentation

25. HangtZhou Ever-Power Vacuum Pumps Co., Ltd. http://www.china-vacuum-pumps.com/vac/roots-vacuum-pumps.htm
26. Gross, J. H. Mass Spectrometry, 2nd ed. *Berlin Heidelber: Springer* **2011**.
27. Laboratories., S. N., OA-TOD Timing System. **August 12, 2015**.
28. Fkoog, D. A.; Holler, F. J.; Crouch, S. R. Principles of Instrumental Analysis. 6 ed. United States: Brooks/Cole, Cengage Learning **2007**.
29. Gross, J. B., Mass Spectrometry: A textbook. *Springer: Berlin* **2004**.
30. Boge, M. Proceedings of EPAC. *France* **2002,** (39-43).
31. Kim, K. J., X-ray Data Booklet. *Lawrence Berkeley Laboratory, University of California* **1986**.
32. Paul Sherrer Institute. About Swiss Light Source-SLS. http://www.psi.ch/sls/about-sls.
33. Bowers, M. T. Gas Phase ion Chemistry (III). *Academic Press, Orlando* **1984**.
34. Johnson, M.; Bodi, A.; Schultz, L.; Gerber, T. Vacuum Ultraviolet Beamline at the Swiss Light Source for Chemical Dynamics Studies. *Nuc. Inst. Methods* **2009,** *610*, 597-603.
35. Bodi, A.; Johnson, M.; Gerber, T.; Gengelliczki, Z.; Sztaray, B.; Baer, T. Imaging photoelectron photoion coincidence spectroscopy with velocity focusing electron optics. *Rev. Sci. Inst.* **2009,** *80* (3), 034101/1-034191/7.
36. Bodi, A.; Sztaray, B.; Baer, T.; Johnson, M.; Gerber, T. Data acquisition schemes for continuous two-particle time-of-flight coincidence experiments. *Rev. Sci. Inst.* **2007,** *78* (8), 084102/1-084102/7.
37. Bodi, A.; Hemberger, P.; Gerber, T.; Sztaray, B. A new double imaging velocity focusing coincidence experiment: i^{2}PEPICO. *Rev. Sci. Inst.* **2012,** *83* (8), 083105/1-083105/8.

Chapter 3. Theory

  The data analysis of this work is in an essential part to understanding the important concepts behind the findings. For the data obtained from the ALS, two types of plots help characterize and identify products: kinetic profiles and photoionization spectra. Additionally, important terms and concepts for understanding the data are described. The computational data analysis and methods vary for the iPEPICO and i^2PEPICO experiments that are further described in this section.

3.1 ALS Data Analysis

  The experimental data obtained from the ALS produce a three-dimensional data set where the intensity of all the species observed is a function of reaction time, mass-to-charge (m/z) ratio, and photon energy. Fixing one variable, such as energy or time, reduces the dimensionality of the data. These so obtained two-dimensional images can now be reduced further to "normal" one-dimension plots that are the photoionization (PI) spectra and kinetic traces. This process is depicted in Figure 3-1.[1] The characterization of products begins through observing their kinetic time profiles and analyzing which species are primary products and which are secondary products. These plots are obtained through taking a vertical slice of the two dimensional images; intensity vs. kinetic time (ms) for a fixed m/z. The reaction time of the experiments are 150 ms and each data cycle initiates 20 ms before each laser shot is fired. Typically, in these experiments approximately 150-250 laser shots are collected at each photon energy.[1] The total number of laser shots for each experiment varies and depends on the photon energy range. The data of photon energy and kinetic time in combination with mass-to-charge ratio (m/z) is collected from the time-to-digital converter (TDC) from the micro-channel plates output.

  The analysis of the data begins with background subtracting the average pre-photolysis signal creating a mass spectrum that represents post-photolysis and continues through IGOR[2] Pro by using the in-house procedures developed by our Sandia collaborators. Since in each experiment there is a variation in photon flux of the light, the ion signal has to be normalized. This is done by measuring the ALS photocurrent through a calibrated vacuum ultra-violet (VUV) sensitive photodiode.

  The kinetic time trace plots help visualizing whether a fraction of the reactant of interest "depletes" at the onset ($t_0 = 0$ ms) of the reaction that is when the photolysis laser is firing. The kinetic time traces are ion signal intensity (S) as a function of time (t) at a specific m/z. This plot is then used to compare to the kinetic time trace plots of all the species seen throughout the reaction to identify primary or secondary chemistry. When the slope of the inverse reactant signal fits well to the slope of the forming species (reactive intermediates and/or byproducts), it is indicative of primary chemistry. When the formation of an observed species occurs past t_0, it is most likely secondary

chemistry and does not concern this research. It is possible that under certain conditions secondary chemistry can be as fast as primary reactions. Radicals of a reaction are very short lived and easily identified due to their kinetic time traces. They have a very sharp and quick increase followed by a fast decay after a few ms.

When the initial primary signals have been identified, further analysis occurs through the PI spectra, which are plots of ion signal intensity (S) as a function of photon energy (E) at a particular m/z. The next step is to characterize each of the signals. This is done using literature PI spectra of different species and comparing them to the specific signals. From these spectra the adiabatic ionization energy (AIE) can be obtained. When the shape of a reference photoionization spectrum of a species fits the experimental signal, a positive assignment is achieved. In some instances, there may be multiple species forming at one m/z. In this case, when the summation of multiple spectra matches the overall experimental signal, the multiple species can be identified as well. Additionally, when reference PI spectra are unavailable in the literature, there are two possible scenarios. One is if the species is commercially available, then we can measure its photoionization spectrum using the same procedure. Otherwise, we can simulate its spectrum within the Franck-Condon (FC) approximation discussed in the computational section of this chapter.
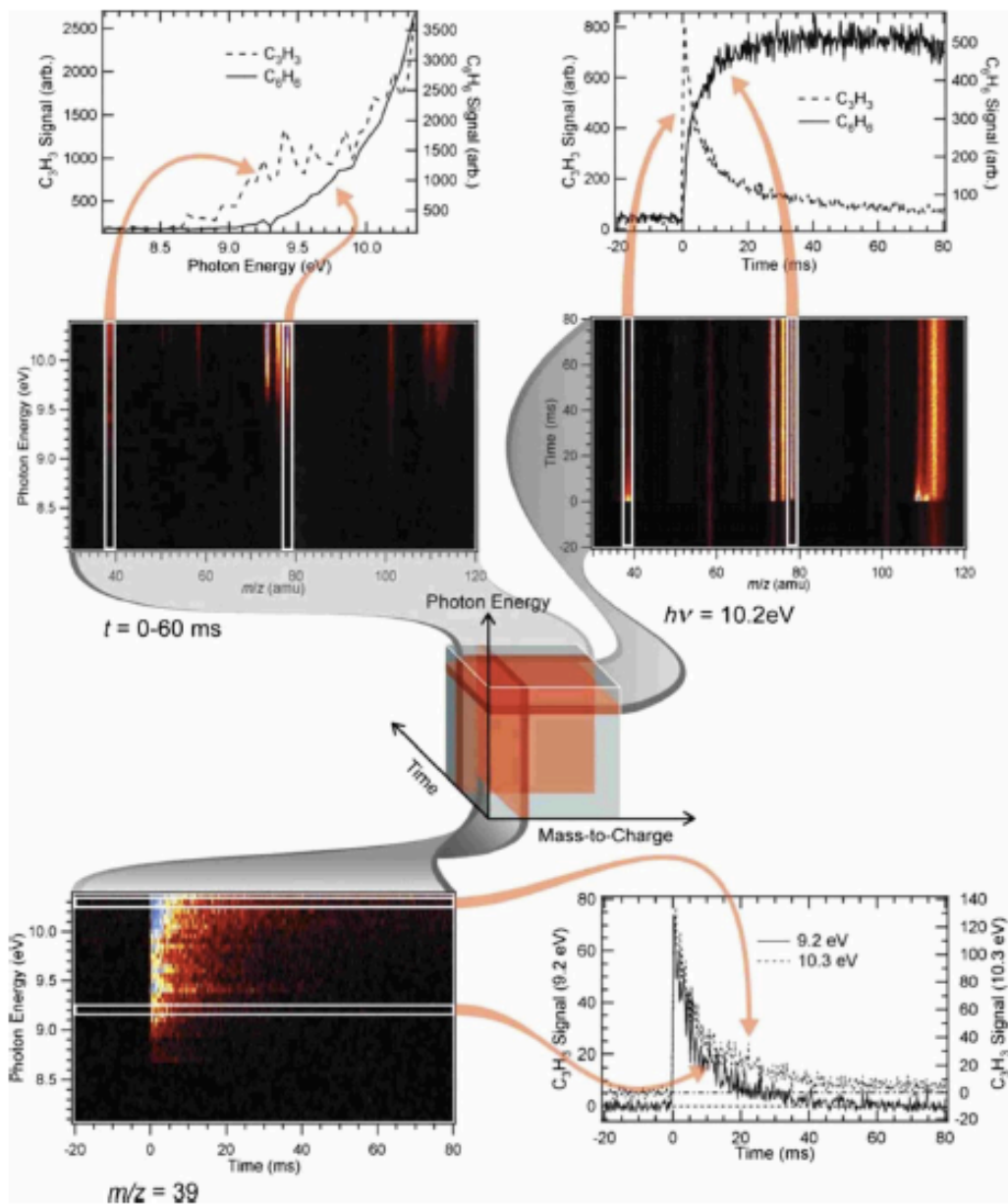
Figure 3-1. A schematic of the three-dimensional data block obtained from the ALS experiments where two-dimensional slices are taken along with their corresponding one-dimensional slice for actual analysis.[1]

3.2 Theoretical Concepts

3.2.1 Photoionization

When a molecule absorbs energy equal to or in excess to the energy needed for an electron to be removed, it ionizes. This required energy is referred to as the molecules ionization energy (IE). When a lone pair is involved, the ionization energies are lower because those electrons are more weakly bound. On the other hand, noble gases have the highest ionization energies of all atoms due to having closed electron shells. There are several ways for ionizing molecules; two common ways are electron ionization and photoionization. In the case of electron ionization, electrons are removed by collisions of energetic electrons with the system whereas electron removal occurs in photoionization through the interaction of an electromagnetic radiation with the system.[1-2]

In gas phase, when high energy level electrons bombard and transfer some of their energy onto the neutral state of a molecule, the specific electron ionization occurs.

$$M + e^- \rightarrow M^+ + 2e^- \tag{3.1}$$

When a molecule releases an electron while simultaneously absorbing a photon, it is undergoing photoionization.

$$M + h\nu \rightarrow M^+ + e^- \tag{3.2}$$

M represented a neutral species in the gas phase, h represents Planck's constant and v corresponds to the frequency of light. M^+ is the molecule cation resulting from the neutral species being ionized.

$$E = h\nu \tag{3.3}$$

represents the energy of the ionization radiation. According to the photoelectric effect ionization occurs only when $E \geq IE$.[1-2] The photoionization cross-section represents the effectiveness (cm^2) of a gaseous species that will interact with radiation (light) during ionization measured in Megabarns; $1Mb = 1 \times 10^{18} \, cm^2$).

Spectroscopically, the ionization energy can be defined as adiabatic. Adiabatic ionization energy (AIE) is used throughout the data analysis presented in this work. It represents the lowest energy value from the lowest electronic, vibrational, and rotational state of the neutral system necessary in order for electron removal to occur. The equation below expresses that the AIE of a

37

certain molecule, given that the enthalpy of formation of a neutral species is known, can be used to calculate the enthalpy of formation of the ion (M^+).

$$M + h\nu \rightarrow M^+ + e^- \qquad \Delta H_{rxn} = IE \qquad\qquad (3.4)$$
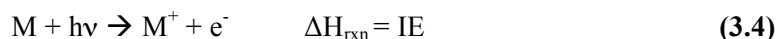
Vertical ionization energy (VIE) represents the most intense peak (large Franck-Condon factors, see below) in the first spectral band in a photoelectron spectrum.

When the photon energy exceeds the AIE of a particular molecule, the species may dissociatively photoionize producing fragmentation (daughter ions). In order to observe at what energy different fragments or dissociated species can arise, the appearance energy (AE) is calculated, which is the energy at which the dissociative species appears in the mass spectrum from the neutral molecules. This process is observed in equation 3.5 where AB presents the neutral molecule that dissociates into the ion, A^+, and neutral fragment, B.

$$AB \rightarrow A^+ + B + e^- \qquad\qquad (3.5)$$

The AE calculated in this way is only the thermochemical limit, which does not take into account any barrier for dissociation. To have an accurate computed AE value, the ionic potential energy surface should be investigated for possible barrier to dissociation.

3.2.2. Photoionization (PI) Spectra

As seen in Figure 3-1, these plots are obtained from taking a two-dimensional slice (intensity vs. photon energy (eV)) of the three-dimensional data block. Initially, primary products are characterized from observing their kinetic time traces; these plots are obtained from the three-dimensional block as well by fixing the photoionization energy that are intensity vs. time (ms). In Figure 3-2 three different time plots are presented that help characterizing products: a depleting reactant, a forming product, and a radical species. In Figure 3-3, the time trace of a primary product is superimposed onto the signal of the reactant (multiplied by -1) showing that the product is formed as fast as the reactant reacts (primary product).

(a)

(b)

39
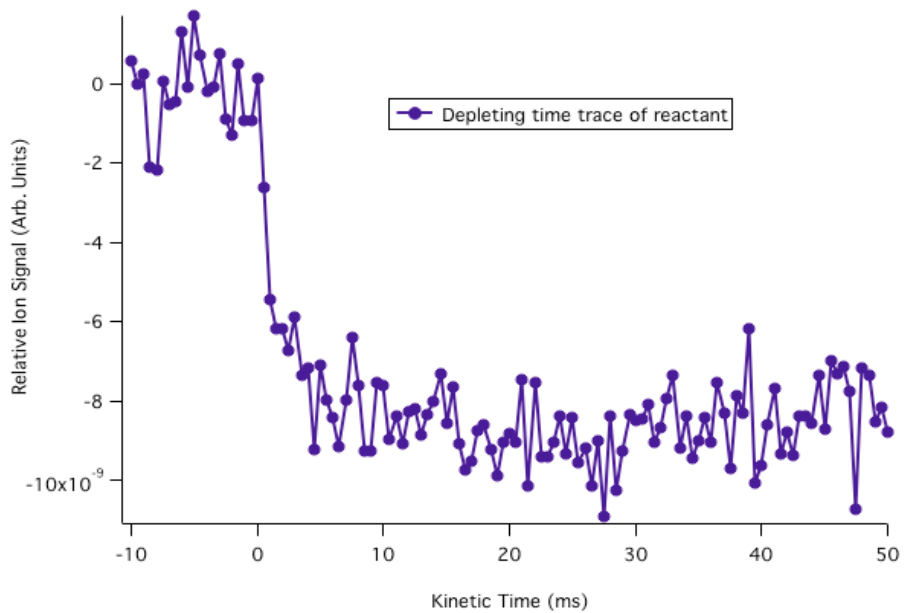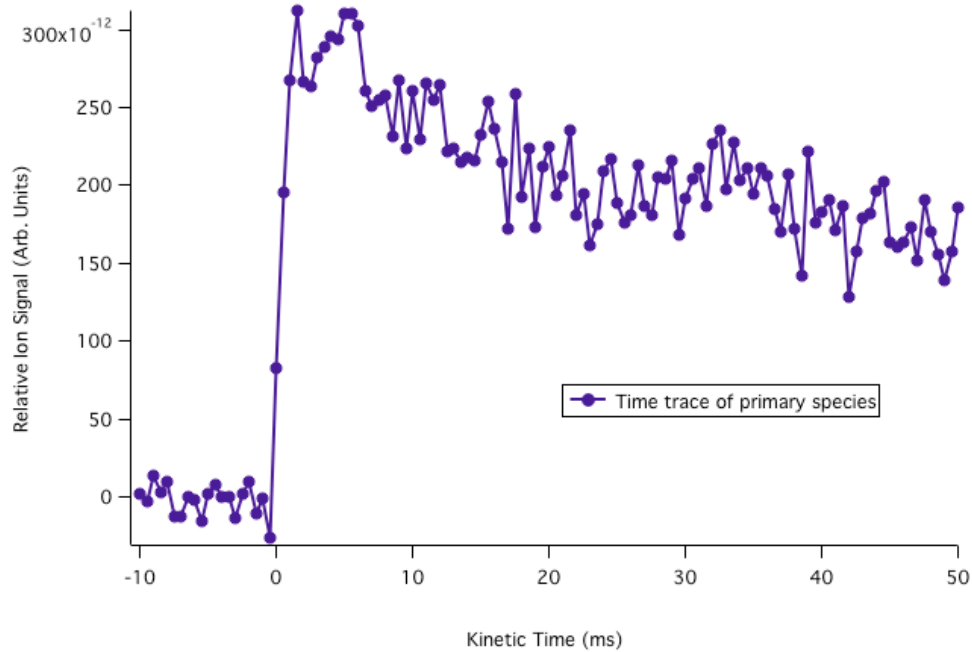
(c)
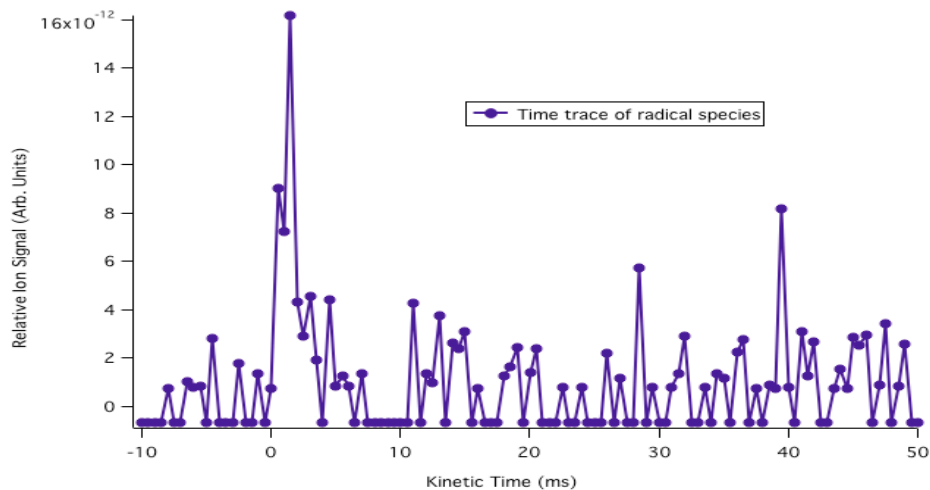
Figure 3-2. (a) It represents the time trace of a depleting reacting at $t_0 = 0$ ms. (b) It represents the time trace of a fast forming product at $t_0 = 0$ ms. (c) It represents the time trace of a radical species forming and fastly decaying.
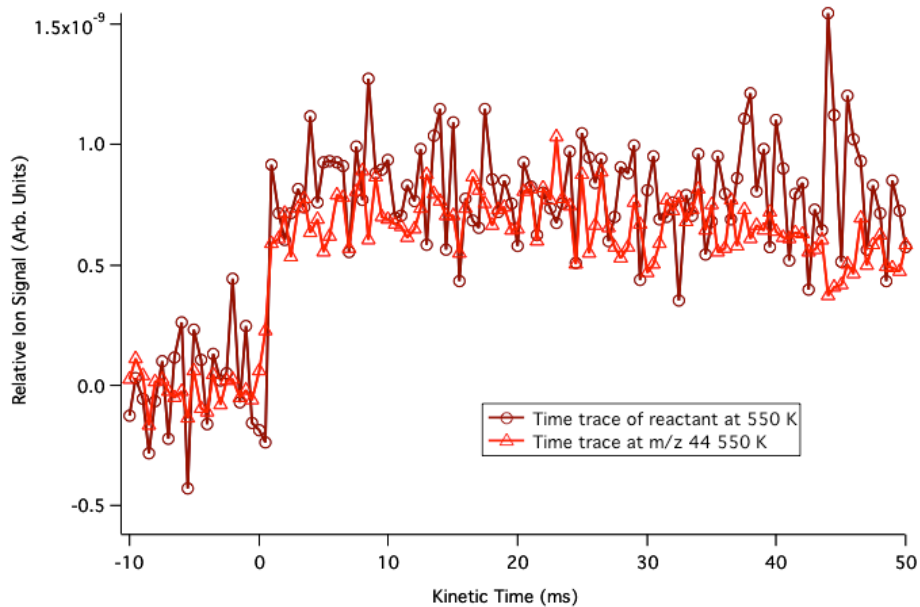
Figure 3-3. Characterizing a primary product observed in the data through superimposing its time trace onto the inverse time plot of the reactant species.

Once the primary species have been selected, the PI spectra help identify them. The photoionization spectrum of each species is unique, with a different ionization onset and shape, which is due to specific geometric parameters that make their Franck-Condon factors (see below) unique. There are several literature PI spectra of different molecules and when available these are used to identify the species. When the spectrum is not available, then a simulation within the FC approximation can be performed to obtain the photoelectron spectrum of the species, which by integration is converted into the photoionization spectrum.

In some instances multiple isomers or species can be present and the summation of their spectra can be used to fit the experimental data and further identify species. Since the PI spectrum of each isomer is directly related to its photoionization cross section, then the fractional abundance (A) of each can be found if the photoionization cross sections are known.[3]

$$A_1 + A_2 + A_3... = 1 \text{ thus } \sigma_{Total} = A_1\sigma_1 + A_2\sigma_2 + A_3\sigma_3... \qquad \textbf{(3.6)}$$

Figure 3-4 shows the comparison of an experimentally obtained spectrum at m/z 44 superimposed onto the reference PI spectra of ethenol and acetaldehyde reported by Cool et al.[3] The summation of the species fit the overall shape of the experimental photoionization curve, which confirms the presence of these two species.
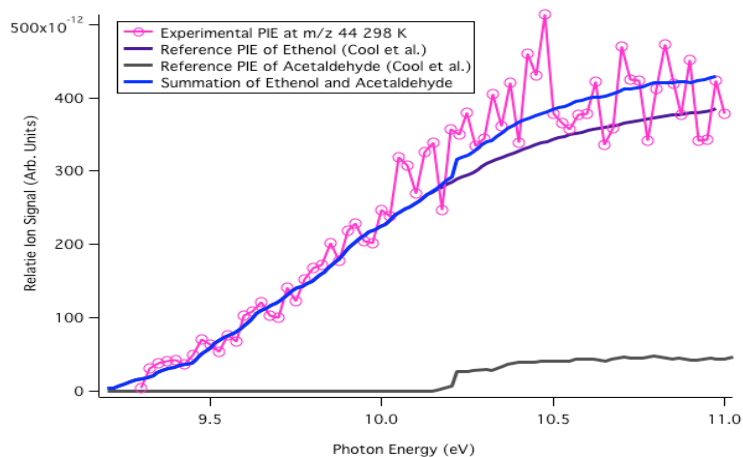
Figure 3-4. The reference PI spectra of ethenol (purple) and acetaldehyde (gray) superimposed onto the experimental PI spectrum of m/z = 44 (pink open circles). The summation (blue) of the two species fit the overall experimental curve.[4]

The ion signal (S(E)) is a function of the photon energy and is proportional to the photoionization cross section ($\sigma(E)$) as equation 3.7 shows:

$$S(E) = k\sigma(E)C\delta \qquad (3.7)$$

where k is the instrumentation constant, C is the concentration of the species, and δ is the mass discrimination factor, which is approximately equal to the mass (m) of the species to the power of 0.67.[5] This factor takes into account how efficiently the detector can detect a species. The photoionization-cross section ($\sigma(E)$) represents the area in which there is the highest probability to ionize the system.[6]

3.2.3. Photoionization Cross Sections

In theory, when a neutral atom or molecule in the gas phase absorbs a photon, an electron is removed if the photon energy is equal or greater than the energy binding the electron to the system. Thus, the possibility of a certain electron removal is directly proportional to the number of photons hitting the specific atom or molecule. In reality, it is more complex than this. The experimental incident flux from states i to j is directly related to the number of photons that are absorbed per unit time (power), equation 3.8,[7-8] where P is power, I is the intensity, c is the speed of light, n_ω is the average number of photon, σ is the photoionization cross section, T_{ij} is determined using Fermi's Golden rule that calculates the density of the final states, and ω represents the frequency interval.[7-8] Due to this, the photoionization cross section is commonly known as the likelihood in which the molecule can potentially ionize when it comes in contact with a photon beam of a particular frequency.

$$\sigma = \frac{P}{I} = \frac{\pi^2 c^2}{n_\omega \omega_{ij}^2} T_{ij} \qquad (3.8)$$

The equation 3.9 shows how the photoionization cross section of a target molecule ($\sigma_T(E)$) can be derived from the observed ion signals ($S_T(E)$ and $S_R(E)$), known concentrations (C_T and C_R) and known photoionization cross section of the reference molecule ($\sigma_R(E)$). The signals and photoionization cross-sections in this work are obtained at 11 eV.

$$\sigma_T(E) = \frac{\sigma_R(E)S_T(E)C_R m_R^{0.67}}{S_R(E)C_T m_T^{0.67}} \qquad (3.9)$$

When a signal in a PI spectrum comprises of several species, the total photoionization cross section of the measured signal can be calculated based on the additivity rule:

$$\sigma_T = \sum_{i=1}^{n} x_i \, \sigma_i \qquad\qquad\qquad where, \sum_{i=1}^{n} x_i = 1 \qquad\qquad (3.10)$$

where x_i represents the mol fraction of the ith isomer and σ_i is the photoionization cross-section of the ith isomer.

Once a particular m/z is fully characterized, it is essential to determine how much of each of the products is actually forming throughout the particular oxidation. This is done through comparing the concentration of the product to the concentration of the reactant, also referred to as branching fraction. This ratio is equal to:

$$\frac{C_p}{C_R} = \frac{S_P \sigma_R \delta_R}{S_R \sigma_P \delta_R} = \frac{S_P \sigma_R (m_R)^{0.67}}{S_R \sigma_P (m_P)^{0.67}} = \frac{S_P \sigma_R}{S_R \sigma_P} * MDF \qquad\qquad (3.11)$$

The branching fractions in equation (3.11) are derived measuring the ratio of the concentration of the product (C_P) divided by the concentration of the reactant (C_R) at a specified photon energy (11 eV) that is equal to the ratio of the product of the ion signal (product, S_P, and reactant, S_R), the photoionization cross-section (product, σ_P, and reactants, σ_R), and the mass discrimination factor (MDF).[9]

3.2.4 Franck-Condon Factors

As previously mentioned, in some cases reference photoionization spectra are unavailable in order to further characterize the observed species. When this occurs, a simulation within the Franck-Condon approximation can be carried out on a particular structure that has an AIE identical to the experimentally observed AIE. The concepts behind these simulations refer to the Born-Oppenheimer approximation and the Franck-Condon principle. When a molecule is ionized, its bond length and position do not change because nuclei are fixed with respect to electron motion, possessing equal momentum. The Born-Oppenheimer approximation therefore suggests that the velocity of the electron is very fast suggesting that the motion of atomic nuclei and electrons in a molecule can be separated.[5,10,11] This is concluded due to the heavier mass of the nuclei compared to the mass of the electron.[5,10,11] For this reason, the wavefunction can be factored into vibrational and rotational components to solve for nuclear and electronic transitions independently. When the molecule

undergoes ionization and thus reaches its final state the electronic transitions occur, usually represented by E'$_1$ → E''$_0$. This transitions indicates a small Franck-Condon overlap of the neutral and its corresponding cation.[11,12] The maxima is where the highest chance of an electronic transition is achieved, according to the Franck-Condon principle.[5,10,11] When there is an electronic transition of E'$_1$ ← E''$_0$, no vibrational peak is present due to this small overlap between states.

As mentioned earlier, the adiabatic ionization energy (AIE) is thus the energy difference between the ground states of the neutral and cation. The AIE can be calculated through the CBS-QB3 composite method in Gaussian 09 described later in this chapter. The Franck-Condon simulation is used to generate a photoelectron spectrum and its integration will provide the simulated photoionization spectrum, which can be compared to the experimental photoionization curve at the specific signal for further product identification. Specifically, the Franck-Condon (FC) and Franck-Condon-Herzberg-Teller methods[14,15,16] are employed. The FC overlap integrals are calculated using recursive formula developed by Ruhoff.[17] Figure 3-5 shows an example of a simulated Franck-Condon photoelectron simulation of 2-methylfuran, then an integrated simulation that is later used to further identify species, and the literature PI spectra to indicate how accurate the computational calculations are.

(a)
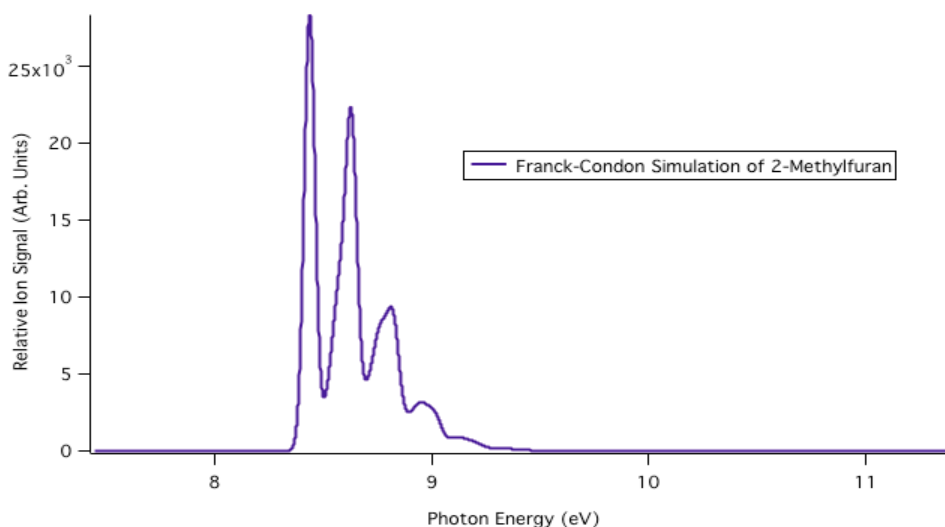
(b)
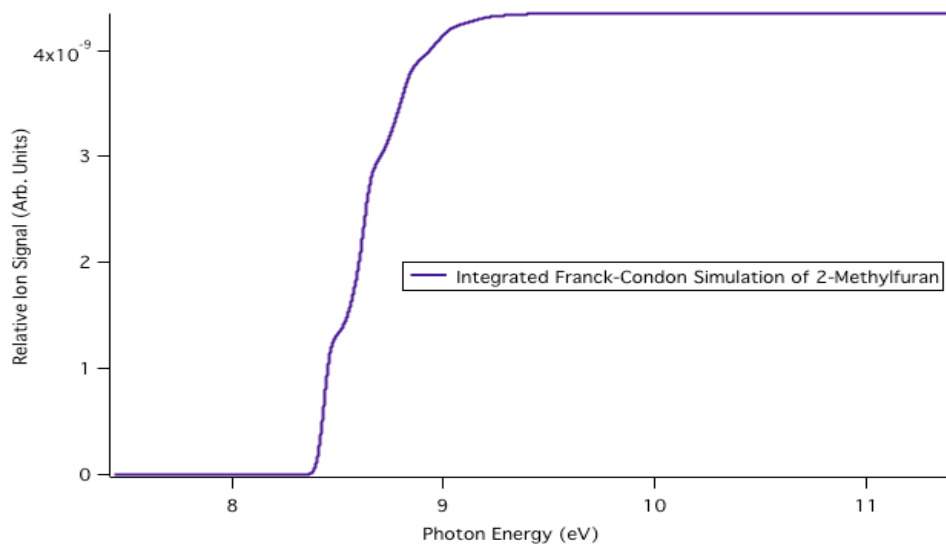
(c)
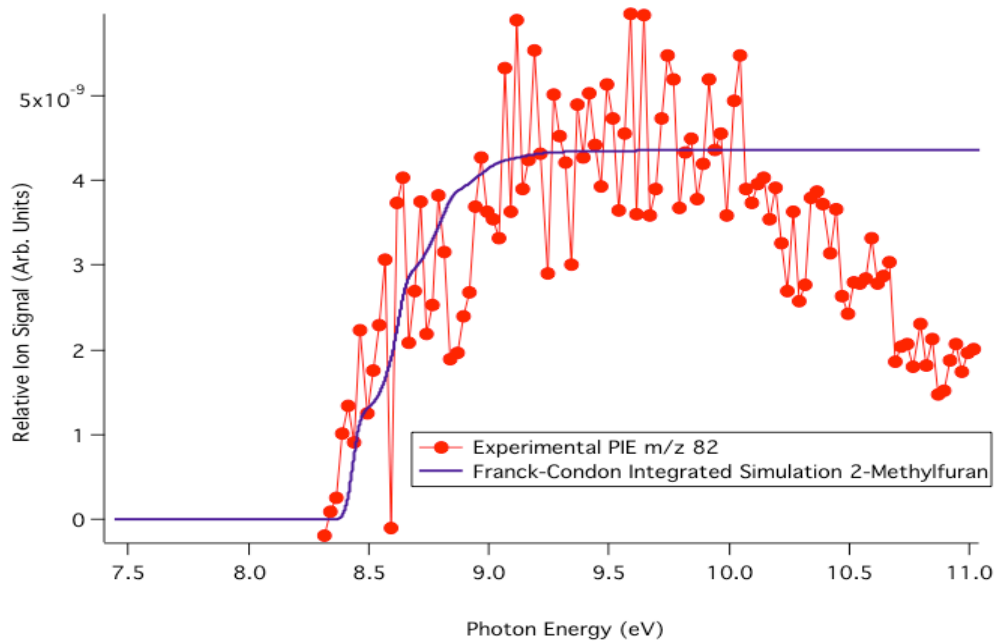
Figure 3-5. (a) Calculated Franck-Condon photoelectron spectrum simulation of 2-methylfuran. (b) Integrated Franck-Condon simulation to generate a PI spectrum curve of 2-methylfuran. (c) Integrated Franck-Condon simulation of 2-methylfuran superimposed onto the experimental PIE of m/z 82.

3.3 Electronic Structure Calculations

The studies reported in this thesis all make use of computational methods to help in the reaction species identification. The Gaussian 09 program[18] is utilized to carry out electronic structure calculations to optimize molecular parameters using the complete basis set CBS-QB3[19-21] composite method along with Gaussian-4 (G4) theory. G4 was used for the computational calculations of the PEPICO experiments; in a sequence of Gx methods it is the fourth series to calculate molecular energies with an error of 1.19 kcal/mol.[22-23] In order to obtain the total energy of a particular atom or molecule, this method performs several energy calculations; Møller-Plesset perturbation theory and coupled cluster theory. These theories are performed up to the fourth order for the G4 calculations. There are three basis sets used in G4 theory; G3LargeXP, quadrupole-zeta, quintuple-zeta. The last two basis sets are used for extrapolation to the Hartree-Fock limit to eliminate any error.[22-23] Throughout the calculation, the specific molecule or atom is polarized to 3d (1st row atoms) and 4d (2nd row atoms). The polarization thus permits this specific method to calculate the geometries and zero-point energies obtained at the B3LYP/6-31G(2df,p) level to account for deficiencies in radicals.[22-23]

The adiabatic ionization energy (AIE) of a specific molecule is calculated using the zero-point vibrational corrected total electronic energy (E_0) obtained through optimization calculations of the neutral and cation of a particular species, i.e., AIE = E_0 (cat) - E_0 (neutral). The calculated AIE of a molecule is also used in generating Franck-Condon (FC) spectral simulations. Specifically, AIE predicts the onset of the curve (an increase in signal from the baseline), and the FC factors predict the general shape of the spectrum.

CBS-QB3 is known to provide reliable geometries and accurate energetics. Bond distances and harmonic vibrational frequencies were optimized at the Becke three-parameter exchange functional with Lee, Yang and Parr correlation functional (B3LYP) level of theory and all electron 6-311+G* basis set. CBS-QB3 consists of different level of theory (ab initio and density functional) that help overcome the greatest amount of error, also referred to as the basis set truncation error, in electronic thermochemical calculations through using a linear combination of atomic orbitals (LCAO-MO) approximations.[19-21]

CBS-QB3 is the main computational methodology used throughout this work in order to perform geometry optimization of specific structures, as well as perform frequency and energy calculations. This method is used due to the low estimated energy error of 1-1.5 kcal/mol according to Sirjean et al.[24] Previously in this section, it was shown that the ionization energy obtained from photoionizing a species is equal to the enthalpy of the ionization reaction. The AIE is calculated from the difference between the zero-point energy corrected total electronic energies (ZPE) of the neutral

and cationic optimized species, displayed in the equation below. These values help obtain the AIE of a species as well as the heat of the reaction, helping in analyzing the experimental data.

$$AIE = ZPE_{ion}^{CBS-QB3\ optimization} - ZPE_{neutral}^{CBS-QB3\ optimization} \qquad (3.12)$$

$$\Delta H_{rxn} = \sum ZPE_{P}^{CBS-QB3\ optimization} - \sum ZPE_{R}^{CBS-QB3\ optimization} \qquad (3.13)$$

3.4 Potential Energy Surface Scan using B3LYP Basis Set

A big part of this research is explaining the formation of specific reaction species, i.e., products and reactive intermediates, through thermodynamic and kinetics considerations. As mentioned before, the CBS-QB3 composite method is used to calculate the most accurate energy value of the species. In order to calculate whether the different pathways from the reactant to the different products have barriers, a potential energy surface scan is run on each optimized structure. B3LYP is a specific density-functional theory using the Hohenberg-Kohn theorem to calculate molecular energy at its ground state.[25] The theoroem along with molecular energy also calculates the wave function in the ground state of a molecule, it is related to the ground-state electron probability density, ρ_0 (x,y,z).[25]

In each particular reaction, molecules will have hydrogen transfers, bond stretching or breaking in order to form the desired products identified through their PI curves. Once a species has reached the lowest possible vibrational electronic level, it occupies its ground vibronic state (Ψ'_0), which is referred to as the global minimum in a PES (potential energy surface) scan. The global minimum is the preferred structure in a PES scan because it the most energetically favorable conformation, i.e., the lowest energy state. In figure 3-6 a GaussView[26] example is given of the structure at the global minimum and saddle point of a particular PES scan. The first saddle point is the highest point in a PES scans also known as the transition state. This "high-energy" species is also referred to as activation complex. When there is a barrier in a PES scan, in order to obtain the correct thermodynamic energy the particular structure at the saddle point is calculated using the CBS-QB3 composite method. Indeed, each global minimum as well is saved and calculated again using the CBS-QB3 composite method to find the exact zero-point corrected total electronic energy value. All the structures present in the potential energy surface scan are calculated using the CBS-QB3 composite method to be consistent with the reliable energetics.
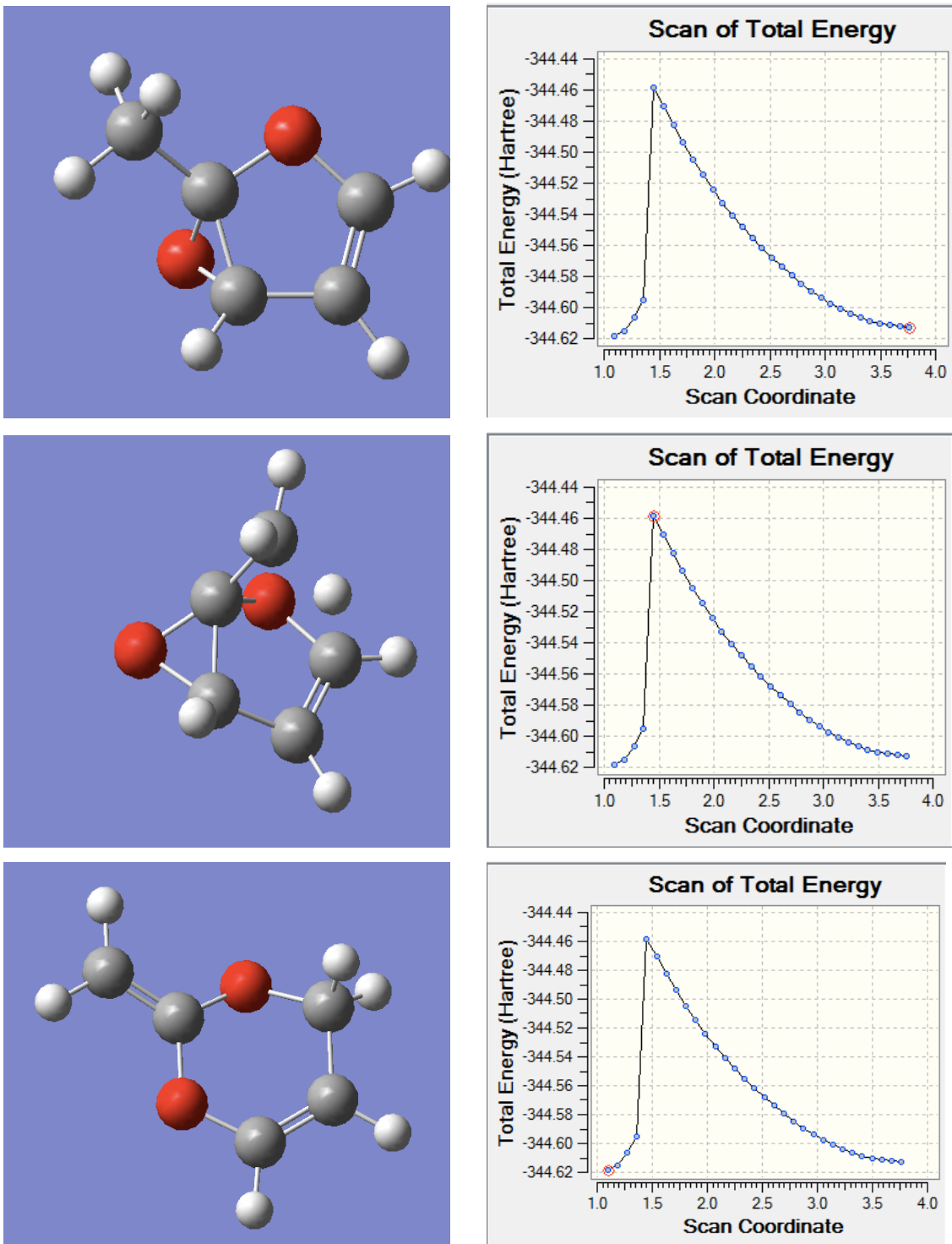
Figure 3-6. A PES scan resulting from a B3LYP calculation. (a) The starting, (b) the saddle point, (c) the minima, ending structure.

3.5 Photoionization and Photodissocation Theories

3.5.1. Isomerization and Unimolecular Dissociation

The analysis of molecules photodissociation takes into account the cation formed from the neutral species. The ionization of cation compared to a neutral species is fast due to nuclear or bond shifts of the neutral species. A cation forms when an electron is removed from the neutral molecules, as motioned before. However, the energy of the electromagnetic wave is greater than the energy of electron removal thus forming the corresponding ion. When analyzing the dissociation, a cation can be bound or unbound. When unbound, it is continually dissociating at the threshold. When analyzing the dissociation, the geometry of the neutral and cation can be identical due to vertical transition and a simple PES scan on a neutral species may give a global minimum that may not be completely accurate.

Molecules undergo photodissociation when there is enough internal energy due to an increase in photon energy to fragment (Equation 3.14).[27]

$$AB + h\nu \rightarrow AB^+ \rightarrow A^+ + B \tag{3.14}$$

The neutral molecule AB is ionized forming the parent molecular ion AB^+, which then photodissociates to form the experimental detected daughter ion is A^+ and releases the neutral fragment referred to as B in the above equation. In the experimentation, only the cationic species of reactions are observed, in mass spectrometry neutral species are not detected.

In this particular work, the dissociation of the three isomer of interest had no barrier forming three-daughter isomers in their ionic states. Indeed, the potential energy pathway is "uphill" and the energy needed to form the daughter ion is termed as the bond dissociation energy (BDE) which equals to the energy at which the daughter isomers are first detected also referred to as the appearance energy (AE). The BDE is simply calculated from the energy difference between the fragments and parent species. This energy value along with the summation of the AIE of the particular species essentially provides the appearance energy needed to produce the daughter ion of the photodissociation (again, if no dissociation barrier is present).

$$BDE = E_{Fragments\ Species} - E_{Parent\ Species} \tag{3.15}$$

$$AE = BDE + AIE \tag{3.16}$$

3.5.2 Thermodynamics and Photodissociation

From the appearance energies, useful thermochemical values of the neutral or cationic species of the investigated molecule can be calculated using the equation below:[28-29]

$$\Delta_r H_{0K}^o = AE = \Delta_f H_{0K}^o(A^+) + \Delta_f H_{0K}^o(B) - \Delta_f H_{0K}^o(AB) \qquad (3.17)$$

$$\Delta_f H_{0K}^o(A^+) = AE - \Delta_f H_{0K}^o(B) + \Delta_f H_{0K}^o(AB) \qquad (3.18)$$

When thermochemical information (heats of formation) for several of the species are known, the equation along with the appearance energy, which is the heat of the reaction for the formation of the neutral and cation fragment, can be used to find the heat of formation of the unknown.

3.5.3 Computational Modeling for PEPICO

Photoelectron photoion coincidence spectroscopy as discussed in the previous chapter measures photoionization mass spectra and photoelectron spectra of gas phase molecules. In PEPICO experiments specifically, the photoelectrons ejected and particular ions are detected in coincidence and act as a time stamp for the ion time-of-flight distributions that provide kinetic information. In order to observe and identify fragments, many researchers use synchrotron photoionization mass spectrometry to report potential mechanisms that come into play for molecular photodissociaiton.[30-31] In order to visualize and find the amount of energy required for a particular species to photodissociate the energy is represented by the different between the AIE of the parent species ($E_{ZPE\ Neutral} - E_{ZPE\ Cation}$) and the experimental AE of the forming daughter ion. Breakdown diagrams take into account fractional abundance of each ion detected as a function of photon energy and are a better visualization of the photodissociation behavior of different species.

MiniPEPICO[32] is computational software designed by Stzaray, Bodi and Baer that calculates the density and number of state functions creating a plot as a function of photon energy. The unique aspect of this program is that it takes into account the rates of photodissociation that can be extracted using Rice, Ramsperger, Kassel, and Marcus's RRKM theory.
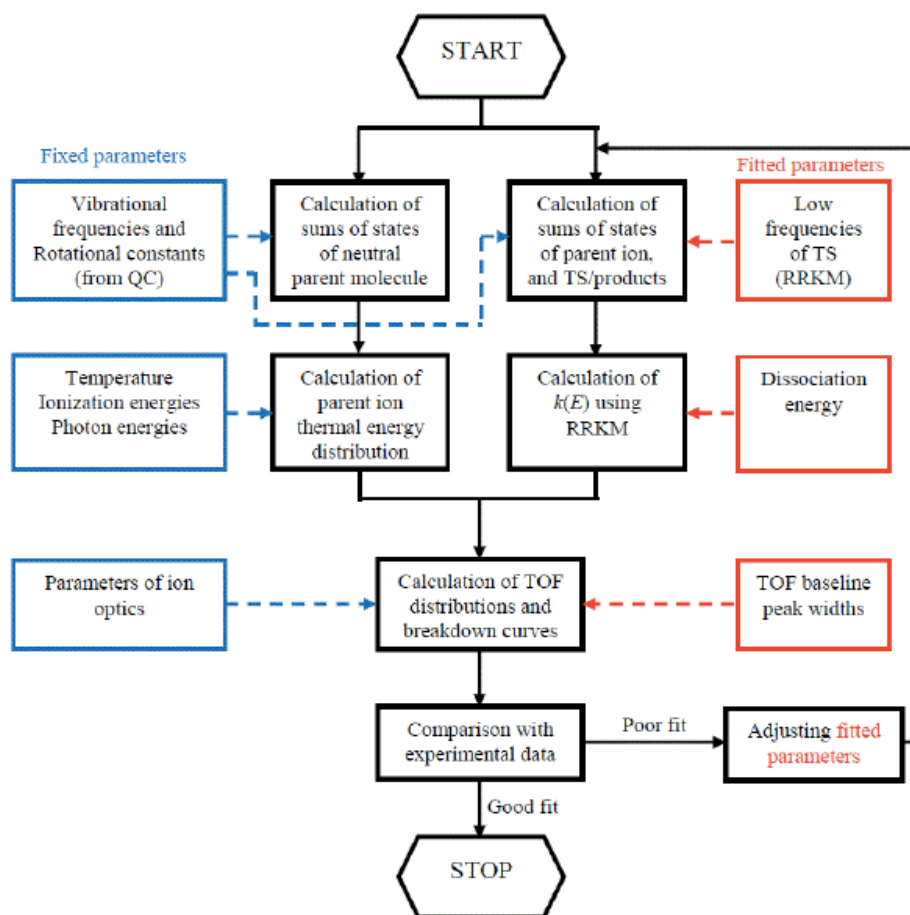
Figure 3-7. A diagram showing the steps and theories used in unimolecular reaction for the MiniPEPICO program.[33]

The process to obtain accurate bond dissociation energies is represented in Figure 3-7. It enables the experimental dissociation rates to be extracted using vibrational transition state theory (VST)[34], simplified statistical adiabatic channel model (SSACM)[35], and Rice, Ramsperger, Kassel and Marcus's RRKM theory.[33,36,37] The rate constant is a function of internal energy (E), number of states of the energy that lies above the barrier to dissociate the species, the density ($\rho(E)$) of the states, Planck's constant and reaction degeneracy ($\hbar$)[38].

$$k(E) = \frac{\sigma N(E - E_0)}{\hbar\rho}(E) \tag{3.19}$$

In order for a breakdown diagram to be modeled, specific electronic structure calculations are performed similar to those described earlier. The input of the miniPEPICO program requires the

vibrational frequencies of the optimized neutral and cationic parent species. In this work, the vibrational frequencies were obtained using the G4 composite method to optimize and calculate the correct zero-point energy, Additionally, from the neutral output the rotational constants are obtained as well to input into the program. A PES scan is using B3LYP to observe whether there is a barrier to dissociate the ion, and TS calculations using G4 are performed to obtain the vibrational frequencies of the TS. The theoretical breakdown diagram created by the program is fitted to the experimental breakdown diagram, helping to determine the most accurate appearance energy for further analysis. There are two types of dissociations that occur throughout these types of experiments; slow and fast (Figure 3-8). When the parent ion travels through the drift tube and does not dissociate immediately, it undergoes a slow dissociation. In the case of the fast dissociation, the parent ion dissociated instantaneously.

(a)
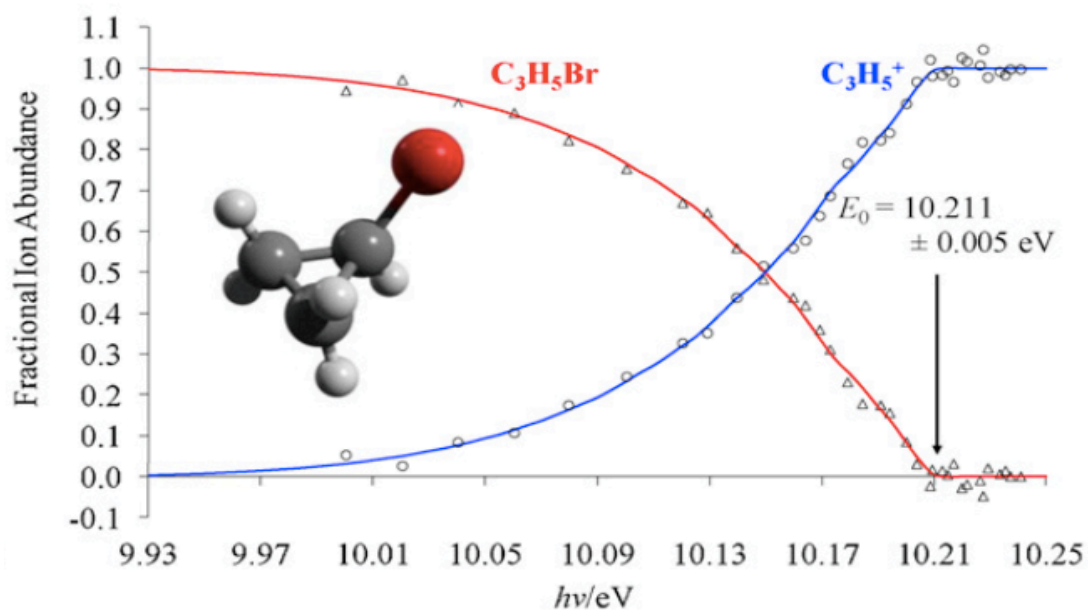
(b)
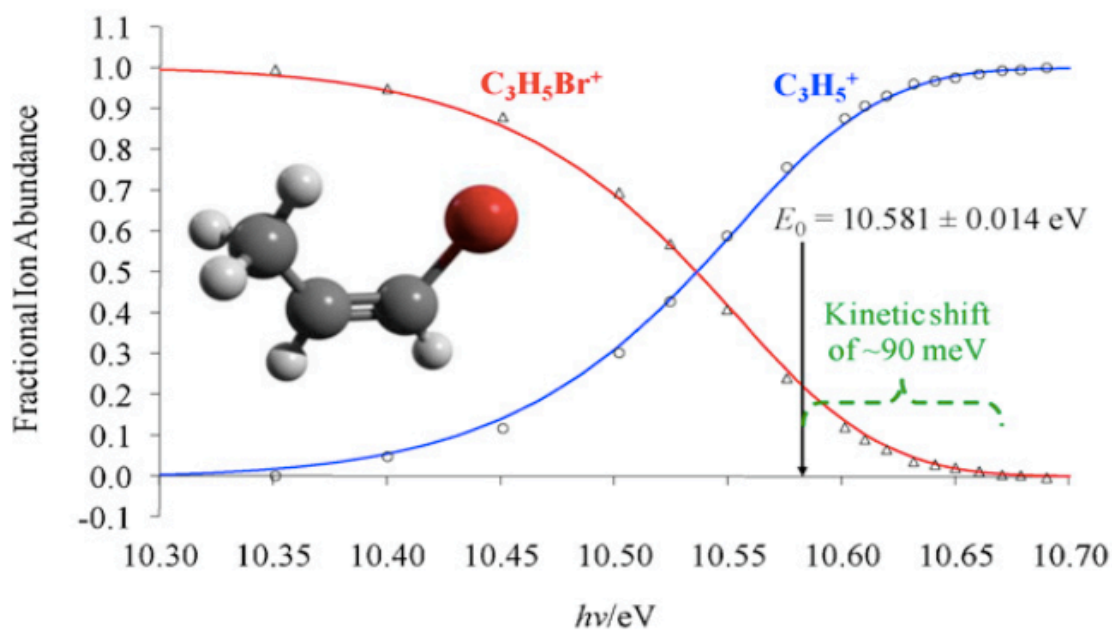
Figure 3-8. a) Breakdown curve of the fast dissociation of bromine from bromocyclopropane. b) Breakdown diagram of the slow dissociation of the bromine loss from cis-1-bromopropene.[39]

The 0 K appearance energy is obtained from fitting the statistical model of the breakdown diagram of fast dissociations or the breakdown diagram together with the time-of-flight distributions for slow dissociations. For fast reactions, there are no time-of-flight distributions analyses; the data analysis is only dependent upon the breakdown diagram. This is because if the reaction involves only a single product ion, there is 0 K dissociation limit and the thermal energy distributions help determine the approach to the limit using only the breakdown diagram. In the case of slow dissociations, it is essential to fit the breakdown diagram with the time-of-flight distributions. The TOF will exhibit an asymmetric fragment ion peak shape, the modeling of which will provide the absolute rate constants, Figure 3-9.
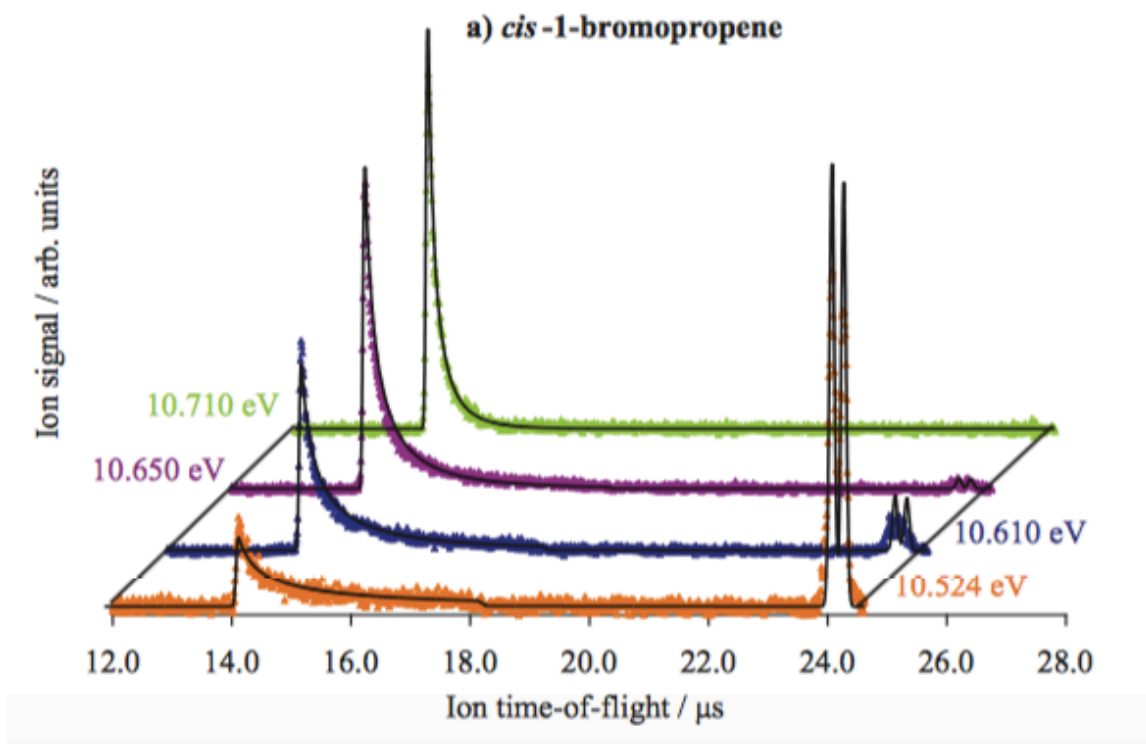
Figure 3-9. The asymmetric time-of-flight distribution due to the slow dissociation Bromine atom loss from cis-1-bromopropene.[39]

In order to do so, the hot electron time-of-flight spectrum needs to be subtracted from the central electrode in order for the parent and daughter ion to appear. In order to visualize the data bet, the channels numbers from the experiment are multiplied by at least 10. Therefore, the ion peak positions can be located to the nearest channel number and the peaks line up through scaling the hot electron TOF spectrum. Another approach is to work with the original TOF data meaning having to determine the fractional part of each hot channel that needs to be subtracted from the central TOF spectrum so that the total counts are preserved. For molecules undergoing a slow dissociations, not all parent ions above the barrier dissociate within the time of the experiment thus a kinetic shift occurs and the following equation has to be taken into account.

$$BD(h\nu) = \int_0^{E_0-IE} P_i(e,h\nu)dE \cong \int_0^{E_0-h\nu} P_n(E)dE \qquad (3.20)$$

3.6 References

1.   Osborn, D. et al. The multiplexed chemical kinetic photoionization mass spectrometer: A new approach to isomer-resolved chemical kinetics. *Rev. Sci. Inst.* **2008**, 79.
2.   Atkins, P. Physical Chemistry 9th ed. *Great Brittain: Oxford University Press.* **2010**.
3.   Cool, T. A.; Nakajima, K.; Mostefaoui, T. A. Selective detection of Isomers with Photoionization mass spectrometry for studies of hydrocarbon flame chemistry. *J. Chem. Phys.* **2003,** *119* (16), 8356-8365.
4.   T.A. Cool, e. al. *J. Chem. Phys.* **2003,** *119* (16), 8356-8365.
5.   Savee, J. D.; Satchin, S.; Welz, O.; Selby, T.M.; Taatjes, C.A.; Osborn, D.L. Absolute Photionization Cross-Section of the Propargyl Radical. *J. Chem. Phys.* **2012,** *136* (13), 134307/1-134307/10.
6.   Lee, P. W. et al. The Photoionization Cross-Section of Neon. *P. Roy. Soc. Lond. A Mat.* **1953,** *220*, 71-76.
7.   Pradhan, A. K.; Nahar, S. N. 6.2 Photoionization Cross Section, in Atomic Astrophysics and Spectroscopy. *Cambridge University Press: Cambridge, UK* **2011**.
8.   Demtroder, W. Continuous Absorption and Emission Spectra in Atoms, Molecules and Photons. An Introduction to Atomic-, Molecular-, and Quantum Mechanics 2nd Ed. *Springer-Verlag: Berling, Germany* **2006**.
9.   Welz, O. et al. Low-Temperature Combustion Chemistry of Biofuels: Pathways in the Initial Low-Temperature (550 K - 750 K) Oxidation Chemistry of Isopentanol. *Phys. Chem. Chem. Phys.* **2012**, 14.
10. Born, M.; Heiseinberg, W. Zur Quantentheorie Der Molekeln. *Annalen der Physik* **1927,** *389*, 457-484.
11. Seiler, R. A Remark on the Born-Oppenheimer Approximation. *Int. J. Quant. Chem.* **1969,** *3*, 25-32.
12. Franck, J.; Dymond, E. G. Elementary Processes of Photochemical Reactions. *Trans. Faraday Soc.* **1926,** *21*, 536-542.
13. Condon, E. A Theory of Intensity Distribution in Band Systems. *Phys. Rev.* **1926,** *28*, 1182-1201.
14. Duschinsky, F. Physicochim. *URSS* **1937,** *7* (551-566).
15. Lerme, J. Iterative Methods to Compute One- and Two-Dimensional Franck-Condon Factors. Tests of Accuracy and Application to Study Indirect Molecular Transitions. *Chem. Phys.* **1990,** *145*, 67-88.
16. Sharp, T. E.; Rosenstock, H. M. Franck-Condon Factors for Polyatomic Molecules. *J. Chem. Phys.* **1964,** *41*, 3453-3463.
17. Ruhoff, P. T. Recursion Relations for Multi-Dimensional Franck-Condon Overlap Integrals. *Chem. Phys.* **1994,** *186*, 355-374.
18. Firsch, M. J. e. a., Gaussian 09. *Revision A. 1 Wallingford* **2009**.
19. Ochterski, J. W.; Petersson, G.A.; Montgomery, J.A. A complete basis set model chemistry. V. Extensions to six or more heavy atoms. *J. Chem. Phys.* **1996,** *104*, 2598-2619
20. Montgomery, J. A.; Frisch, M. J.; Ochterski, J. W.; Petersson, G. A. A complete basis set model chemistry. VI. Use of density functional geometries and frequencies. *J. Chem. Phys.* **1999,** *110* (6), 2822-2827
21. Montgomery, J. A.; Frisch, M. J.; Ochterski, J. W.; Petersson, G. A. A complete basis set model chemistry. VII. Use of the minimum population localization method. *J. Chem. Phys.* **2000,** *112* (15), 6532-6542.
22. Curtiss, L. A.; Redfern, P. C.; Raghavachari, K. Gaussian-4 Theory. *J. Chem. Phys.* **2007,** *126*, 084108.

23.   Curtiss, L. A.; Redfern, P. C. Assessment of Gaussian-3 and Density Funcitonal Theories on the G3/05 Test Set of Experimental Energies. *J. Chem. Phys.* **2005,** *123*, 12.

24.   Sirjean, B.; Rene, F.; Glaude, P-A.; Ruiz-Lopez, M.F. Extension of the Composite Cbs-Qb3 Method to Singlet Diradical Calculations. *J. Chem. Phys. Lett.* **2007,** *435*, 152-156.

25.   Hohenberg, P.; Kohn, W. Inhomogeneous Electron .*Gas. Phys. Rev.* **1964,** *136*, B864-B871.

26.   Dennington, R. Keith, T.; Millam, J. GaussView 2009. *SemiChem Inc. Shawnee Mission, KS* **2009**.

27.   Baer, T.; Bodi, A.; Sztaray, B. Photoelectron-Photoion Coincidence Methods in Mass Spectrometry (PEPICO). *Ref. Mod. Chem., Molec. Sci. and Chem. Eng.* **2014**.

28.   Borkar, S.; Sztaray, B. Self-Consistent Heats of Formation for the Ethyl Cation, Ethyl Bromide, and Ethyl Iodide from the Threshold Photoelectron Photoion Coincidence Spectroscopy. *J. Phys. Chem. A.* **2010,** *114* (20), 6117-6123.

29.   Shuman, N. et al. Heat of formation of the allyl ion by TPEPICO spectroscopy. *J. Phys. Chem.* **2009,** *113* (40), 10710-10716.

30.   Smith, A. R. Absolute Photoionization Cross-Section of Furanic Fuels: 2-ethylfuran, 2-acetylfuran, and furfural. *J. Mass. Spec.* **2015,** *50*, 1206-1213.

31.   Wei, L.; Yang, B.; Wang, J.; Huang, C.; Sheng, L.; Zhang, Y.; Qi, F.; Lam, C.; Li, W. Vacuum Ultraviolet Photoionization Mass Spectrometric Study of Ethylenediamine. *J. Phys. Chem.* **2006,** *110*, 9089-9098.

32.   Sztaray, B.; Bodi, A.; Baer, T. Modeling unimolecular reactions in photoelectron photoion coincidence experiments. *J. Mass Spec.* **2010,** *45*, 1233-1245.

33.   Marcus, R. A; Rice, O. K. The kinetics of the recombination of methyl radicals and iodine atoms. *J. Phys. Coll. Chem.* **1951,** *55*, 894.

34.   Hase, W. L. Variational unimolecular rate theorry. *Acc. Chem. res.* **1983,** *16*, 258.

35.   Baer, T. Unimolecular Reaction Dynamics: Theory and Experiments. *Oxford University Press. New York* **1996**.

36.   Rice, O. K.; Ramsperger, H. C. Theories of unimolecular reactions at low pressures II. *J. Am. Chem. Soc* **1927,** *49* (1617).

37.   Rice, O. K.; Ramsperger, H. C. Theories of unimolecular reactions at loew pressures II. *J. Am. Chem. Soc.* **1928,** *50*, 617.

38.   Borkar, S. N. Very Accurate Gas-Phase Thermochemistry Through Photoelectron Photoion Coincidence (PEPICO) Spectroscopy. *Chemistry, University of the Pacific, Stockton, California* **2013**.

39.   Borkar, S. Sztaray, B.; Bodi, A. Dissociating C3H5Br+ ions: Almost all roads lead to the allyl cation. *Int. J. Mass. Spec.* **2012,** *330-332*, 100-108.

Chapter 4: Low- Temperature Synchrotron Photoionization Study of 2-Methyl-3-Buten-2-Ol (MBO) Oxidation Initiated by O(^{3}P) Atoms in the 298-650 K Range‡

Yasmin Fathi, Chelsea Price, and Giovanni Meloni*

Department of Chemistry, University of San Francisco, San Francisco, CA 94117 USA

4.1 Abstract

This work studies the oxidation of 2-methyl-3-buten-2-ol initiated by O(^{3}P) atoms. The oxidation was investigated at room temperature, 550, and 650 K. Using the synchrotron radiation from the Advanced Light Source (ALS) of the Lawrence Berkley National Laboratory, reaction intermediates and products were studied by multiplexed photoionization mass spectrometry. Mass-to-charge ratios, kinetic time traces, photoionization spectra, and adiabatic ionization energies for each primary reaction species were obtained and used to characterize their identity. Using electronic structure calculations, potential energy surface scans of the different species produced throughout the oxidation were examined and presented in this paper to further validate the primary chemistry occurring. Branching fractions of primary products at all three temperatures were also provided. At room temperature only three primary products formed: ethenol (26.6%), acetaldehyde (4.2%), and acetone (53.4%). At 550 and 650 K the same primary products were observed in addition to propene (5.1%, 11.2%), ethenol (18.1%, 2.8%), acetaldehyde (8.9%, 5.7%), cyclobutene (1.6%, 10.8%), 1-butene (2.0%, 10.9%), trans-2-butene (3.2%, 23.1%), acetone (50.4%, 16.8%), 3-penten-2-one (1.0%, 11.5%), and 3-methyl-2-butenal (0.9%, 2.5%), where the first branching fraction value in parentheses corresponds to the 550 K data. At the highest temperature, a small amount of propyne (0.8%) was also observed.

*Corresponding author: gmeloni@usfca.edu

4.2 Introduction

Air pollution continues to be a leading threat to the environment. According to the Environmental Protection Agency (EPA), there are six common air pollutants; lead, ozone, particulate matter (PM), nitrogen oxides (NO_2 and NO), sulfur dioxide (SO_2), and carbon monoxide (CO).[1] The burning of fossil fuels causes a dangerous amount of greenhouse gases to be released in the atmosphere. The release of these gases are detriment to the environment causing the earth's climate to change.[2] Fossil fuels have been used as the main source of energy throughout the past century. Petroleum-based gasoline emits constant air pollutants into the atmosphere that react with other compounds generating molecules harmful to human health and the environment. Fossil fuels are an expensive consumer product and have depleting resources.[3] For this reason, researchers have been looking to find alternative sources for renewable energy and power transportation in a more affordable and earth friendly way.[3] It has been found that the use of biofuels as an alternative fuel source produces less greenhouse gas emissions compared to fossil fuels[4], specifically mixing ethanol with gasoline has been found to decrease carbon monoxide emissions[5] and they are made from biomass that has been found as the only viable substitute.[6]

Popular renewable energy sources, biofuels, are slowly providing a long-term solution to reducing harmful combustion emission of greenhouse gases. Most biofuels are oxygenated carbon-neutral hydrocarbons, made from a mix of different feedstock, such as vegetable oil, fats, and different greases.[7] Oxygenated fuel increases the oxygen content in fuel while simultaneously reducing toxic emission.[7] While biofuels express several benefits as a renewable energy source, yet in combustion can increase emission of greenhouse gases such as nitrogen oxides and carbon oxides.[8] However, every biofuel reacts differently in the atmosphere and can create different byproducts that do not increase nitrogen oxide emissions. Short chain volatile alcohols are useful biofuels, which possess low water solubility and with linear hydrocarbon backbones, help confer combustion properties useful in internal combustion engines.[9] Nevertheless, the combustion of short chain volatile alcohols, used as biofuels, have become of great interest to observe what byproducts are formed in the atmosphere.[9] In general, knowledge of their combustion is scarce.

2-methyl-3-buten-2-ol (MBO) has become an attractive biofuel and renewable fuel additive due to its high energy content and low solubility in water.[10] MBO is produced from the methyl-erythritol-4-phosphate isoprenoid pathway.[10] Up to this point, ethanol has been the popular short chain volatile alcohol used as a biofuel. MBO has a greater energy output, due to its higher energy density of 106,000 BTU gallon^{-1} (British Thermal Unit), much closer to petroleum gasoline 125,000 BTU gallon^{-1}. Bioethanol on the other hand has a much lower energy content of 85,000 BTU gallon^{-}

1.[10] Additionally, the low solubility in water helps purify the compound compared to ethanol allowing purified MBO to be captured of a culture without needed post harvesting.[10]

In this investigation, the $O(^3P)$ initiated oxidation reaction of MBO is studied to investigate potential byproducts that can be formed in combustion. Ground state oxygen atoms are spread throughout the atmosphere through combustion from engines.[11] For this reason, researchers have found interest in how specific biofuels will react with $O(^3P)$. Cvetanovic began researching the different pathways that occur initially in these type of reactions. He concluded that two main pathways might occur: an addition pathway to the less-substituted carbon atom of a multiple bond and a H-atom abstraction where the $O(^3P)$ acts electrophilic.[12-13] Two different studies have been done to further this finding, using multiplexed synchrotron photoionization mass spectrometry (MPIMS)[14-15] and crossed molecular breams (CMBs),[16] researchers concluded that at the beginning stages of the oxidation with $O(^3P)$ these reactions undergo intersystem crossing (ISC) taking the initial triplet reactant to singlet radical or intermediate leading to product formation. The MPIMS study of $O(^3P)$ with propene[14-15] produced 40% of product formation from ISC, and the CBM study[16] had almost 90% product formation from ISC.

The research presented here is carried out at room temperature, 550, and 650 K using a tunable synchrotron multiplexed photoionization mass spectrometer, which has the ability to identify isomeric species via photoionization spectra. In addition, using electronic structure calculations potential energy surface scans of the different species produced throughout the oxidation are examined and presented.

4.3 Experimental

The synchrotron multiplexed time- and energy-resolved photoionization mass spectrometer at the Advanced Light Source (ALS) of Lawrence Berkley National Lab has been previously described and, therefore, a brief explanation will be presented in this work.[17-19]

MBO (purity $\geq$ 98%) is commercially obtained from Sigma Aldrich in liquid form, purified (freeze-pump-thaw technique), and along with helium gas is dispensed into a gas cylinder until the mixture has reached an overall partial pressure of 1%.[19] Using calibrated mass flow controllers, the purified gas mixture flows through a 650 μm pinhole into a heated slow flow quartz reactor tube.[19] The mixture flows directly into an ionization region, where it is photoionized through crossing tunable synchrotron radiation.[19] The ground state oxygen atoms are generated through 351 nm photolysis of 1% NO_2 and helium gas ($NO_2 \rightarrow O(^3P) + NO$).[17] According to Troe[20], at this wavelength the quantum yield of $O(^3P)$ is 1.00 and the absorption cross-section, according to Vandaele and co-

workers[21] is 4.62 x 10^{-19} cm^2. Based on these values together with the concentration of NO_2 of 1.3 x 10^{14} molecules cm^{-3} at 298 K, 3.7 x 10^{14} molecules cm^{-3} at 550 K, and 3.1 x 10^{14} molecules cm^{-3} at 650 K, and the laser fluence of 201 mJ cm^{-2}, the concentration of $O(^3P)$ is held at 2.1 x 10^{13} molecules cm^{-3} at 298 K, 6.0 x 10^{13} molecules cm^{-3} at 550 K, and 5.1 x 10^{13} molecules cm^{-3} at 650 K.

Based on the respective ionization energies, cations are formed and consequently accelerated and detected via a 50 kHz pulse orthogonal acceleration time-of-flight mass spectrometer.[22-23] The mass resolution under the current experimental conditions is approximately 1,600.[17] In this work the temperature of the reaction analyzed is varied and data is collected at 298, 550, and 650 K. Additionally, the pressures of these experiments are controlled using a feedback controlled throttle valve, starting at 4 Torr at 298 K and increasing to 7 Torr at both 550 and 650 K.

These experiments results in a three dimensional data plot that is integrated and sliced into two dimensional data plots; photon energy (eV) vs. mass-to-charge ration (amu) and time (ms) vs. mass-to-charge ratio (amu).[24] Photoionization (PI) spectra are used to identify reaction intermediates and products formed throughout the oxidation. These spectra are obtained through the integration of the ion signal of a specific reaction time range yielding the plot of ion intensity as a function of photon energy. In this work, the photoionization spectra are integrated in the time range of 0-70 ms at 298 K, 0-30 ms at 550 K, and 0-10 ms at 650 K. The time intervals are chosen to minimize the presence of signal due to possible secondary reactions that might occur. Species identification is achieved by comparing the photoionization spectrum of detected products with either literature, calculated, or measured PI plots of species the products are believed to be. The AIE's are determined by taking the linear extrapolation of the initial onset of the photoionization spectrum. The experimental adiabatic ionization energies have an estimated uncertainty of 0.05 eV for species identified with an onset. This uncertainty is due to the photon energy step size, possible presence of hot bands, and energy resolution.[19]

The ion intensity over the whole photon energy range is integrated yielding a plot of ion intensity versus time. The time trace plots reveal the amount of reactant depleted or product formed over a certain time range of the oxidation. The primary products of this experiment are also identified via the comparison of their time traces with the depletion of the reactant. Secondary chemistry is observed when the product formation is slower than the reactant depletion.

Once the reference photoionization spectra identify primary products at each observed signal, it is important to find the relative concentrations of each. Equation (1) shows the relation of the concentration (C) of a specific species at the photoionization spectrum intensity at a chosen energy (S_E), in our experiments 11 eV. The instrumentation constant is k, σ represents the photoionization

60

cross-section, and δ is the mass-discrimination factor, which has been determined to be equal to the mass of the identified species to the power of 0.67.[25]

$$S(E) = k\sigma(E)\delta C \qquad (1)$$

This work presents primary products observed from the oxidation of MBO + O(^{3}P) with their corresponding branching fractions, which are the concentration of different products formed relative to the reactant. In order to perform this quantification, absolute photoionization cross sections, which are obtained through absolute photoionization spectra, are needed. The absolute photoionization spectrum of the reactant is acquired through comparing the known literature photoionization spectrum of propene at a known concentration with the experimental data.

$$\frac{C_P}{C_R} = \frac{S_P\sigma_R\delta_R}{S_R\sigma_P\delta_R} = \frac{S_P\sigma_R(m_R)^{0.67}}{S_R\sigma_P(m_P)^{0.67}} = \frac{S_P\sigma_R}{S_R\sigma_P} * MDF \qquad (2)$$

The branching fractions in equation (2) are derived measuring the ratio of the concentration of the product (C_P) divided by the concentration of the reactant (C_R) (measured as change in the initial reactant concentration) at a specified photon energy that is equal to the ratio of the product of the ion signal (product, S_P, and reactant, S_R), the photoionization cross-section (product, σ_P, and reactants, σ_R), and the mass discrimination factor (MDF).[25] MDF is the quotient of reactant and product mass to the power of 0.67,[25] which takes into account the mass-dependent response of the detector.

4.4 Computational

The identification of products continues through electronic structure calculations. In this study, all computational calculations are completed in the Gaussian 09 software suite using the CBS-QB3 composite model.[26-27] This choice is based on its high accurate energetics with a mean absolute deviation of 1 kcal/mol and relative low computational cost.[28] The AIE of the reaction species is obtained using the computed values of the corrected zero-point vibrational electronic energies of the ground state neutral and cationic species. These values are also used to calculate the enthalpy changes of proposed mechanism pathways leading to the products.

The main focus of this research is to identify the products formed in combustion during the oxidation of MBO with O(^{3}P). In most cases, reference photoionization spectra are available for comparison to the experimental data to verify which products are created. In the case, however, that a reference photoionization spectrum is unavailable, a photoelectron spectrum (PE) is simulated. The PE spectrum is generated using the Franck-Condon (FC) and Franck-Condon-Herzberg-Teller methods.[29-31] The FC overlap integrals are calculated using recursive formula developed by Ruhoff.[32] Once the photoelectron spectrum is computed, its integration will provide the simulated photoionization spectrum, which can be compared to the experimental photoionization curve at the

specific signal for further product identification.

Once the products are identified, it is essential to determine the reaction pathways leading to the identified species from the initial oxidation. The potential energy surface scan is carried out as a function of bond lengths and bond angles using the B3LYP/6-31G(d) level of theory.[33] The energies of stationary points, minima, and transition states are then re-calculated using the CBS-QB3 method. These values are used to determine the enthalpy changes throughout the proposed mechanisms using MBO + O(^{3}P) as the energy reference level. In order to further verify the forward and reverse steps of the different potential energy surface scans as well as the local minima and saddle points, intrinsic reaction coordinate (IRC) calculations are also performed.

4.5 Results

To aid clarity to the discussion of the numerous observed reaction species and their pathways, the experimental data are first presented at the three temperature, 298, 550, and 650 K. A concise presentation of our quantitative results in form of branching fractions is then provided, followed by the computational characterization of the reaction pathways to substantiate the experimental findings.

The oxidation with O(^{3}P) yields two types of reactions: (1) oxygen addition and (2) hydrogen abstraction pathway. The most energetically favorable pathway is the O(^{3}P) addition to either less-substituted carbon of the double bond. As seen in Scheme 1, triplet diradicals A and B are formed from the ground state oxygen atom adding to either unsaturated carbons. The enthalpy change (Δ_rH) for radical A is -106 kJ/mol and for radical B is -109 kJ/mol. Diradical B (O(^{3}P) addition to the secondary unsaturated carbon) is therefore a few kJ mol^{-1} more stable than A (O(^{3}P) addition to the primary unsaturated carbon). These diradicals can enter the singlet surface through intersystem crossing (ISC) to form an epoxide that leads to several products observed in this study. The calculated Δ_rH yielding the epoxide from the reactant is -370 kJ/mol. The epoxide cation is computed to be unbound using the CBS-QB3 model and, in fact, it has not been experimentally observed. The second type of reaction formed throughout this oxidation is the hydrogen abstraction from a methyl group bonded to the γ carbon (-5 kJ/mol). This radical is then attacked by O$_2$ forming a peroxide species (-254 kJ/mol). The last possible hydrogen abstraction for the ground state oxygen atom throughout this oxidation is from the alcohol group bonded to the γ carbon. However, it is an endothermic process with a calculated Δ_rH of 5 kJ/mol and, thus, it is not considered in the analysis of the formation of the different species.
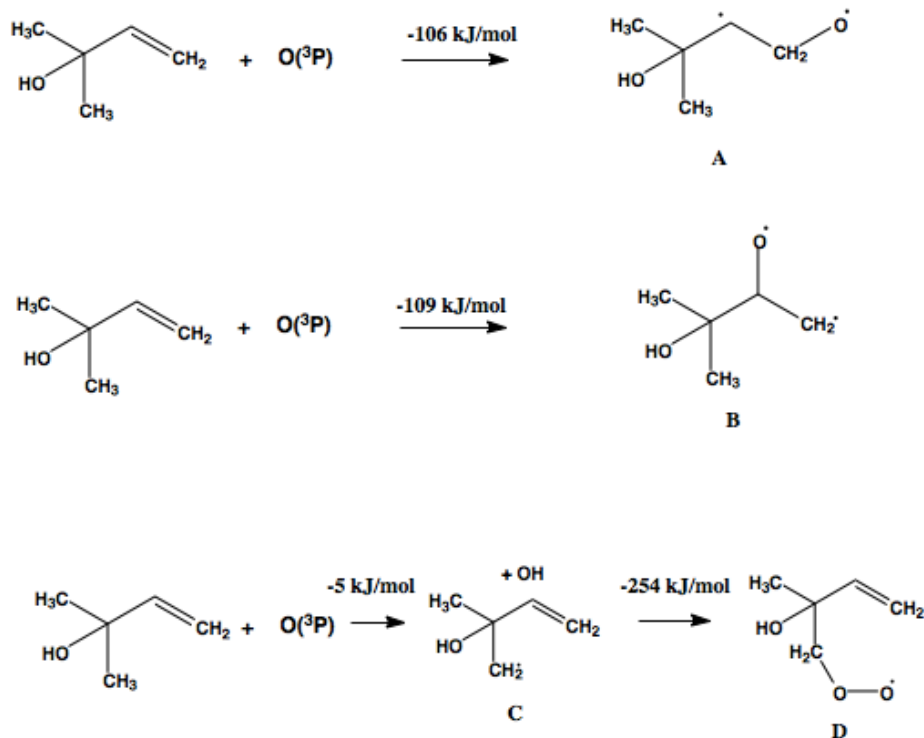
Scheme 1: The three radical species forming from the initial MBO + O(^{3}P) reaction (the CBS-QB3 calculated enthalpy changes are provided): the two oxy radicals A and B, the H abstraction radical C, and peroxy species D.

MBO+ O(^{3}P) reactions are carried out at three different temperatures. At 298 K the measurements are performed from 9.3 to 11 eV, and at 550 and 650 K in the 8.7–11 eV range.

4.5.1 Product Identification of MBO + O(^{3}P) at 298 K. At room temperature, the oxidation of MBO + O(^{3}P) forms only two signals at m/z 44, and m/z 58. The experimental photoionization spectrum at m/z 44 reveals two species. The experimental onset of the PI spectrum at 9.30 $\pm$ 0.05 eV agrees with the reference PI spectrum of ethenol up to around 10.20 eV, where the literature PI spectrum of acetaldehyde is matched. According to Ruscic and Berkowitz,[34] the m/z 44 experimental ionization onset matches very well with the reference adiabatic ionization energy of 9.33 $\pm$ 0.01 eV for ethenol. The experimental ionization of acetaldehyde also is in good agreement with the literature adiabatic ionization energy of 10.20 $\pm$ 0.02 eV.[35] The summation of the literature photoionization spectra of ethenol and acetaldehyde taken by Cool et al.[36] matches very well with the experimental m/z 44 photoionization curve (Figure 1).
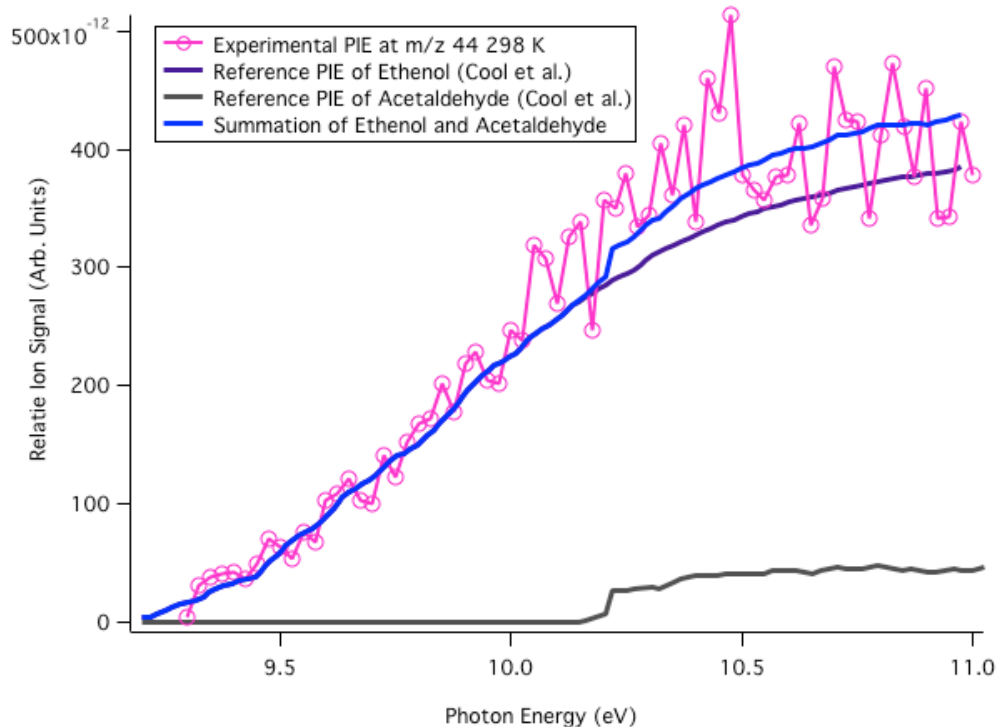
Figure 1. Summation (blue line) of the literature photoionization spectra of ethenol (dark purple) and acetaldehyde (gray) superimposed onto the experimental photoionization curve at m/z 44 (pink line and open circles) at 298 K.

Experimentally, the adiabatic ionization energy of acetone (m/z 58) is observed to be 9.70 ± 0.05 eV, compared to the literature adiabatic ionization energy of 9.694 ± 0.006 eV reported by Trott.[37] In the absolute photoionization spectrum of MBO, m/z 58 is a dissociative photoionization fragment. However, in the studied reaction m/z 58 is observed as a product, i.e., its time trace is not depleting. The ratio of the dissociative photoionization fragment (daughter ion) and the reactant (parent ion) in the absolute photoionization spectrum (2.65 at 11 eV) is used to adjust the experimental m/z 58 spectrum. This is achieved by adding the normalized signal (with respect to the parent signal in the reaction data) of the daughter ion to the observed curve to take into account the depleting signal of the fragment. The resulting m/z 58 matches well to the literature photoionization spectrum of acetone within the very low signal-to-noise ratio, which affects the uncertainty of the measured ion signal as described in the branching fractions section (Figure 2).[38] Acetone has been determined to be a primary product by comparing its kinetic trace to the temporal behavior of the

reactant. Its time trace is presented in Figure 3. The time trace of the reactant, which is indeed a depleting signal, has been multiplied by -1 for comparison with the formation of the product.
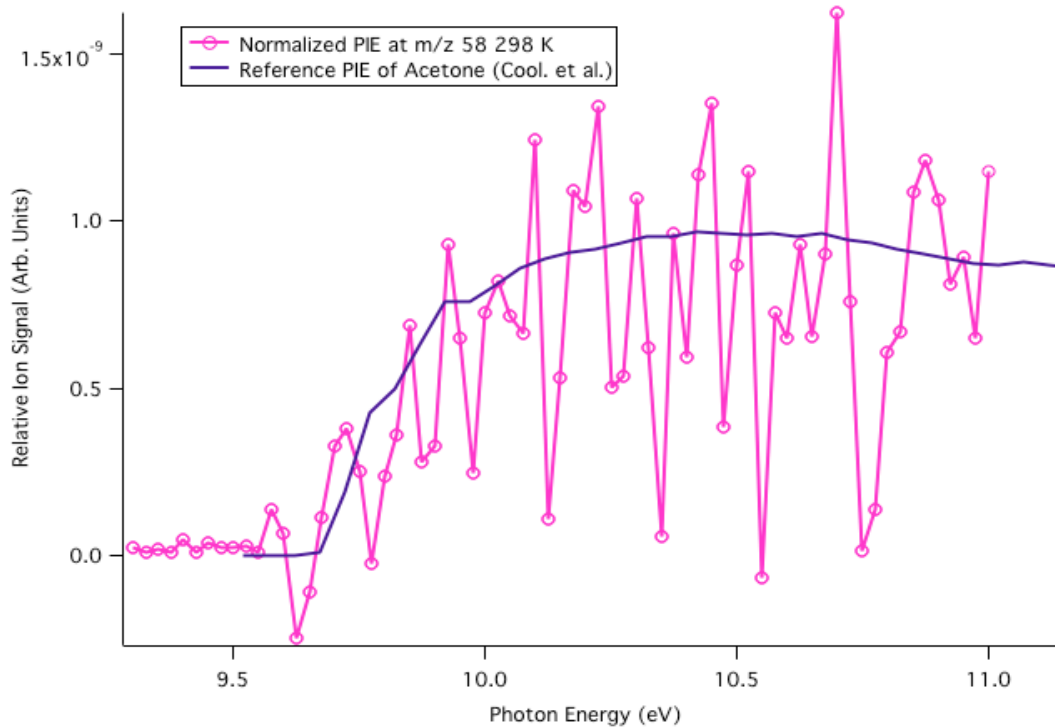
Figure 2. Comparison of the experimental photoionization curve of product m/z 58 superimposed onto the literature photoionization spectrum of acetone at 298 K.
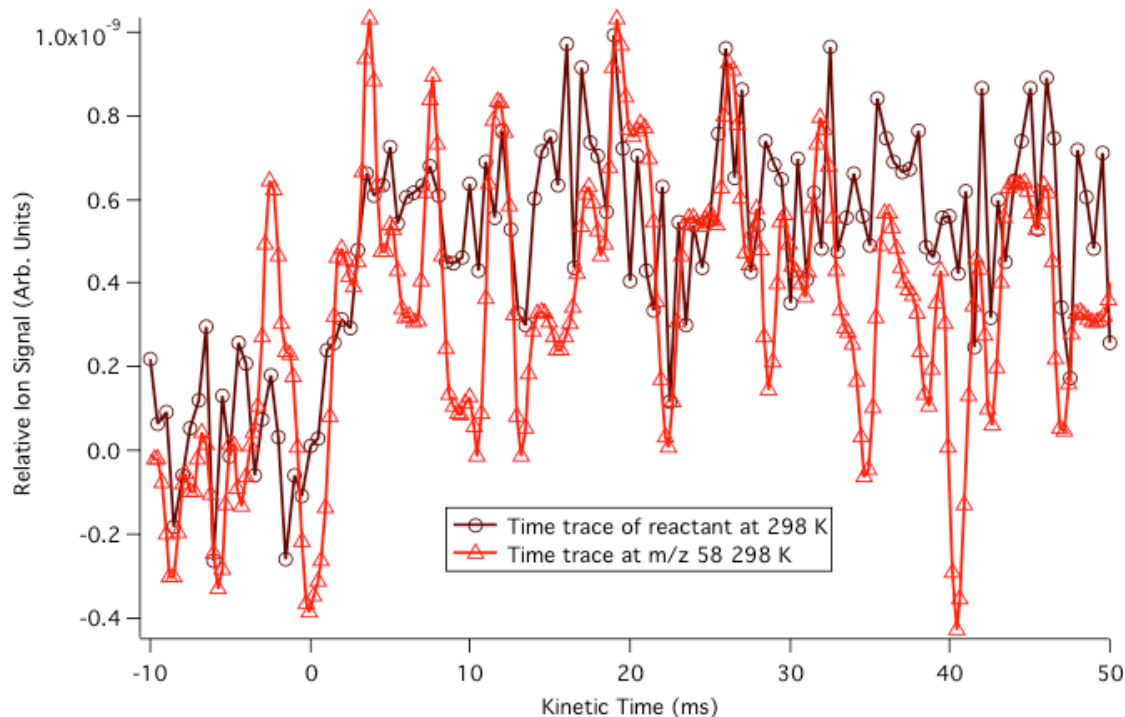
Figure 3. Time trace of m/z 58 (open triangles) superimposed onto the time trace of the reactant (open circle) at 298 K. The time trace of the reactant has been multiplied by -1.

4.5.2 Product Identification of MBO + O(^{3}P) at 550 and 650 K.

At the higher temperatures, the oxidation of MBO presents additional products. At both temperatures, the following signals are identified: m/z 42, 44, 54, 56, 58, 70, 82 and 84. At 650 K, an additional primary product is identified at m/z 40. When photolyzing NO_2 to create O(^{3}P), NO is formed as well. At signal m/z 30, the experimental photoionization spectrum matches very well to the reference photoionization spectrum of NO[39] (Figure 4). A signal at m/z 40 is only observed at 650 K and assigned as propyne (Figure 5) based on the good agreement with its superimposed literature photoionization spectrum.[38] The observed adiabatic photoionization energy is 10.40 $\pm$ 0.05 eV, which is in good agreement with the reported value of propyne of 10.37 $\pm$ 0.01 eV.[40]
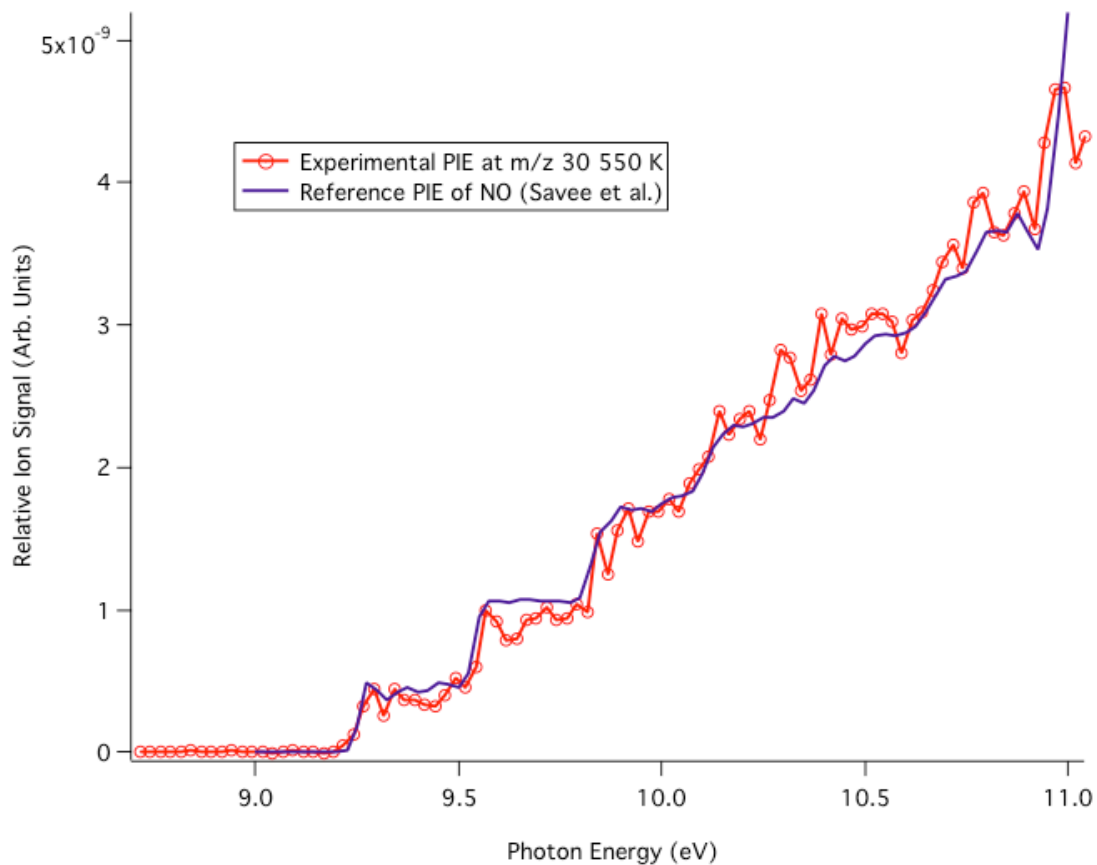
Figure 4. Literature photoionization spectra of NO (blue) superimposed onto the experimental photoionization curve at m/z 30 at 550 K (red line and open circles).
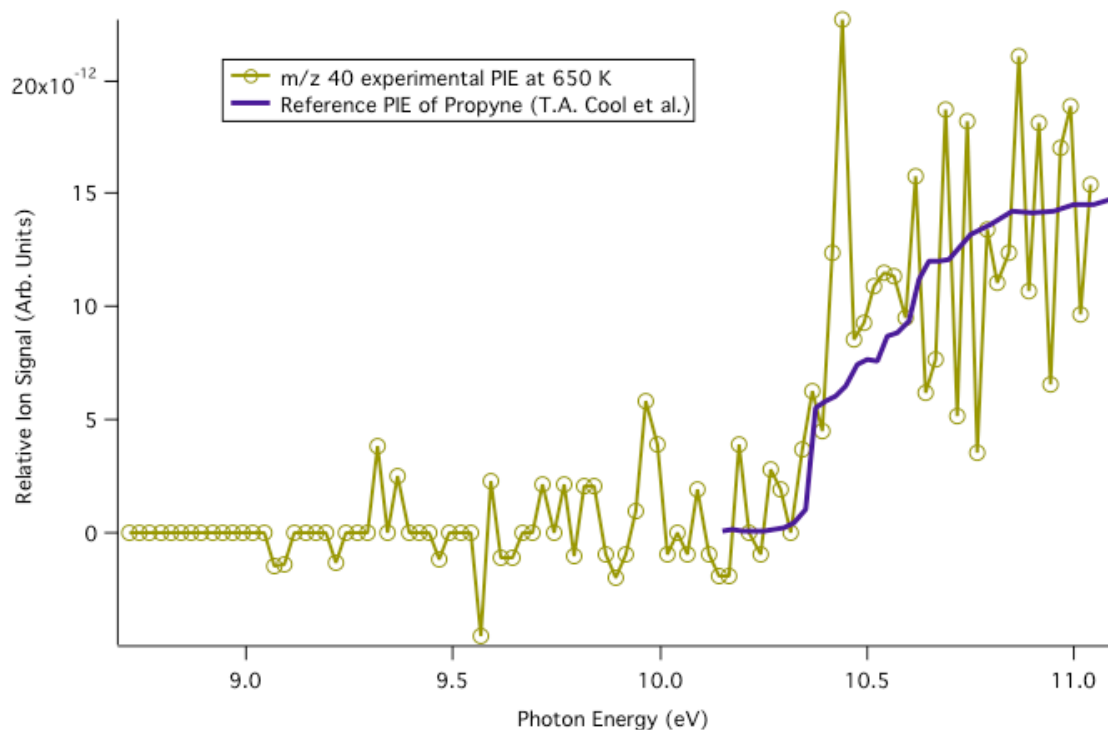
Figure 5. The experimental photoionization spectrum of m/z 44 (dark yellow line and open circles) and the reference photoionization spectrum of propyne (purple) for the MBO + O(^{3}P) reaction at 650 K.

Person and Nicole[41] reference PI spectrum of propene agrees well with the experimental data at m/z 42 (Figure 6). The ionization onset of 9.70 $\pm$ 0.05 eV matches the reference AIE of 9.74 $\pm$ 0.01[41] eV. Similarly to 298 K, products at m/z 44 are observed, however, the ethenol contribution gets smaller as the temperature is increased (Figure 7). Figure 8 presents the time trace of m/z 44 superimposed onto the time trace of the reactant at 550 K showing its fast formation as primary product. The time trace of the reactant (depleting signal) has been multiplied by -1 for comparison with the formation of the product (Figure 8).
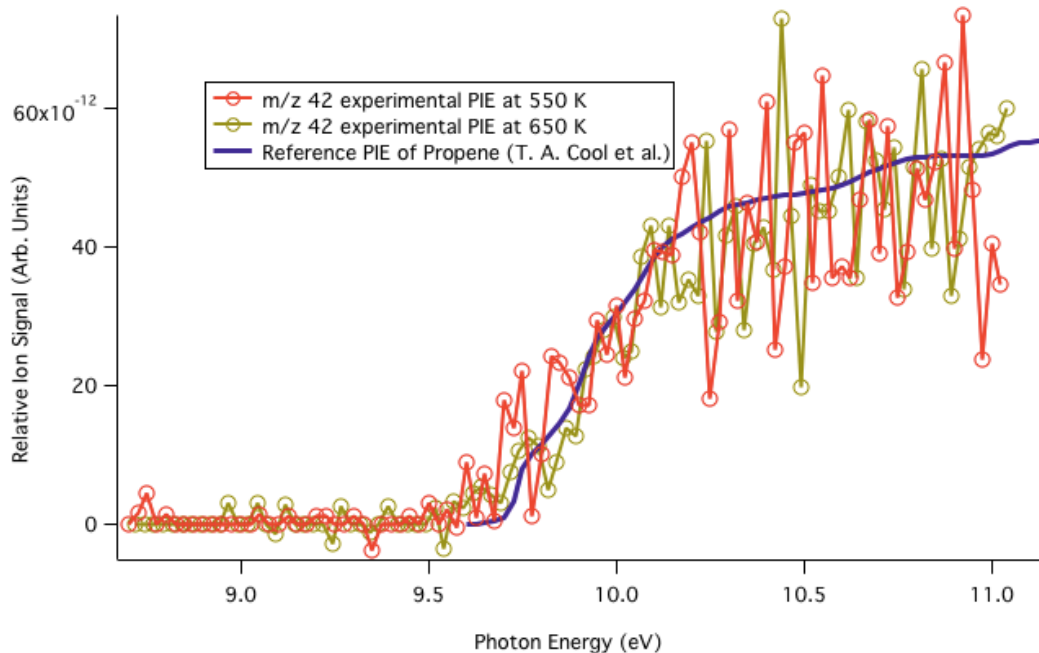
Figure 6. The literature photoionization spectra of propene (dark red) superimposed onto the experimental photoionization spectrum at m/z 42 (red line and open circles) at 550 and 650 K.

a)

b)
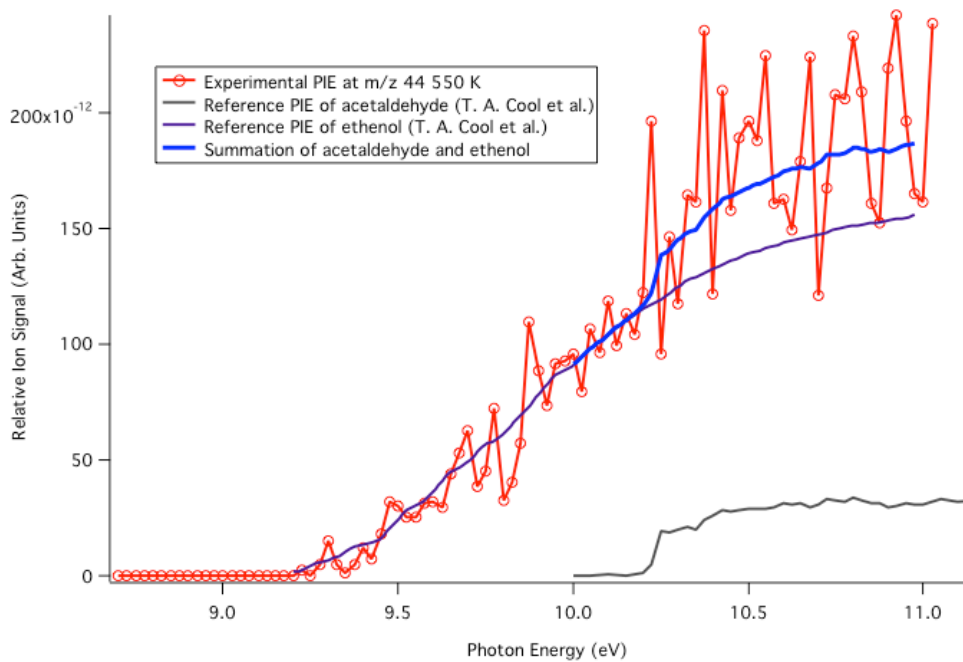
Figure 7. a) Summation (blue line) of the literature photoionization spectra of ethenol (purple) and acetaldehyde (gray) superimposed onto the experimental photoionization spectrum at m/z 44 (red line and open circles) at 550 K. b) The reference photoionization spectrum of acetaldehyde and ethenol superimposed onto the experimental photoionization spectrum of m/z 44 at 650 K (dark yellow line and open circles).
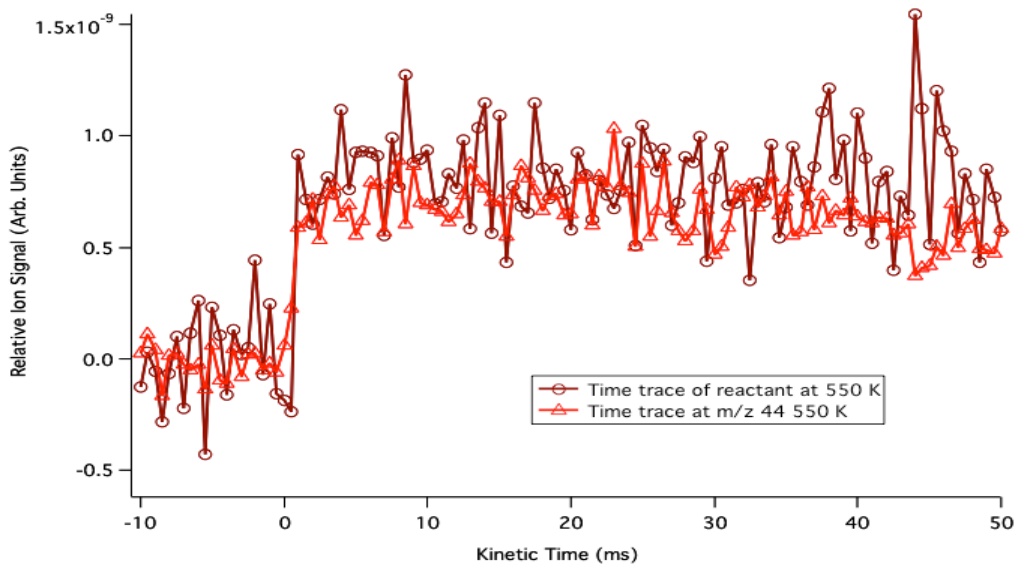
Figure 8. Time trace of m/z 44 (open triangles) superimposed onto the reactant time trace at 550 K. The time trace of the reactant has been multiplied by -1.

The m/z 54 signal is assigned to cyclobutene (Figure 9) with its experimental AIE of 9.40 $\pm$ 0.05 eV in good agreement with the literature value of 9.43 $\pm$ 0.02 eV.[42] There is no literature PI spectrum for cyclobutene, thus using the CBS-QB3 optimized geometries and force constants of the cationic and neutral species (Franck-Condon approximation), a photoelectron curve is simulated and integrated into a photoionization spectrum, which agrees with this study experimental data. Two isomeric species are formed at m/z 56 (Figure 10), trans-2-butene and 1-butene. The ionization onset of 9.10 $\pm$ 0.05 eV is fit to the literature PI curve of trans-2-butene with a reported AIE of 9.10 $\pm$ 0.02 eV.[43] The literature AIE of 1-butene of 9.62 $\pm$ 0.05 eV[44] and Wang et al.[45] PI spectrum agree well with the experimental data at the higher energy range. The summation of trans-2-butene and 1-butene spectra is a good match to the overall shape of the experimental signal at m/z 56 up to 10.1 eV. At higher photon energies the un-matched experimental signal might be due to dissociative photoionization of products at m/z 84, which could undergo a CO loss.
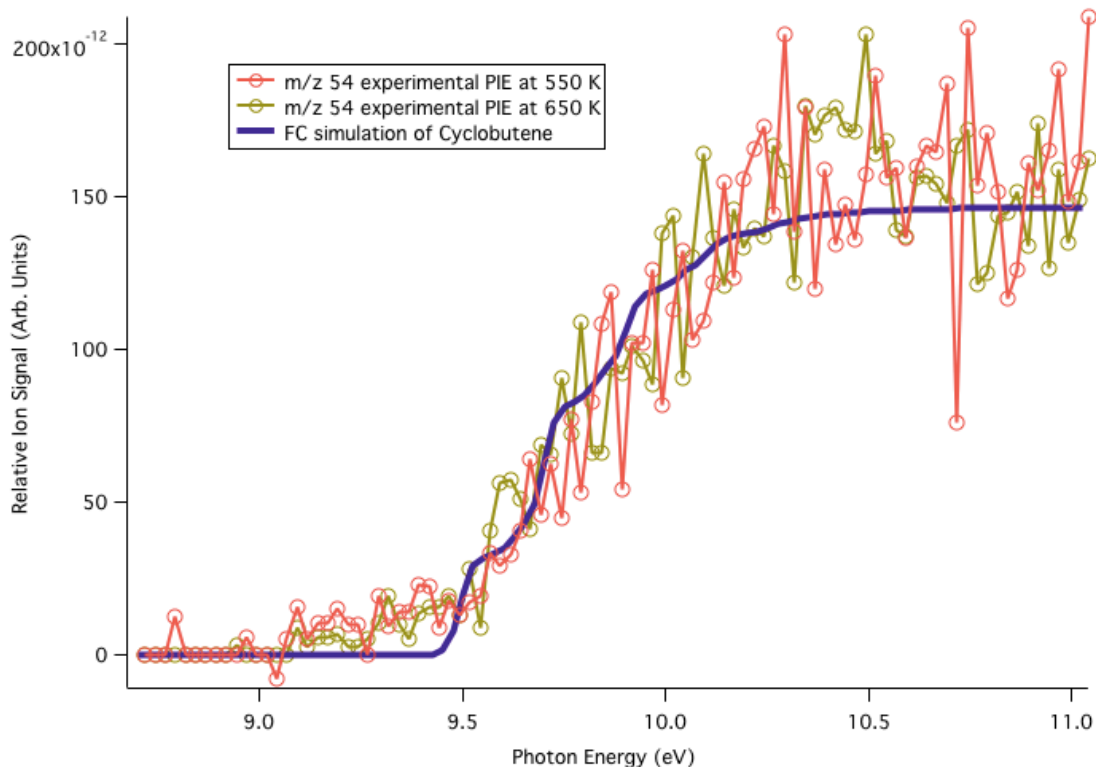
Figure 9. The experimental photoionization spectrum of m/z 54 at 550 K (red line and open circles) and 650 K (dark yellow line and open circles) and the simulated Franck-Codon (FC) photoionization spectrum of Cyclobutene (purple) for the MBO + O(^{3}P) reaction.
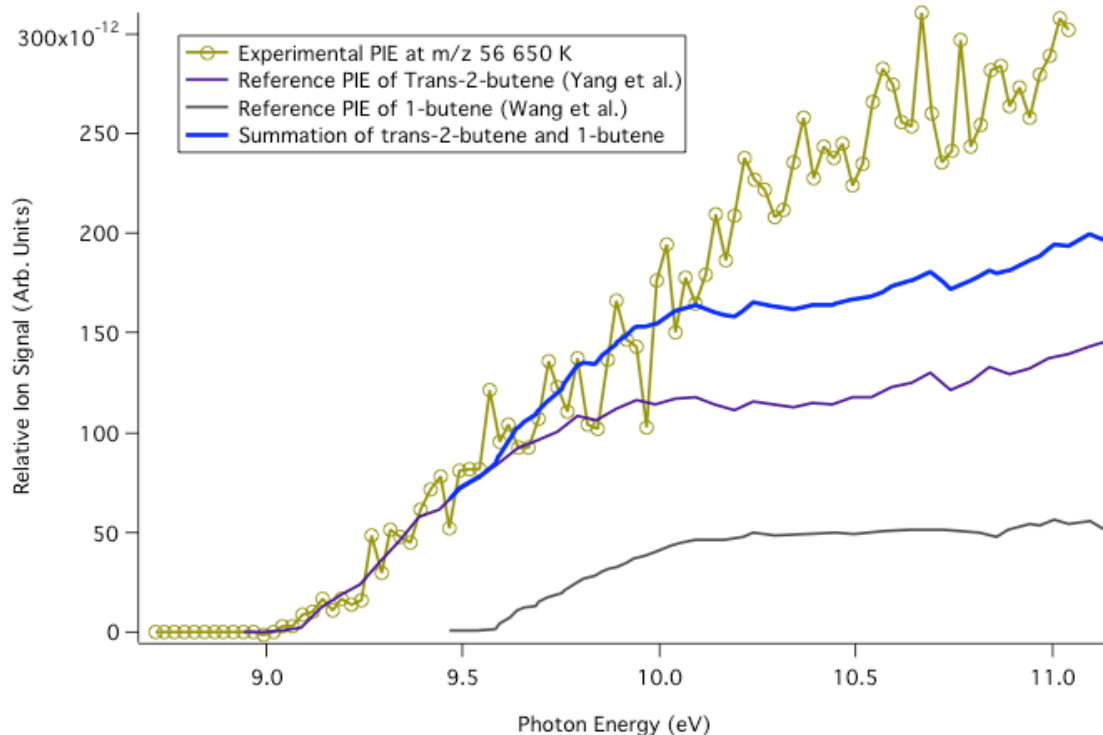
Figure 10. a) Summation (blue line) of the literature photoionization spectra of trans-2-butene (purple) and 1-butene (gray) superimposed onto the experimental photoionization spectrum of m/z 56 at 650 K (dark yellow line and open circles) for the MBO + O(^{3}P) reaction.

A product at m/z 58 is observed. The same procedure used at 298 K is applied at both 550 and 650 K to yield a signal consistent with the presence of acetone. m/z 70 is assigned to 2-butenal based on the good agreement of the observed ionization onset at 9.70 $\pm$ 0.05 eV with the literature AIE of 9.73 $\pm$ 0.01 eV[46] and the literature spectrum (Figure 11).[43] Based on the computational results presented below in the Proposed Mechanism of MBO with O(^{3}P) section, the formation of this species is not kinetically favorable due to a very high barrier for this formation. Therefore, this species cannot be considered to be a primary product. Figure 12 presents the time trace of m/z 70 superimposed onto the time trace of the reactant (multiplied by -1) at 550 K showing a slower formation than a primary product would have (see Figure 8 for comparison). The signal m/z 82 at both temperatures is assigned to cyclobutanecarbaldehyde based on the good match with the FC simulated spectrum (Figure 13). Finally, two non-isomeric species are characterized at m/z 84 (Figure 14). The ionization onset of the spectrum at 9.40 $\pm$ 0.05 eV is consistent with the measured spectrum of 3-penten-2-one with a reported AIE of 9.39 eV.[47] The spectrum of this species alone does not

match the whole signal in the studied photoionization energy range. The inclusion of 3-methyl-2-butenal with an AIE of 9.4 eV[43] in the summation spectrum is in good agreement with the measured signal.
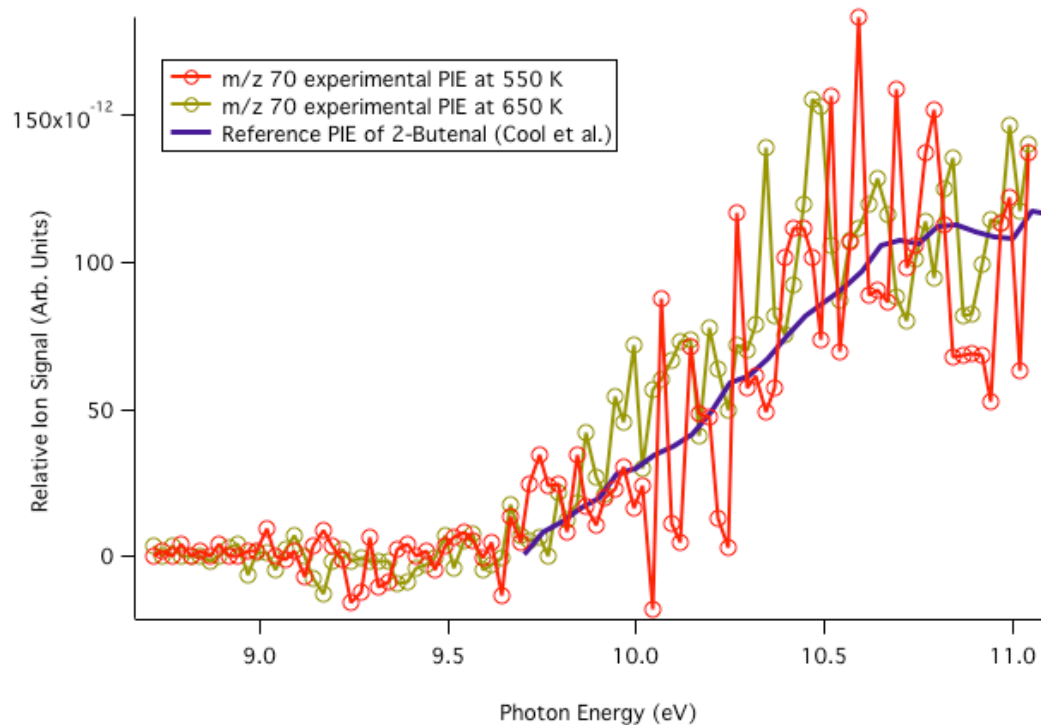
Figure 11. The experimental photoionization spectrum of m/z 70 at 550 K (red line and open circles) and 650 K (dark yellow line and open circles) and the reference photoionization spectrum of 2-Butenal (purple) for the MBO + O(^{3}P) reaction.
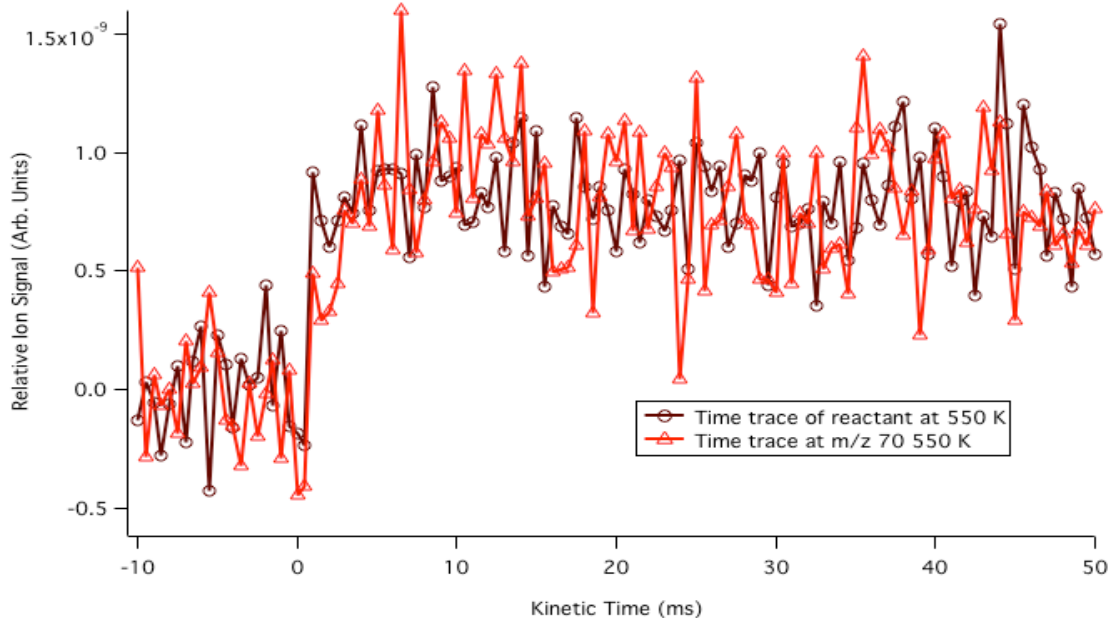
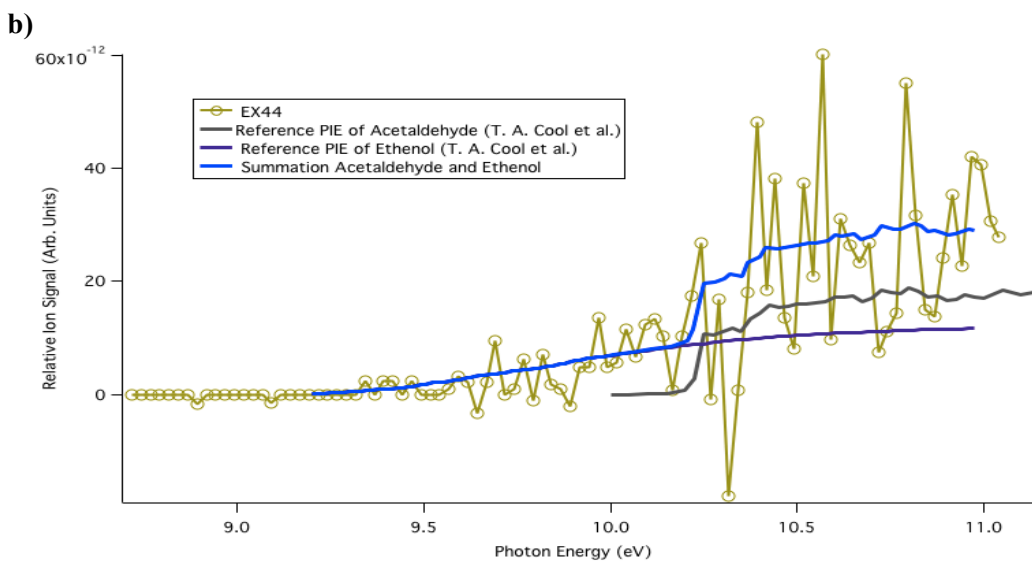**Figure 12.** The time trace of m/z 70 (open triangles) superimposed on the reactant time trace (open circles) at 550 K. The time trace of the reactant has been multiplied by -1.
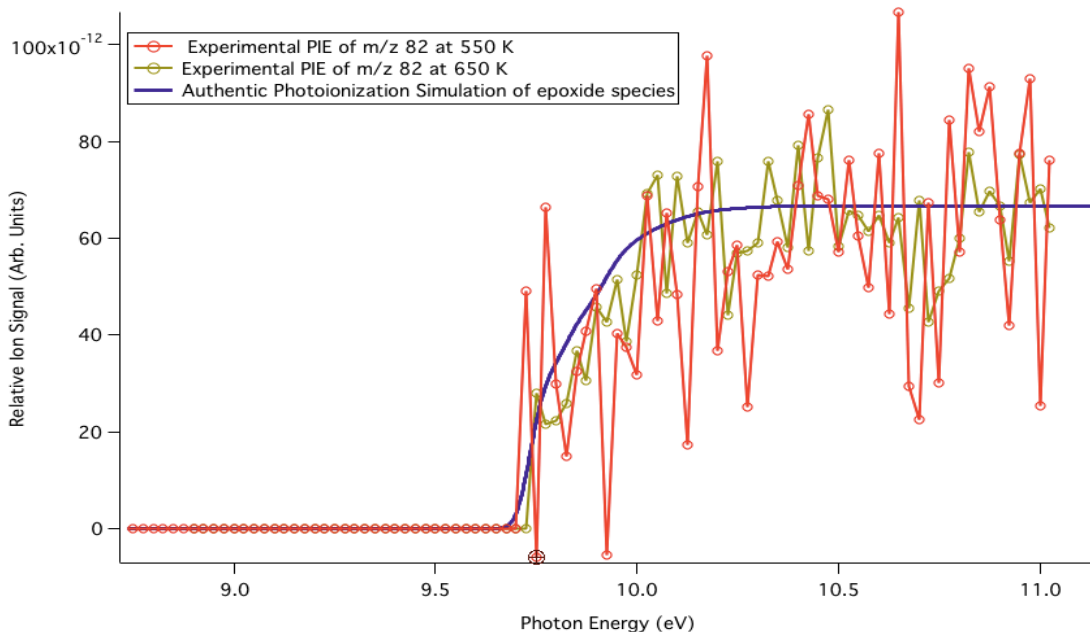
Figure 13. Comparison of the experimental photoionization spectrum at m/z 82 superimposed onto the Franck-Condon simulation of the epoxide species at 550 K (red line and open circles) and 650 K (dark yellow line and open circles).
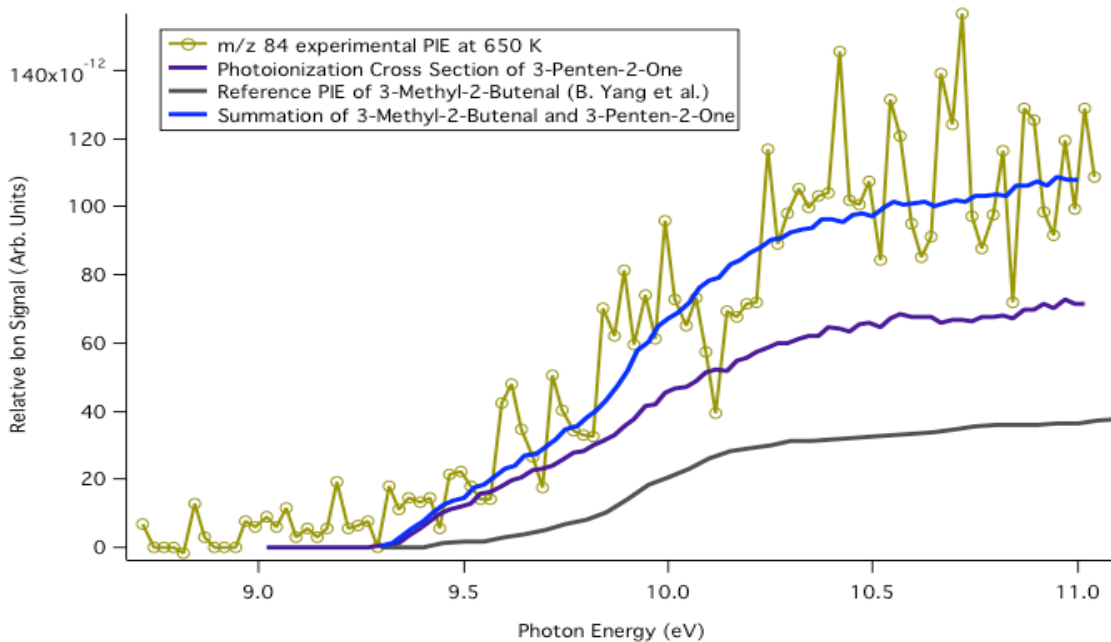
Figure 14. Summation at 650 K (blue line) of the simulation Franck-Codon (FC) photoionization spectrum of 3-penten-2-one (purple) and the literature photoionization spectrum of 3-methyl-2-butenal (gray) superimposed onto the experimental photoionization spectrum at m/z 84 at 650 K (dark yellow line and open circles) for the MBO + O(^{3}P) reaction.

4.5.3 Branching Fractions

The products formed at all three temperatures and their corresponding branching fractions, calculated using equation (2), are presented in Table 1. Both ion intensities and photoionization cross-sections are a function of photon energy. For this reason, PI spectra of each product formed are compared at the same photon energy of 11 eV to determine their concentrations. The uncertainties of the branching fractions are calculated using the propagation of errors of each variable in equation (2) and are listed in Table 1. The signal used to calculate the branching fractions at each temperature is average for 250 laser shots at each energy step. The uncertainties of the photoionization cross sections and the mass discrimination factor are from the literature, whereas the uncertainty of each ion signal is estimated by taking the difference between the measured upper value at 11 eV of a specific species and its reference (literature or simulation) spectrum used in the assignment. The same procedure is applied using the lower ion signal value at 11 eV.

Table 1. Branching fractions of products with their uncertainties formed during the oxidation of MBO using O(^{3}P) at 298, 550, and 650 K.

Compound	m/z	298 K	550 K	650 K
From the O(^{3}P) addition pathway				
Propyne	40			1.0 ± 0.5
Ethenol	44	26.6 ± 8.9	18.1 ± 10.0	2.8 ± 1.7
Acetaldehyde	44	4.2 ± 1.5	8.9 ± 5.1	5.7 ± 3.4
Cis-2-Butene	56		3.2 ± 1.7	23.1 ± 10.5
1-Butene	56		2.0 ± 1.1	10.9 ± 5.0
Acetone	58	53.4 ± 39.8	50.4 ± 38.3	$16.8 + 8.7$
3-Penten-2-One	84		1.0 ± 0.5	11.5 ± 5.1
3-Methyl-2-Butenal	84		0.9 ± 0.5	2.5 ± 1.1
From the O(^{3}P) H abstraction pathway				
Propene	42		5.1 ± 2.8	11.2 ± 4.5
Cyclobutene	54		1.6 ± 0.8	10.8 ± 4.7
Cyclobutanecarbaldehyde	82		0.4 ± 0.3	2.4 ± 1.2

At 298 K only three products are observed, ethenol, acetaldehyde, and acetone. They are quantified and the total branching fraction is 84.2 ± 40.8 %. The large estimated error of the branching fraction of acetone (± 39.8%) is due to the very low signal-to-noise ratio at m/z 58. At 550 and 650 K more products are observed and the overall branching fractions are 91.6 ± 40.1 % and 98.7 ± 16.7 %, respectively. Acetone with a branching fraction of 50.4 ± 38.3 % is the major product at 550 K, whereas at 650 K trans-2-butene becomes the most abundant product with a branching fraction of 23.1 ± 10.5 %. The relative amount of formaldehyde and ethanol diminishes, as the temperature is increased.

4.5.4 Proposed Mechanism of MBO with O(^{3}P). As discussed above, the most favorable energetic pathway of the oxidation of MBO + O(^{3}P) is the formation of the singlet epoxide from the triplet diradicals formed through the oxygen addition to the carbons of the double bond.

The initial reaction of MBO with O(^{3}P) forming triplet diradicals is used as the reference point for the energetic calculations of the products. Due to the numerous species computed in this oxidation, the products formed from the epoxide are separated into two different potential energy surface diagrams (a) and (b) (Fig. 15). The epoxide is not seen throughout this reaction. Computationally its cation is unbound, conveying that the epoxide dissociatively ionizes. Any molecular species or energetic barrier above the red line in the potential energy surface diagrams is

thermodynamically unfavorable. In Figure 15 (a) the direction to right follows the formation of acetaldehyde and propyne and to the left it follows the formation of cis-2-butene and 1-butene. Following the right side of the (a) energetic pathway, the hydrogen transfer from a methyl group bonded to the γ carbon cleaves γ and β C-C bond and forms acetaldehyde and prop-1-en-2-ol, with a calculated enthalpy change of 18 kJ/mol (E1*). The barrier of this hydrogen transfer is of 289 (TS1*). The formation of propyne has a calculated transition state barrier of 331 kJ/mol (TS2*).

The potential energy surface diagram pathway to the left forms two products identified at signal m/z 56. With a calculated barrier of 268 kJ/mol (TS1) and an enthalpy change of 50 kJ/mol (E1), the epoxide (E) rearranges through a hydrogen transfer to the alcohol group yielding an epoxide + H_2O. The epoxide breaks with a barrier of 326 kJ/mol (TS2). A hydrogen transfer to the methylene group initiates the breaking of the epoxide group forming 2-ethacrolein, which is not observed due to poor Franck-Condon factors. E2 converts into E3 with a barrier of 279 kJ/mol (TS3). This species has a calculated adiabatic ionization energy of 8.32 eV. The optimized cation has a slightly different structure than the neutral species, further indicating that the species is not observed due to poor FC factors. From this point, carbon monoxide cleaves off creating a double radical on the β carbon with a calculated heat of reaction of 278 kJ/mol (E4) and no barrier. E4 can undergo two different pathways. If hydrogen is transferred from the CH_2 moiety to the adjacent C, a double bond is formed with a barrier of 14 kJ/mol (TS4a) yielding trans-2-butene and an enthalpy change of -278 kJ/mol. If instead hydrogen is transferred from the CH_3 to the double radical C site, 1-butene is formed with a calculated barrier of 32 kJ/mol (TS4b) and enthalpy change of -279 kJ/mol (Figure 15 (a)).

In the second potential energy surface diagram (Figure 15 (b)), further products are energetically proven through the singlet epoxide (F). Similarly, to the previous potential energy surface diagram, the initial oxidation of MBO with $O(^3P)$ is used as the reference point. The hydrogen transfer from the β carbon to the epoxidic oxygen yields a double radical site on the β carbon with a calculated enthalpy change of 238 kJ/mol (F1) and barrier of 285 kJ/mol (TS1). With a computed barrier of 58 kJ/mol (TS2*), water is pulled off forming 3-methyl-2-butenal with an overall exothermicity of 298 kJ/mol. The hydrogen atom of the OH group from F1 can be transferred to the double radical to form F2 with a barrier of 30 kJ/mol (TS2) and enthalpy change of 243 kJ/mol. The βC-γC bond is cleaved yielding acetone and ethenol with a calculated enthalpy change of 25 kJ/mol and barrier of 239 kJ/mol (TS3*). Indeed, F2 has another fate; it can lead to the formation of 3-penten-2-one with an overall exothermicity of 276 kJ/mol.
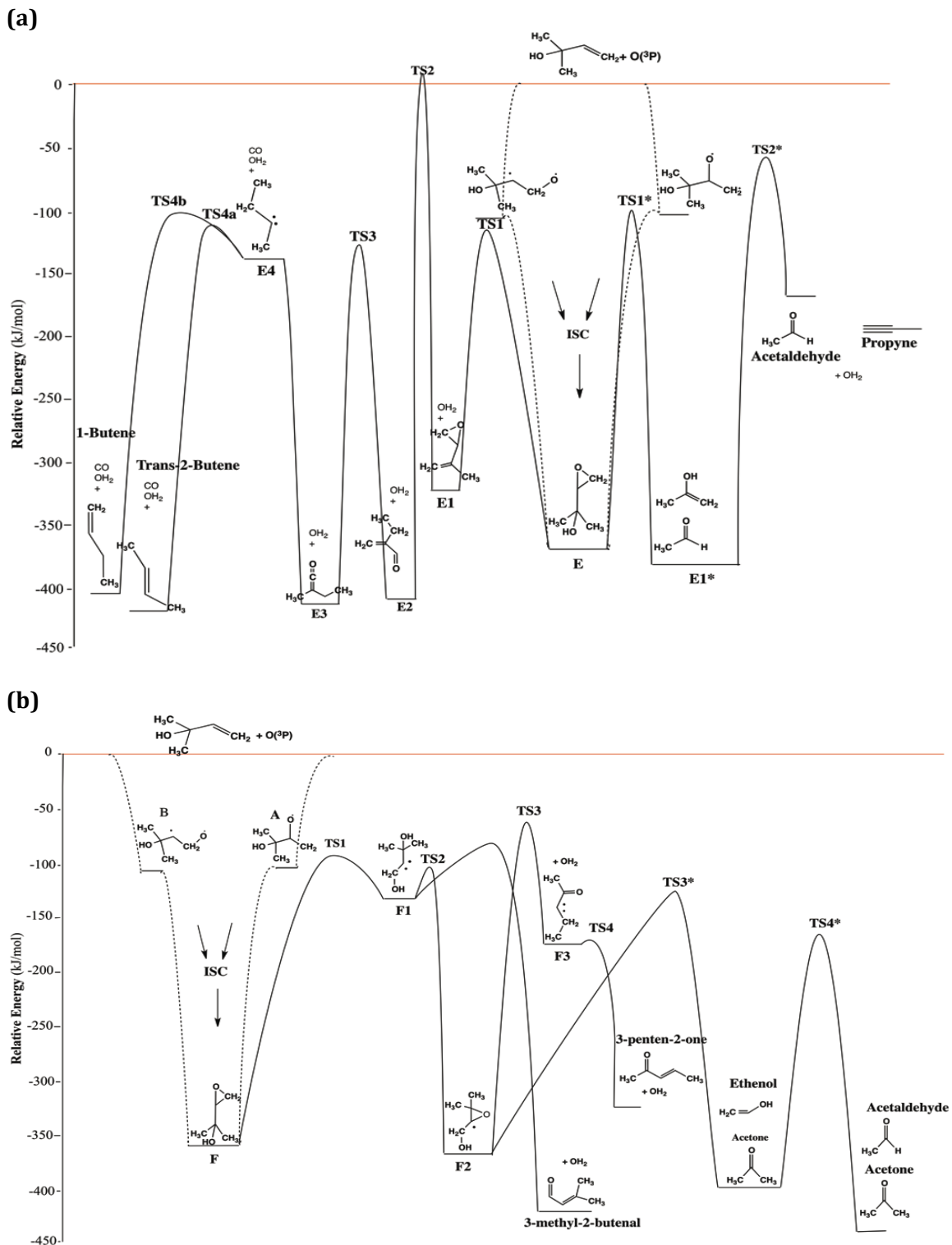
Figure 15. (a) Potential energy surface diagram of the proposed mechanisms of the oxidation of MBO + O(^{3}P). Each energy level throughout this diagram was calculated using the CBS-QB3 method and are all relative to the epoxide (E) at-370 kJ/mol. (b) Potential energy surface diagram continued of the proposed mechanisms of the oxidation of MBO + O(^{3}P) with the epoxide (F) reference point at -370 kJ/mol forming the rest of the products seen in the reaction.

78

Since experimentally O_2 is present in the 1% NO_2 gas mixtures used to produce $O(^3P)$, O_2 is considered for the mechanism of the formation of cyclobutene, formaldehyde, and propene. For this diagram shown in Figure 16, the radical plus the O_2 is used as the reference point. Any transition state barrier above the red line is kinetically unfavorable throughout these pathways. The formation of the peroxy radical (D), O_2 addition has a heat of reaction of -254 kJ/mol as seen previously. For the formation pathways of the three observed products, the initial step from D is the formation of D1 with an enthalpy change of -15 kJ/mol (D1). This species is not observed because it dissociatively ionizes according to our CBS-QB3 calculations. Cyclobutene is yielded through a high barrier (TS2*) 30 kJ/mol above the energy reference level. Cyclobutene is not observed at room temperature but it is formed at 550 and 650 K. The intermediate cyclobutanecarboaldehyde (D3*) is also observed at the higher temperatures.

The formation of propene continues from species D1 through the highest TS3 barrier, which is below the energy reference level. The intermediate D2 and D4 species in the pathway for propene formation are not observed because D2 dissociatively ionizes and D4 has poor FC factors. Formaldehyde is formed with D4 and is observed at 550 and 650 K. 2-Butenal, which is observed experimentally, cannot be yielded via the presented computed potential energy surface because it needs to overcome two very high barrier 217 (TS4) and 163 (TS5) kJ/mol higher than the energy reference level.
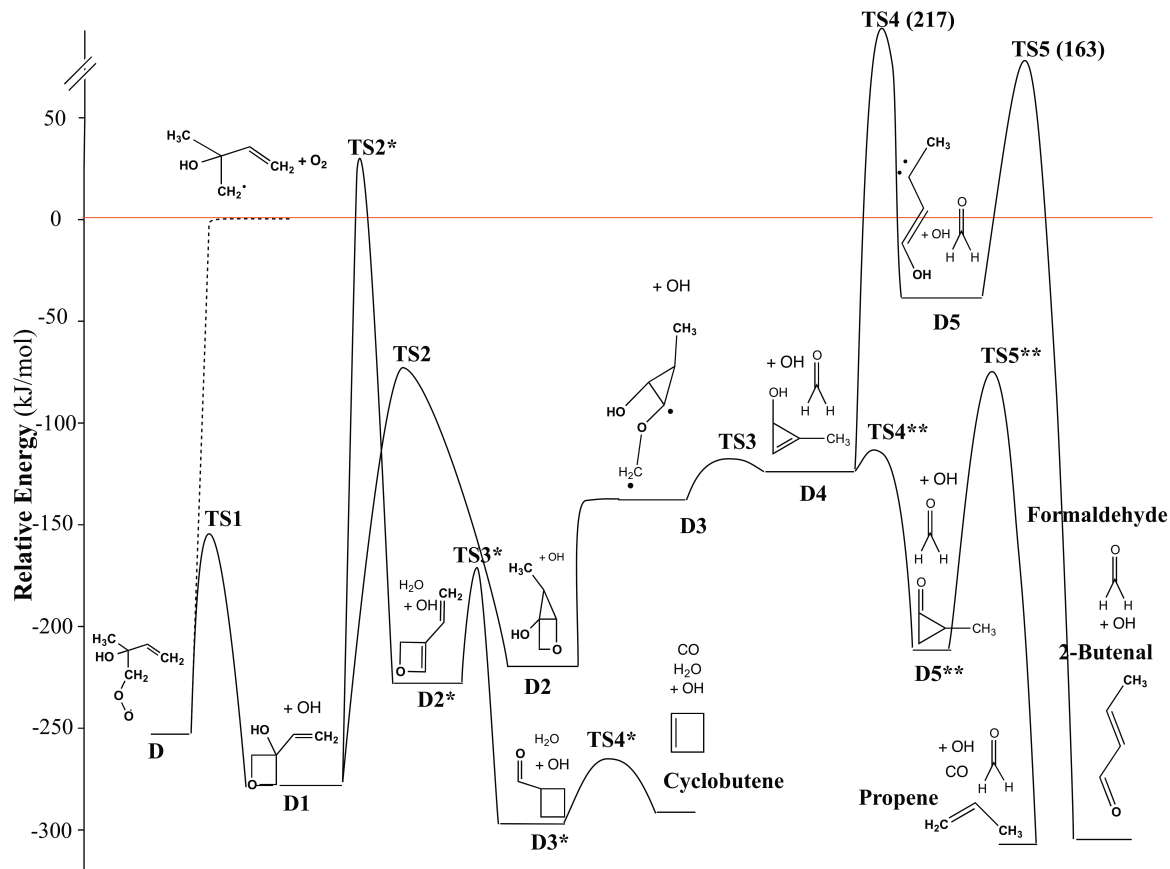
Figure 16. Potential energy surface diagram of the hydrogen abstraction radical reacting with O_2 addition onto radical C for the oxidation of MBO + O(^{3}P) for the formation of propene, cyclobutene, and 2-butenal. The energies throughout these mechanisms were calculated using the CBS-QB3 method and are expressed through radical D.

4.6 Conclusions

The biofuel additive, MBO is oxidized using O(^{3}P) atoms at 298, 550, and 650 K. This study presents the thorough investigation of the low-pressure elementary reactions of this oxidation at different temperatures. The primary products in this study are identified and presented. The experiments are carried out using the synchrotron radiation as the ionization source of the Advanced Light Source (ALS) of the Lawrence Berkley National Laboratory. At room temperature only three species are identified, ethenol, acetaldehyde, and acetone with a total branching fraction of 84.2 $\pm$ 40.8 %. At 550 and 650 K more products are observed and the overall branching fractions are 91.6 $\pm$ 40.1 % and 98.7 $\pm$ 16.7 %, respectively. Acetone with a branching fraction of 50.4 $\pm$ 38.3 % is the major product at 550 K, whereas at 650 K trans-2-butene becomes the most abundant product with a branching fraction of 23.1 $\pm$ 10.5 %. The relative amount of ethenol and acetone diminishes as the

temperature is increased. The potential energy surface has been computed using the CBS-QB3 composite model to validate the formation of the observed species.
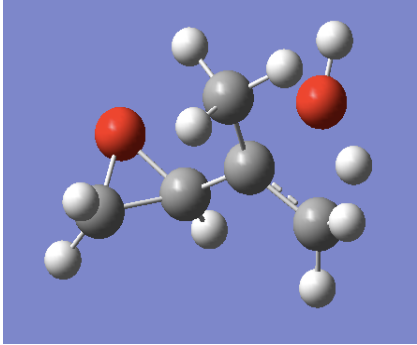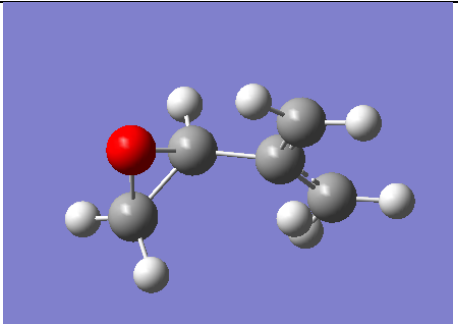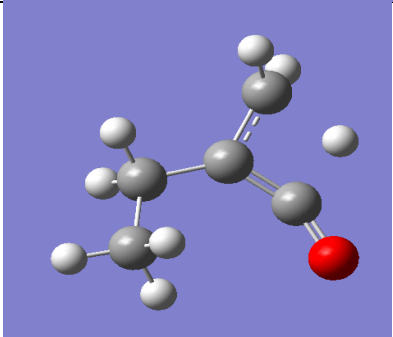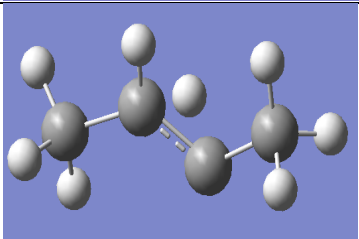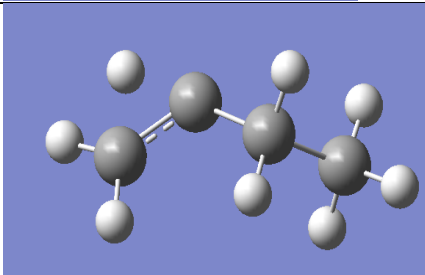
4.7 Acknowledgments
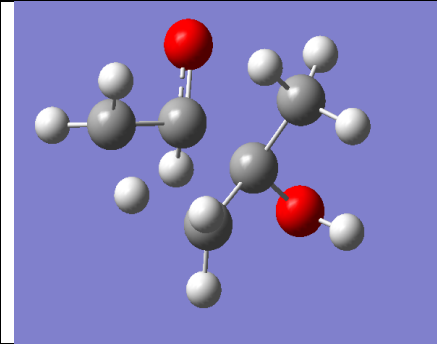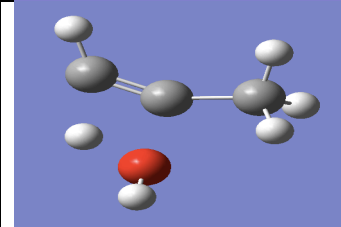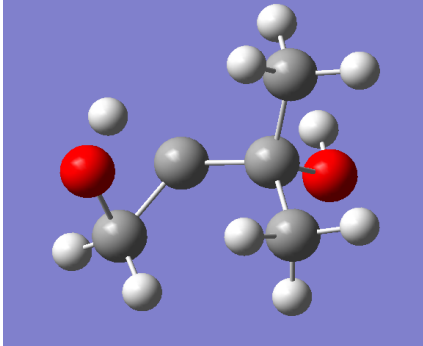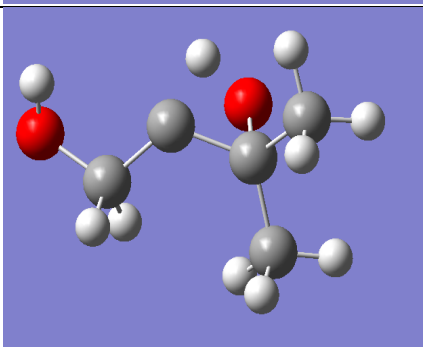
4.8 Supporting Information
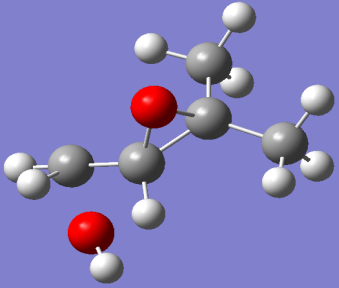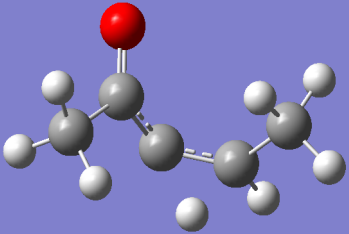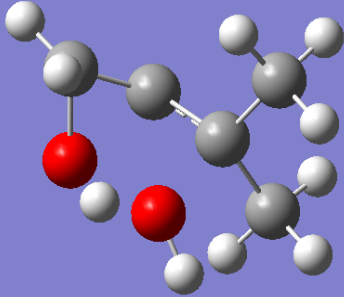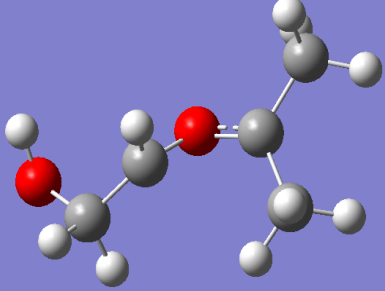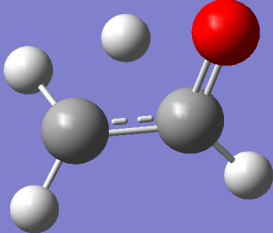
Table S1. Optimized molecular structures using the CBS-QB3 model of all the species presented in Fig. 15 a.

Species	Structure	*m/z*
TS1		102
TS2		84
TS3		84
TS4a		56
TS4b		56
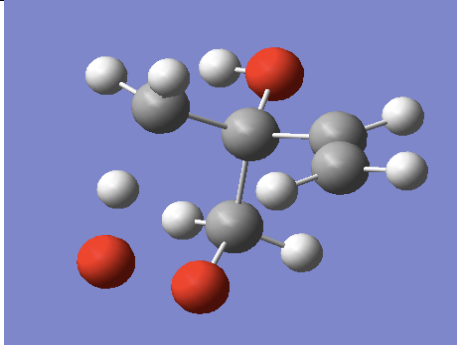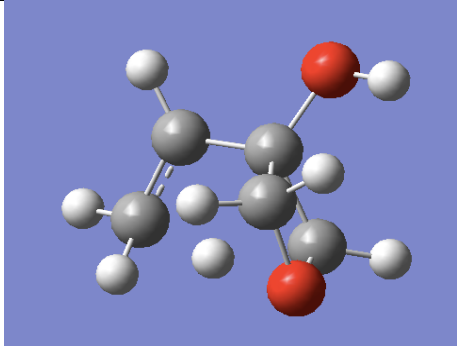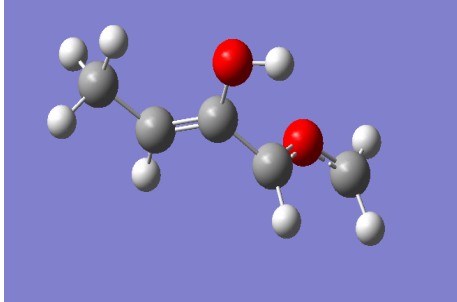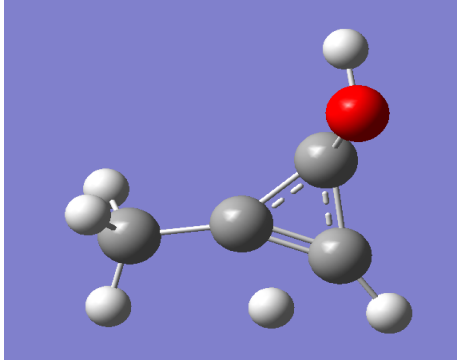
Species	Structure	m/z
TS1*		102
TS2*		58
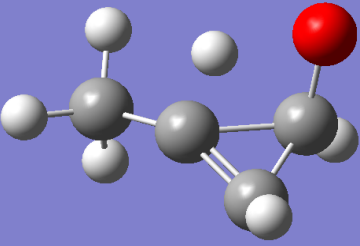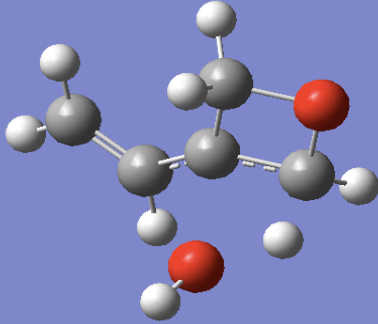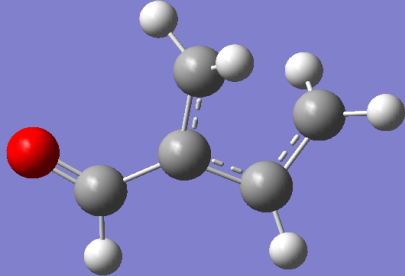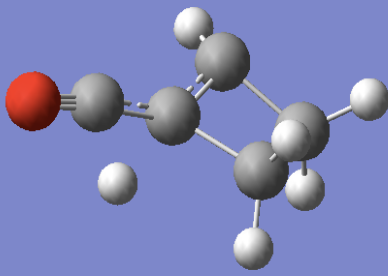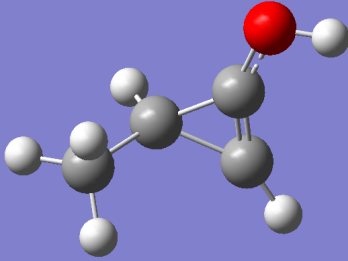
Table S2. Optimized molecular structures using the CBS-QB3 model of all the species presented in Fig. 15 b.

Species	Structure	*m/z*
TS1		102
TS2		102

TS3		84
TS4		84
TS2*		102
TS3*		102
TS4*		44

Table S3. Optimized molecular structures using the CBS-QB3 model of all the species presented in Fig. 16.

Species	Structure	*m/z*
TS1		117
TS2		100
TS3		100
TS4		70

TS5		70
TS2*		100
TS3*		82
TS4*		82
TS4**		70

TS5**		70
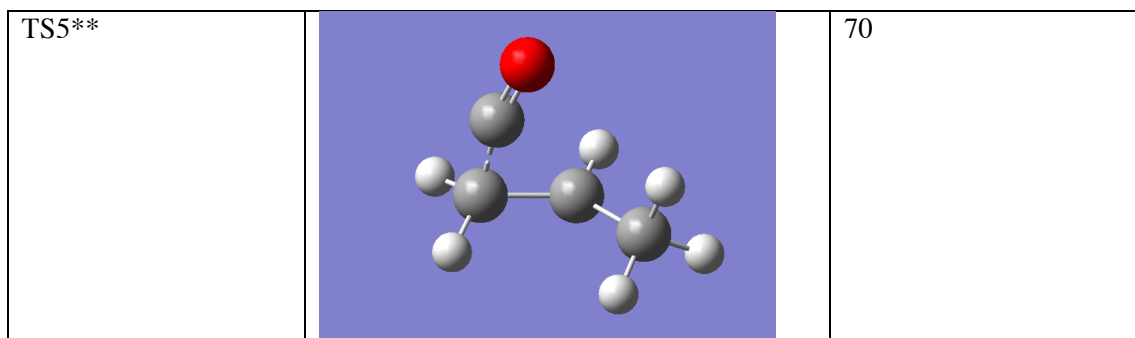
Table S4. Optimized geometries for neutral species calculated for this work in Figure 15a. All calculations were conducted using the CBS-QB3 model.

MBO Neutral

C	-1.140138645	1.599837135	-0.997759073
C	-0.840846331	0.66392199	0.185430866
C	-0.440911367	-0.725274078	-0.30345361
C	0.187284072	1.309621538	1.095519439
C	1.414508407	0.882144959	1.370966638
O	-2.053250311	0.45186613	0.940732752
H	-1.946230507	1.180461079	-1.604656328
H	-0.257307898	1.743113139	-1.626150251
H	-1.459129906	2.584748397	-0.640313664
H	2.358599864	1.3084372	1.258231146
H	-1.254425658	-1.143261688	-0.899297578
H	0.458667918	-0.686628099	-0.921057722
H	-0.263645678	-1.38833524	0.544935007
H	-0.158946013	2.235928928	1.556236379
H	2.062828988	1.433890839	2.042459321
H	1.82199079	-0.02759223	0.944784677

E

C	-1.365648805	1.728836668	-0.865746855
C	-0.84187062	0.727774989	0.171061457
C	-0.350427779	-0.550808675	-0.499608786
C	0.236422234	1.410713042	1.013162771
C	1.434729466	0.755121066	1.542573052
O	-1.90038128	0.32489597	1.057145778
H	-2.176922982	1.281234834	-1.443957355
H	-0.568500714	2.034988436	-1.547443475
H	-1.749663002	2.630736469	-0.375608328

H	-2.345558307	1.11861455	1.372680829
H	-1.114413419	-0.927447238	-1.182093697
H	0.565635932	-0.359631399	-1.061449617
H	-0.160558527	-1.321015745	0.249862456
H	-0.142670657	2.272516556	1.567795009
H	1.888979523	1.134643672	2.454585037
H	1.62483144	-0.291480313	1.327348898
O	1.51418706	1.637314138	0.409922577

E1

C	-1.649957	1.061916	-0.070677
C	-0.801972	-0.169255	0.104741
C	-1.250876	-1.408847	-0.08707
C	0.603532	0.09107	0.549046
C	1.772048	-0.516301	-0.09687
H	-2.657422	0.812255	-0.407415
H	-1.188275	1.732793	-0.801221
H	-1.728443	1.62144	0.868774
H	-2.276821	-1.600585	-0.383466
H	-0.611445	-2.273661	0.051269
H	0.708254	0.41449	1.586192
H	2.687326	-0.663336	0.472103
H	1.621812	-1.196763	-0.930462
O	1.426046	0.850234	-0.356349

E2

C	-1.303328	0.145618	0.589167
C	0.122907	0.411887	0.172463
C	0.590336	1.605943	-0.203582
C	1.062172	-0.751887	0.184606
C	-2.116718	-0.58671	-0.492631
H	-1.791225	1.091591	0.838315
H	-1.30463	-0.45549	1.506995
H	-3.134827	-0.783532	-0.146926
H	-0.037112	2.490331	-0.218753
H	1.627144	1.711093	-0.502535
H	0.621841	-1.69592	0.575153
H	-1.663631	-1.546887	-0.755577
H	-2.174907	0.012743	-1.404574
O	2.215642	-0.72163	-0.174029

E3

C	-1.073487	-0.847085	-0.000323
C	0.379337	-0.405598	0.000113
C	1.461932	-1.465596	0.000241
C	0.711149	0.863182	-0.000142
C	-2.103793	0.284264	0.000286
H	-1.236171	-1.489393	0.875392
H	-1.23608	-1.488364	-0.876813
H	-3.118294	-0.1207	-0.000086
H	1.374165	-2.106817	0.88469
H	1.374617	-2.106675	-0.884356
H	2.464034	-1.033222	0.000532
H	-1.999254	0.919573	-0.883765
H	-1.999401	0.918426	0.885172
O	1.015695	1.991522	-0.000227

E4

C	0.496063	0.408261	-0.113622
C	-0.601064	-0.56233	-0.211023
C	-1.914668	0.032666	0.095918
C	1.904241	-0.146095	0.115396
H	0.292784	1.30302	0.505163
H	0.414339	0.776167	-1.163463
H	2.667627	0.618505	-0.052296
H	-2.000207	1.133554	0.099733
H	-2.744376	-0.428921	-0.445362
H	-2.039534	-0.304433	1.143668
H	2.093008	-0.989813	-0.550708
H	2.008926	-0.503095	1.143257

Cis-2-butene

C	0.543206	-0.384823	0.000019
C	-0.543206	0.384823	0.000019
C	-0.543206	1.885943	0.000005
C	0.543206	-1.885943	0.000005
H	-1.522053	-0.094609	-0.00018
H	1.522053	0.094609	-0.00018
H	1.063572	-2.283049	0.879015
H	0.47348	2.28649	-0.000698
H	-1.064739	2.283003	-0.878283
H	-1.063572	2.283049	0.879015

H	1.064739	-2.283003	-0.878283
H	-0.47348	-2.28649	-0.000698

1-Butene

C	-0.539049	0.520068	0.308049
C	0.724158	-0.293849	0.340682
C	1.857721	0.017124	-0.280921
C	-1.727564	-0.246943	-0.294278
H	-0.365419	1.442055	-0.25619
H	-0.796811	0.822427	1.331338
H	-2.636852	0.359816	-0.274299
H	0.676965	-1.216239	0.91954
H	2.733992	-0.618753	-0.221633
H	1.951541	0.923958	-0.87151
H	-1.928386	-1.166523	0.263707
H	-1.526625	-0.525148	-1.332146

E1*

C	1.810786	1.382402	0.163721
C	1.994616	-0.099882	0.012923
C	3.086342	-0.773833	0.37146
O	0.932757	-0.774856	-0.54089
H	1.629345	1.852347	-0.810368
H	2.690335	1.847911	0.607214
H	0.947462	1.603749	0.802667
H	0.229616	-0.151185	-0.742747
H	3.145518	-1.845214	0.231318
H	3.930849	-0.26079	0.808334

Acetaldehyde

C	-0.235687	0.397307	-0.000024
C	1.168775	-0.147701	-0.000026
H	1.70773	0.221575	0.879356
H	-0.305349	1.508865	0.000067

H	1.708268	0.222598	-0.878603
H	1.154974	-1.237462	-0.000541
O	-1.233019	-0.276652	0.000002

Acetone

C	-1.288693	-0.546612	-0.000021
C	0.120808	-0.029886	0.000037
C	1.213132	-0.792418	0.000004
O	0.249642	1.338778	-0.000029
H	-1.832304	-0.192238	0.884017
H	-1.311654	-1.635861	0.000767
H	-1.831866	-0.19343	-0.884781
H	-0.623656	1.740612	0.000154
H	2.198908	-0.346049	-0.000018
H	1.131957	-1.869764	-0.000024

Propyne

C	1.238071	-0.000262	-0.000013
C	-0.21917	0.001144	-0.000067
C	-1.420089	-0.000432	0.000137
H	1.630113	0.448256	0.917064
H	1.630647	0.569009	-0.847244
H	1.628509	-1.019424	-0.069658
H	-2.482138	-0.000542	-0.000502

Table S5. Optimized geometries for neutral species calculated for this work in Figure 15b. All calculations were conducted using the CBS-QB3 model.

F

C	-1.365648805	1.728836668	-0.865746855
C	-0.84187062	0.727774989	0.171061457
C	-0.350427779	-0.550808675	-0.499608786
C	0.236422234	1.410713042	1.013162771
C	1.434729466	0.755121066	1.542573052
O	-1.90038128	0.32489597	1.057145778
H	-2.176922982	1.281234834	-1.443957355
H	-0.568500714	2.034988436	-1.547443475

H	-1.749663002	2.630736469	-0.375608328
H	-2.345558307	1.11861455	1.372680829
H	-1.114413419	-0.927447238	-1.182093697
H	0.565635932	-0.359631399	-1.061449617
H	-0.160558527	-1.321015745	0.249862456
H	-0.142670657	2.272516556	1.567795009
H	1.888979523	1.134643672	2.454585037
H	1.62483144	-0.291480313	1.327348898
O	1.51418706	1.637314138	0.409922577

F1

C	1.963285	0.760467	0.8116
C	0.87937	0.022753	0.036367
C	1.15853	-1.477037	-0.029958
C	-0.503825	0.551254	0.287347
C	-1.605472	-0.387742	0.191179
O	0.796335	0.487122	-1.349483
H	2.949401	0.562252	0.382124
H	1.969576	0.43593	1.856563
H	1.768972	1.835146	0.801984
H	0.769123	1.453702	-1.322144
H	2.170092	-1.653248	-0.403516
H	1.081324	-1.921851	0.965544
H	0.462848	-1.986066	-0.696897
H	-2.772563	1.118984	0.288105
H	-1.526011	-1.197656	-0.543542
H	-1.486079	-0.875989	1.194938
O	-2.890379	0.187158	0.063264

F2

C	2.134615682	-0.926427302	-0.412062152
C	1.008798769	0.002430897	-0.007338694
C	1.37907512	1.47039899	0.032237664
C	-0.385453444	-0.453302105	-0.182213109
C	-1.581861934	0.441531946	-0.39464926
O	0.230698889	-0.468153053	1.112145823
H	2.98028571	-0.813782893	0.27314316
H	2.486950076	-0.700319641	-1.42310816
H	1.80800234	-1.967122116	-0.379834971
H	-0.517709834	-1.450887714	-0.610836017
H	2.228799689	1.616373412	0.705835186
H	1.674512482	1.823987804	-0.960334436

H	0.557912315	2.087936988	0.393458799
H	-2.952986294	-0.945193712	-0.434511386
H	-1.468660351	1.36810251	0.16625571
H	-1.655826938	0.693812499	-1.46395744
O	-2.790096279	-0.14672451	0.077219283

F3

C	2.228868	-1.122101	-0.760779
C	1.157345	-0.521502	0.095566
C	-0.0435	2.309286	-0.017007
C	-0.170602	-0.264223	-0.205348
C	-0.812065	1.036719	-0.403441
O	1.253354	-0.310618	1.327495
H	3.122404	-0.495049	-0.699063
H	1.914632	-1.213569	-1.802502
H	2.491009	-2.111552	-0.376421
H	0.235392	2.26923	1.036987
H	0.873598	2.412002	-0.602219
H	-0.660197	3.196132	-0.182309
H	-1.824516	1.034311	0.016722
H	-0.99086	1.004333	-1.497733

3-penten-2-one

C	-2.338869473	-0.284465862	-3.25686E-06
C	-0.888489424	0.170999713	-4.69913E-06
C	2.270399954	0.456934708	-1.13375E-05
C	0.118324766	-0.925498648	-2.47427E-06
C	1.454360779	-0.795980122	-5.32415E-06
O	-0.607659481	1.355614164	-7.57029E-06
H	-2.994362981	0.584881264	-4.53347E-06
H	-2.54448745	-0.902353427	0.88024747
H	-2.544488065	-0.902356387	-0.880251763
H	2.929457983	0.468245899	-0.876253328
H	1.651813622	1.349106174	-1.50232E-05
H	2.929458431	0.468253958	0.876230273
H	2.029927031	-1.721034073	-3.07931E-06
H	-0.292876692	-1.931325363	1.64689E-06

3-methyl-2-butenal

C	2.559484937	0.678023425	0.420493202
C	1.216179723	0.168318429	-0.02611089
C	0.360803797	1.16586541	-0.754014682
C	0.852882788	-1.105241145	0.234025216
C	-0.408233969	-1.777784652	-0.120060641
H	2.43850643	1.540567083	1.085643607
H	3.139521119	1.030090059	-0.440112085
H	3.140000232	-0.083957849	0.942161057
H	0.192575387	2.04237079	-0.117171335
H	0.891695212	1.528999117	-1.641965277
H	-0.595351732	0.747006155	-1.051555713
H	-0.444560457	-2.836546514	0.218741004
H	1.554446902	-1.740371034	0.769557014
O	-1.359180369	-1.310505273	-0.714228479

Ethenol

C	-2.023553248	1.013227657	-0.187195976
C	-2.260879697	-0.065753284	0.554835214
H	-1.722810888	0.945984194	-1.227978166
H	-1.906410862	-1.399979313	-0.759945681
H	-2.561483874	-0.003250979	1.594798507
H	-2.128094281	1.999709609	0.242089403
O	-2.174483148	-1.366512886	0.166031699

Acetone

C	2.483864881	-1.192822883	0.065494122
C	1.426617121	-0.103745224	0.003729494
C	1.929119991	1.329668864	0.025998749
O	0.247544338	-0.364037573	-0.059786155
H	2.004439794	-2.170500507	0.049572489
H	3.085016337	-1.091129175	0.974610782
H	3.171110986	-1.105549887	-0.782106549
H	2.499107354	1.519711355	0.9410633
H	2.606673557	1.510496135	-0.814506217
H	1.084643642	2.015084895	-0.02893799

Acetaldehyde

C	-0.235687	0.397307	-0.000024
C	1.168775	-0.147701	-0.000026

H	1.70773	0.221575	0.879356
H	-0.305349	1.508865	0.000067
H	1.708268	0.222598	-0.878603
H	1.154974	-1.237462	-0.000541
O	-1.233019	-0.276652	0.000002

Table S6. Optimized geometries for neutral species calculated for this work in Figure 16. All calculations were conducted using the CBS-QB3 model.

Radical C

C	-0.928926	-0.556739	1.299927
C	-0.413412	1.511323	-0.026998
C	-0.394154	-0.021522	0.006706
C	0.988049	-0.620277	-0.181792
C	2.157865	-0.010332	-0.008332
H	-1.213068	-1.601143	1.354476
H	-0.824942	0.005488	2.220005
H	-2.091333	-0.358325	-0.902062
H	-1.441258	1.868514	0.08159
H	-0.020243	1.866154	-0.980679
H	0.175867	1.943339	0.785643
H	2.237344	1.035023	0.267623
H	3.08983	-0.547349	-0.142641
H	0.954386	-1.669944	-0.460852
O	-1.16539	-0.544559	-1.09502

Radical D

C	-0.757794	-0.687936	-0.697607
C	1.725488	-0.867133	-0.829044
C	0.561943	-0.420077	0.06306
C	0.636383	1.027996	0.494528
C	1.421014	1.968444	-0.018032
H	-0.863765	-1.758651	-0.896653
H	-0.814629	-0.118194	-1.625038
H	0.520338	-2.09983	1.079537
H	1.629361	-1.930771	-1.069601
H	2.66633	-0.721558	-0.297051
H	1.762205	-0.315425	-1.771234
H	2.118192	1.778932	-0.826302
H	1.389109	2.982716	0.362341
H	-0.040165	1.269193	1.308073

O	0.565051	-1.160696	1.290189
O	-1.923346	-0.349826	0.096494
O	-2.377852	0.85875	-0.179371

D1

C	0.928245	0.276943	-1.040007
C	0.728302	0.49847	1.011434
C	0.06184	-0.482701	0.013516
C	-1.42432	-0.355774	-0.179643
C	-2.154379	0.732534	0.039521
H	0.408078	0.708315	-1.897832
H	1.794437	-0.307698	-1.3799
H	1.273012	-1.983181	0.276184
H	1.499915	0.016576	1.626584
H	0.069205	1.091201	1.650144
H	-1.725884	1.657398	0.411457
H	-3.218742	0.739449	-0.163173
H	-1.886756	-1.259952	-0.566026
O	0.322208	-1.860997	0.186957
O	1.296368	1.276131	-0.065252

D2

C	-1.59548	0.27112	-0.497067
C	-0.250133	-0.740891	0.699626
C	-0.15588	0.556408	-0.083073
C	0.726417	-0.611837	-0.446778
C	2.196543	-0.493933	-0.106034
H	-1.810052	0.160281	-1.564389
H	-2.321399	0.949706	-0.034274
H	-0.104993	2.20808	0.894994
H	0.000107	-1.045645	1.709059
H	2.732693	0.066331	-0.876264
H	2.346724	0.033056	0.838781
H	2.652196	-1.484453	-0.023035
H	0.493637	-1.172014	-1.351274
O	0.382116	1.805486	0.167585
O	-1.57183	-1.005553	0.20821

D3

C	-3.13004	-0.162581	-0.000091

C	-0.793424	-0.633454	0.000061
C	0.49171	-0.008352	-0.000054
C	1.645328	-0.717465	-0.000038
C	3.014372	-0.116093	0.000045
H	-3.427656	-1.200905	0.000029
H	-3.79499	0.681609	0.000297
H	-0.375323	1.692091	-0.000162
H	-0.933347	-1.706702	-0.000003
H	3.590631	-0.429647	-0.879429
H	2.966221	0.972905	0.001131
H	3.591218	-0.431474	0.878455
H	1.557864	-1.798697	-0.000137
O	0.530096	1.362684	-0.000009
O	-1.847883	0.143378	0.000045

D4

C	0.176537	-1.256233	0.171568
C	0.72255	-0.102996	-0.046531
C	-0.680934	-0.162255	-0.498228
C	-1.80999	0.539935	0.241333
H	2.499101	0.296431	0.436765
H	0.18862	-2.270479	0.526394
H	-2.749792	-0.011845	0.134321
H	-1.584898	0.622893	1.308319
H	-1.97477	1.549009	-0.151503
H	-0.866781	-0.255563	-1.573757
O	1.754943	0.744855	0.013826

D5

C	0.002571	0.239041	-0.004317
C	-1.204019	-0.402674	0.000047
C	1.154912	-0.570751	-0.005409
C	2.437024	0.185564	0.000669
H	-2.310327	1.12646	0.001034
H	0.000523	1.344315	-0.007619
H	3.066255	-0.174111	-0.823654
H	2.384948	1.289142	-0.038275
H	2.994841	-0.109928	0.900324
H	-1.245799	-1.485282	0.001516
O	-2.40417	0.162791	0.002592

2-butenal

C	0.06653	0.690236	0.000047
C	1.518765	0.411703	-0.000058
C	-0.838565	-0.295627	-0.000006
C	-2.320475	-0.122096	0.000093
H	-0.455835	-1.314519	-0.000133
H	-0.236511	1.73438	0.000138
H	-2.763956	-0.607898	0.876621
H	-2.613575	0.929529	-0.000013
H	-2.764139	-0.608157	-0.876193
H	2.166177	1.31459	-0.000101
O	2.013789	-0.694153	-0.000098

D5**

C	-0.251609	1.268111	-0.19432
C	-0.809314	-0.073563	0.054107
C	0.575258	0.126284	0.509839
C	1.746675	-0.5271	-0.196518
H	1.535726	-0.670648	-1.259495
H	0.01829	1.53056	-1.213908
H	-0.577211	2.105162	0.415489
H	1.960457	-1.508788	0.234058
H	2.64695	0.088296	-0.109856
H	0.702458	0.273416	1.580592
O	-1.731592	-0.822548	-0.085691

Propene

C	1.280463	0.220496	-0.000011
C	0.134691	-0.453663	0.00001
C	-1.233503	0.162312	-0.000001
H	-1.807057	-0.151727	0.87926
H	1.301452	1.306478	-0.000058
H	2.238784	-0.286536	0.000162
H	-1.807812	-0.15467	-0.877651
H	-1.181938	1.253645	-0.001713
H	0.166665	-1.542057	0.000017

D2*

C	1.134776	-0.924344	0.000103
C	0.805048	1.013595	-0.000116
C	-0.033268	-0.251025	0.000387
C	-1.434222	-0.559586	-0.000164
C	-2.429582	0.338307	0.0001
H	1.501426	-1.942256	0.00046
H	0.786341	1.627948	0.901003
H	0.785756	1.627223	-0.901727
H	-2.237028	1.406251	0.000851
H	-3.467059	0.029188	-0.000503
H	-1.680759	-1.619293	-0.000922
O	2.006851	0.146157	-0.000128

D3*

C	-1.513001	0.466958	0.000003
C	0.749813	-1.06032	-0.000069
C	-0.07376	0.216068	-0.00005
C	0.99785	1.032761	-0.000227
C	1.998719	-0.104061	0.000056
H	-1.798467	1.541954	0.000066
H	0.642943	-1.68547	0.888786
H	0.643111	-1.685617	-0.888851
H	2.634105	-0.169061	-0.887922
H	2.634021	-0.169026	0.888112
H	1.111344	2.111631	-0.000322
O	-2.353098	-0.406606	0.000231

Cyclobutene

C	-0.699193	-0.787011	0.000061
C	0.815145	-0.667837	-0.00002
C	0.813461	0.669529	-0.000093
C	-0.700852	0.785527	-0.000096
H	1.602953	-1.412639	-0.000363
H	-1.142436	-1.247046	-0.88826
H	-1.141907	-1.246397	0.888995
H	-1.144687	1.244352	0.888554

H	-1.144855	1.24423	-0.888695
H	1.599571	1.41625	0.000656

Table S7. Optimized geometries for the transition states from Figure 15a. All calculations were conducted using the CBS-QB3 model.

TS1

C	0.524952	-1.093446	1.16928
C	0.492385	-0.353433	-0.13387
C	1.4708	-0.606682	-1.138847
C	-0.760349	0.346786	-0.515558
C	-2.072888	-0.323434	-0.397411
O	1.538545	1.319181	0.306896
H	1.555016	-1.247442	1.490036
H	0.070408	-2.082354	1.031689
H	-0.030683	-0.560432	1.939136
H	1.900489	1.577786	1.167378
H	2.105304	-1.476991	-0.998312
H	1.202828	-0.387655	-2.168818
H	2.020404	0.468966	-0.567773
H	-0.633493	1.095541	-1.2915
H	-2.861545	-0.05753	-1.096955
H	-2.137574	-1.323341	0.023957
O	-1.678615	0.702657	0.514304

TS2

C	1.292177	1.349698	0.088166
C	0.857032	0.005797	-0.093223
C	1.62945	-1.196147	-0.031716
C	-0.579508	-0.177681	-0.525622
C	-1.645126	-0.628152	0.377085
H	1.024799	-0.024378	1.075547
H	2.319035	1.569752	0.348417
H	0.552494	2.134364	0.111304
H	2.692983	-1.167361	0.162582
H	1.122724	-2.149543	-0.046041
H	-0.663865	-0.41121	-1.585206
H	-2.49074	-1.186043	-0.017007
H	-1.415764	-0.805668	1.425343
O	-1.558228	0.739874	-0.045386

100

TS3

C	-1.238569	-1.828462	-0.087361
C	-0.64868	-0.46919	0.104009
C	-1.287431	0.823507	0.028698
C	0.61088	-0.04456	0.469864
C	-0.625155	-2.912332	0.8078
H	-1.165454	-2.128905	-1.141478
H	-2.317091	-1.736031	0.102242
H	-1.077985	-3.886115	0.605741
H	-2.265263	0.968547	0.504747
H	-1.119189	1.512838	-0.794066
H	0.149223	1.262779	0.358847
H	-0.775373	-2.677882	1.864237
H	0.451055	-2.998015	0.640233
O	1.627625	-0.253613	1.065475

TS4a

C	-0.491902	0.337447	-0.052875
C	0.572225	-0.565472	0.027502
C	1.931718	0.077064	0.04427
C	-1.943266	-0.069709	0.063856
H	-0.087741	-0.247491	-1.098077
H	-0.319862	1.430669	-0.031108
H	-2.580174	0.454078	-0.654729
H	1.961316	1.167054	-0.131433
H	2.330581	-0.107413	1.049604
H	2.626402	-0.419553	-0.63795
H	-2.296545	0.19557	1.0653
H	-2.046626	-1.148895	-0.058124

TS4b

C	0.525636	0.594041	0.083512
C	-0.650787	-0.069352	-0.585166
C	-1.767343	-0.232065	0.233022
C	1.723466	-0.374047	0.048965
H	0.337078	0.900661	1.129123
H	0.799832	1.491875	-0.480881
H	2.604412	0.091374	0.498169
H	-1.756778	0.692371	-0.629532

H	-2.649495	-0.756309	-0.136383
H	-1.788408	0.015348	1.308951
H	1.960476	-0.65751	-0.978403
H	1.50705	-1.289279	0.606961

TS1*

C	0.330484	0.983541	1.059217
C	-0.007541	0.214715	-0.209442
C	-0.346452	-1.208434	-0.033279
C	-1.42061	0.842375	-0.874529
C	-2.491187	-0.057877	-0.30377
O	0.955976	0.42991	-1.240398
H	1.310334	0.691206	1.453496
H	-0.413697	0.811532	1.841124
H	0.332469	2.049952	0.829593
H	1.824131	0.214461	-0.883664
H	-0.024254	-1.891322	-0.814716
H	-0.417042	-1.637538	0.962258
H	-1.725251	-1.12545	-0.292751
H	-1.253009	0.64501	-1.955154
H	-3.415968	-0.187121	-0.868373
H	-2.67129	0.090636	0.760055
O	-1.81432	2.033104	-0.545485

TS2*

C	1.514234	-0.142314	-0.005261
C	0.112927	0.324161	0.018745
C	-0.800994	1.231721	0.01521
O	-0.927988	-1.058996	-0.105381
H	1.761886	-0.760483	0.863347
H	2.167304	0.734253	0.004941
H	1.724769	-0.7239	-0.906338
H	-0.994955	-1.477366	0.766995
H	-1.552634	-0.08391	-0.091158
H	-0.639468	2.301958	0.03309

Table S8. Optimized geometries the transition states from Figure 15b. All calculations were conducted at the CBS-QB3 level.

TS1

C	-1.351363	-1.353865	0.140217
C	-0.698695	0.019903	-0.017734
C	-0.732724	0.804759	1.29003
C	0.635083	-0.091734	-0.739092
C	1.822269	0.618371	-0.211214
O	-1.4246	0.82605	-0.976841
H	-2.384229	-1.242548	0.479236
H	-0.805252	-1.959304	0.868939
H	-1.347388	-1.88921	-0.812992
H	-1.428692	0.339341	-1.811032
H	-1.745501	0.803649	1.698703
H	-0.060843	0.354903	2.024852
H	-0.439986	1.842439	1.121992
H	1.476719	-1.191873	-0.616037
H	2.60418	0.915252	-0.90917
H	1.709706	1.307229	0.621166
O	1.971333	-0.734111	0.296979

TS2

C	2.082407	-0.827629	-0.628142
C	0.948115	-0.013814	-0.033778
C	1.262664	1.468428	0.07655
C	-0.439161	-0.489619	-0.293131
C	-1.583338	0.452593	-0.279565
O	0.485077	-0.540369	1.252515
H	2.991972	-0.704715	-0.032978
H	2.293091	-0.497857	-1.650077
H	1.81649	-1.884807	-0.657425
H	-0.166411	-1.339414	0.743855
H	2.218115	1.613701	0.586418
H	1.346674	1.90913	-0.92096
H	0.497595	2.005775	0.634964
H	-2.770909	-1.055062	-0.465767
H	-1.503079	1.244414	0.470108
H	-1.551586	0.943635	-1.273178
O	-2.834585	-0.18145	-0.063336

TS3

C	1.832584	-1.052745	-0.617424
C	0.951391	0.027049	-0.031669
C	1.312207	1.450341	-0.379889
C	-0.422092	-0.29875	0.378423
C	-1.639381	0.636692	0.383514
O	0.596992	-0.186615	1.362807
H	2.867336	-0.918484	-0.288402
H	1.81666	-1.014648	-1.710523
H	1.502402	-2.042819	-0.297088
H	-0.790824	-1.312541	0.236714
H	2.330346	1.675153	-0.048914
H	1.26138	1.604676	-1.46157
H	0.628817	2.150415	0.101861
H	-2.334503	-0.857109	-0.874864
H	-2.151476	0.067988	1.209711
H	-2.510425	1.306058	0.387156
O	-2.305394	0.106276	-0.89744

TS4

C	-1.836363	-0.842534	0.503672
C	-0.910972	0.176003	-0.142357
C	2.03972	0.202528	0.773588
C	0.168197	-0.293556	-0.983972
C	1.483751	-0.351569	-0.524451
O	-1.132865	1.381365	-0.099286
H	-2.390247	-0.351471	1.30442
H	-1.296681	-1.709416	0.897551
H	-2.547323	-1.210097	-0.241778
H	2.480606	1.181452	0.562266
H	1.264391	0.343051	1.526803
H	2.831028	-0.435911	1.173125
H	2.24907	-0.62347	-1.257861
H	0.857894	-1.427085	-0.528372

TS2*

C	1.477702	1.007515	0.730902
C	0.640276	-0.136307	0.192711
C	1.416337	-1.375393	-0.187446
C	-0.609646	-0.356557	0.857044
C	-1.783495	-0.73041	0.084603

O	0.097856	0.593885	-1.404752
H	2.290809	1.268093	0.047064
H	1.922281	0.699346	1.680975
H	0.863025	1.88756	0.928205
H	0.648533	1.365397	-1.571011
H	2.226098	-1.117492	-0.871875
H	1.854344	-1.826574	0.707196
H	0.772374	-2.113128	-0.667515
H	-0.925296	0.910074	-0.672394
H	-1.733825	-1.034007	-0.961454
H	-2.663406	-1.089413	0.610755
O	-1.610603	0.730747	0.242648

TS3*

C	2.496873	-0.787624	0.388115
C	1.333927	0.068103	0.035061
C	1.502641	1.378962	-0.657831
C	-0.693946	-0.247141	-0.508362
C	-2.062612	0.25257	-0.257643
O	0.171558	-0.342043	0.566971
H	2.319001	-1.25568	1.362764
H	3.428852	-0.216635	0.407753
H	2.633917	-1.60804	-0.331891
H	-0.441165	-0.88359	-1.343326
H	2.349179	1.922318	-0.207519
H	1.724184	1.301601	-1.72839
H	0.58263	1.962013	-0.570508
H	-2.743792	-1.48326	0.32312
H	-2.063024	1.232261	0.228932
H	-2.568942	0.363218	-1.22685
O	-2.84343	-0.576894	0.634442

TS4*

C	0.276331	-0.460657	-0.51212
C	1.045502	0.593015	0.027741
H	0.064031	-1.233368	0.229363
H	1.734029	-0.808077	-0.340549
H	0.793765	1.64556	0.180474
H	-0.548281	-0.284054	-1.196762
O	2.22035	0.189727	0.32533

Table S9. Optimized geometries for the transition states from Figure 16. All calculations were conducted using the CBS-QB3 model.

TS1

C	0.607043	-0.518514	-1.005119
C	0.023025	-0.451071	1.439531
C	-0.561677	-0.478594	0.042615
C	-1.463651	0.696722	-0.255555
C	-1.247927	1.953253	0.115416
H	0.218068	-0.352082	-2.010365
H	1.115827	-1.488708	-0.950096
H	-0.844632	-2.427608	0.031385
H	0.281977	-1.426961	1.848951
H	-0.423359	0.231055	2.156884
H	1.307061	0.043522	1.151451
H	-0.391333	2.245571	0.71277
H	-1.924837	2.745273	-0.182696
H	-2.320607	0.437379	-0.870504
O	-1.371396	-1.648479	-0.177174
O	1.527826	0.525568	-0.760075
O	2.198689	0.220633	0.448611

TS2

C	-0.979123	-0.462889	-0.937484
C	-0.391632	-0.634752	0.984345
C	-0.155316	0.547543	0.019833
C	1.245551	0.68107	-0.330958
C	2.05789	-0.433006	0.054862
H	-0.540904	-0.743205	-1.897057
H	-1.995166	-0.082626	-1.058071
H	-1.703736	1.671876	0.38388
H	-0.939985	-0.582015	1.930904
H	1.472171	-0.768655	1.038992
H	1.878537	-1.388992	-0.466494
H	3.133561	-0.2477	0.088883
H	1.601923	1.562313	-0.848189
O	-0.760107	1.805321	0.233873
O	-0.936221	-1.506421	0.026572

TS3

C	-2.876365	-0.324239	0.460719
C	-0.772442	-0.694461	-0.578318
C	0.67114	-0.533983	-0.362462
C	1.437771	-1.455357	0.231464
C	2.919348	-1.341388	0.435654
H	-3.454157	-0.804529	-0.318584
H	-3.290553	0.131148	1.343311
H	0.549296	1.160627	-1.233785
H	-1.214577	-1.234068	-1.409261
H	3.447779	-2.177427	-0.036672
H	3.304804	-0.411828	0.017323
H	3.173275	-1.368767	1.501589
H	0.941986	-2.350483	0.589772
O	1.252729	0.631591	-0.844851
O	-1.583089	-0.257349	0.3617

TS4

C	-0.074802	0.559337	1.280684
C	0.909692	0.304299	0.295787
C	-0.481731	-0.012619	0.117647
C	-1.483105	-0.753844	-0.671694
H	2.289274	0.854898	-0.907638
H	-0.341089	0.826441	2.293563
H	-1.612674	-0.281701	-1.648355
H	-1.075101	-1.756847	-0.845213
H	-2.44743	-0.823382	-0.168886
H	-1.283684	1.417342	0.500761
O	1.627814	1.293976	-0.366442

TS5

C	0.471683	1.263729	-0.003971
C	0.777489	-0.054319	0.594546
C	-0.477582	0.283726	-0.225083
C	-1.834377	-0.293105	0.013859
H	0.247416	-0.370019	-1.122715
H	1.020677	1.872057	-0.721239
H	-2.195114	-0.02203	1.009493
H	-2.545049	0.074574	-0.730824
H	-1.794886	-1.381549	-0.06111
H	0.698481	-0.289864	1.650962

O	1.36815	-0.885419	-0.287585

TS4**

C	0.178395	1.259105	-0.178796
C	0.724082	0.109619	0.054556
C	-0.678797	0.175177	0.507139
C	-1.803504	-0.547799	-0.242013
H	2.482371	-0.322591	-0.469063
H	0.177787	2.261091	-0.567347
H	-2.618609	-0.81207	0.437144
H	-2.221143	0.081946	-1.033121
H	-1.451633	-1.473212	-0.707886
H	-0.863379	0.285727	1.579482
O	1.746695	-0.749687	-0.010566

TS5**

C	-0.160995	1.231611	-0.209404
C	-1.085117	0.113061	-0.093847
C	0.831173	0.409614	0.494729
C	1.584928	-0.686047	-0.191437
H	1.038408	-1.648207	-0.22788
H	0.017615	1.482422	-1.261667
H	-0.540517	2.115156	0.308613
H	2.52611	-0.887158	0.328396
H	1.84218	-0.423695	-1.225196
H	0.775046	0.413527	1.576258
O	-1.603069	-0.926831	0.054812

TS2*

C	1.116571	0.050507	0.896392
C	0.598798	-1.026888	-0.737949
C	-0.122973	-0.088587	0.188924
C	-1.502013	0.181997	0.472988
C	-2.522563	-0.463424	-0.108717
H	1.27987	-0.007634	1.970282
H	1.273058	1.201695	0.40433
H	0.447208	2.568066	-1.161532
H	0.729217	-0.687117	-1.76536
H	0.212933	-2.052358	-0.708576
H	-2.363188	-1.219557	-0.869755
H	-3.548965	-0.25624	0.167164

H	-1.687354	0.935567	1.231046
O	0.475957	1.856579	-0.500709
O	1.80533	-0.907086	0.05853

TS3*

C	-1.114296	0.056035	1.296623
C	0.050911	-0.077405	-1.002203
C	0.024821	-0.222062	0.420081
C	1.224958	-0.850582	0.716354
C	1.609524	-1.46625	-0.50024
H	-0.921575	-0.118779	2.377636
H	-0.84329	-0.201387	-1.612912
H	0.829322	0.526575	-1.445806
H	2.649131	-1.572537	-0.812909
H	0.934135	-2.180273	-0.952796
H	1.822492	-0.794292	1.621701
O	-2.200528	0.430892	0.907389

TS4*

C	1.490853	0.090747	-0.038257
C	-0.889036	-1.048938	-0.077388
C	0.098586	0.15146	0.109823
C	-0.963422	1.080245	-0.177084
C	-2.026572	0.011798	0.029172
H	0.58152	-0.040469	1.275337
H	-0.787854	-1.507914	-1.060082
H	-0.835779	-1.808564	0.706678
H	-2.509553	-0.05138	1.019804
H	-2.815106	-0.054744	-0.729618
H	-0.995466	2.115805	0.143475
O	2.637472	-0.045576	-0.05415

4.9 References

1. *Criteria Air Pollutants;* United States Envriontional Protection Agency: Research Triangle Park, NC, **2016**.
2. *Climate Change: Basic Information;* United States Environmental Protection Agency: Washington, DC, **2016.**
3. *The High Cost of Fossil Fuels;* Environment America. Boston, MA, **2016**.
4. Huber, G. W.; Iborra, S.; Corma, A. Synthesis of Transportation Fuels from Biomass: Chemistry, Catalysts, and Engineering. *Chem. Rev.* **2006**, 106, 4044.
5. Wymann, C. E. Appl. Biochem. *Biotech*. **1994**, 45/46.
6. Klass, D. L. Biomass for Renewable Energy, Fuels and Chemicals. **1998**, San Diego: Academic Press.
7. Westphal, G.A.; Krahl, J.; Brüning, T.; Hallier, E.; Brünger, J. Ether Oxygenated Additives in Gasoline Reduce Toxicity of Exhausts. *Toxicology* **2010**, 268, 198-203
8. Lenin, A. H.; Ravi, R.; Arrumugham, S.; Thyagarajan, K., Performance, Emission and Combustion Evaluation of Diesel Engine Using Methyl Esters of Mahua oil. *Int. J. Env. Sci.* **2012**, 3 (1).
9. Kremer, F.; Blank, L. M.; Jones, P. R.; Akhtar, M. K. A Comparison of the Microbial Production and Combustion Characteristics of Three Alcohol Biofuels: Ethanol, 1-Butanol, and 1-Octanol. *Front. Bioeng.g and Biotech.* **2015** *3*, 112.
10. Gupta,D.; Ip, T.; Summers, M. L.; Basu, C. 2-Methyl-3-buten-2-ol (MBO) synthase expression in Nostoc punctiforme leads to over production of phytols. *Bioeng.***2015**, *6* (1), 33-41.
11. Miller, J. A.; Kee, R. J.; Westbrook, C. K. Chemical Kinetics and Combustion Modeling. *Annu. Rev. Phys. Chem.* **1990**, 41, 345-387
12. Cvetanovic, R. J.; Singleton, D. L. Reaction of Oxygen Atoms with Olefins. *Rev. Chem. Int.* **1984,** 5, 183-226
13. Cvetanovic, R. J. Evaluated Chemical Kinetics Data for the Reactions of Atomic Oxygen $O(^3P)$ with Unsaturated Hydrocarbons. *J. Phys. Chem. Ref. Data.* **1987,** 1 261-326
14. Taatjes, C. A.; Osborn, D. L.; Selby, T. M.; Meloni, G.; Trevitt, A. J.; Epifanovsky, E.; Krylov, A. I.; Sirjean, B.; Dames, E.; Wang, H.Products of the Benzene+$O(^3P)$ Reaction *J. Phys. Chem. A* **2010**, 114, 3355– 3370
15. Savee, J. D.; Welz, O.; Taajtes, C. A.; Osborn, D.L. New Mechanistic Insights on the $O(^3P)$ + Propene Reaction from Multiplexed Photoionization Mass Spectrometry. *Phys. Chem. Chem. Phys.* **2012,** 14, 10410-10423
16. Leonori, F.; Occhiogrosso, A.; Balucani, N.; Bucci, A.; Petrucci, R.; Casavecchia, P. Crossed Molecular Beam Dynamics Studies of the $O(^3P)$ + Allene Reaction: Primary Products, Branching Rations, and Dominant Role of Intersystem Crossing. *J. Phys. Chem. Lett.* **2012**, 3, 75-80
17. Ng, M. Y.; Nelson, J.; Taatjes, C.A.; Osborn, D.L.; Meloni, G. Sycnhrotron Photoinization Study of Mesitylene Oxidation Initiated by Reaction with $Cl(^2P)$ or $O(^3P)$ Radicals. *J. Phys. Chem. A* **2014**, *118*, 3735-3748.
18. Ray, A. W.; Taatjes, C.A.; Welz, O.; Osborn, D.L.; Meloni, G. Synchrotron Photoionization Measurements of OH-Intitiated Cyclohexene Oxidation: Ring-   Preserving Products in OH + Cyclohexene and Hydroxycyclohexyl + O_2 Reaction. *J. Phys. Chem. A* **2012**, *116*, 6720-6730.
19. Ng, M. Y.; Bryan, B. M.; Nelson, J.; Meloni, G., Study of tert-Amyl Methyl Ether Low Temperature Oxidation Using Synchrotron Photoionization Mass Spectrometry. *J. Phys. Chem. A* **2015**, *119* (32), 8667-82.

20. Troe, J.Are Primary Quantum Yields of NO_2 Photolysis at $\lambda \le 398$ nm Smaller Than U nity? *Z. Phys. Chem.* **2000**, 214, 573– 581

21. Vandaele, A. C.; Hermans, C.; Simon, P. C.; Carleer, M.; Colin, R.; Fally, S.; Mérienne, M. F.; Jenouvrier, A.; Coquart, B.Measurements of the No_2 Absorption Cross-Section from 42000 cm^{-1} to 10000 cm^{-1} (238–1000 nm) at 220 and 294 K *J. Quant. Spectrosc. Radiat. Transfer* **1998**, 59, 171– 184

22. Muller, G.; Scheer, A.; Osborn, D. L.; Taatjes, C. A.; Meloni, G., Low Temperature Chlorine-Initiated Oxidation of Small-Chain Methyl Esters: Quantification of Chain-Terminating HO_2-Elimination Channels. *J. Phys. Chem. A.* **2016**, *120* (10), 1677-1690.

23. Welz, O.; Zador, J.; Savee, J. D.; Ng, M. Y.; Meloni, G.; Fernandes, R. X.; Sheps, L.; Simmons, B. A.; Lee, T. S.; Osborn, D. L. Low-Temperature Combustion Chemistry of Biofuels: Pathways in the Initial Low-Temperature (550 K-750 K) Oxidation Chemistry of Isopentanol *Phys. Chem. Chem. Phys.* **2012**, *14*, 3112– 3127.

24. Osborn, D. L., et al., The multiplexed chemical kinetic photoionization mass spectrometer: A new approach to isomer-resolved chemical kinetics. *Rev. Sci. Instrum.*, 2008. 79: p. 104103-1/104103-10.

25. Welz, O.; Zador, J.; Savee, J. D.; Ng, M. Y.; Meloni, G.; Fernandes, R. X.; Sheps, L.; Simmons, B. A.; Lee, T. S.; Osborn, D. L. Low-Temperature Combustion Chemistry of Biofuels: Pathways in the Initial Low-Temperature (550 K-750 K) Oxidation Chemistry of Isopentanol *Phys. Chem. Chem. Phys.* **2012**, 14, 3112– 3127.

26. Montgomery, J. A., Jr.; Frisch, M. J.; Ochterski, J. W.; Petersson, G. A. A Complete Basis Set Model Chemistry. VI. Use of Density Functional Geometries and Frequencies *J. Chem. Phys.* **1999**, *110*, 2822– 2827.

27. Montgomery, J. A., Jr.; Frisch, M. J.; Ochterski, J. W.; Petersson, G. A. A Complete Basis Set Model Chemistry. VII. Use of the Minimum Population Localization Method *J. Chem. Phys.* **2000**, *112*, 6532– 6542.

28. Frisch, M. J.; Trucks, G. W.; Schlegel, H. B.; Scuseria, G. E.; Robb, M. A.; Cheeseman, J. R.; Scalmani, G.; Barone, V.; Mennucci, B.; Petersson, G. A.; et al. *Gaussian 09*; Gaussian, Inc.: Wallingford, CT, USA, **2009**.

29. Duschinsky, F. *Physicochim. URSS* **1937**, *7*, 551– 566.

30. Sharp, T. E.; Rosenstock, H. M. Franck—Condon Factors for Polyatomic Molecules *J. Chem. Phys.* **1964**, *41*, 3453– 3463.

31. Lermé, J. Iterative Methods to Compute One- and Two-Dimensional Franck-Condon Factors. Tests of Accuracy and Application to Study Indirect Molecular Transitions *Chem. Phys.* **1990**, *145*, 67– 88.

32. Ruhoff, P. T. Recursion Relations for Multi-Dimensional Franck-CondonOverlap Integrals *Chem. Phys.* **1994**, *186*, 355– 374.

33. Jorgensen, J. T.-R. a. W. L., Performance of B3LYP Density Functional Methods for a Large Set of Organic Molecules. *J. Chem. Theory Comput.* **2008**, *4*, 297-306.

34. Ruscic, B.; Berkowitz, J., The heats of formation of some $C_2H_5O^+$ isomers, relevant bond energies in ethanol and $PA(CH_3CHO)$, *J. Chem. Phys.* **1994**, *101*, 10936.

35. Warneck, P., Heat of formation of the HCO radical, *Z. Naturforsch. A* **1974**, *29*, 350.

36. Cool, T.A.; Nakajima, K.; Mostefaoul, T.A.; Qi, F.; McIlroy, A.; Phillip, R.; Westmoreland, P.R.; Law, M.E.; Poisson, L.; Peterka, D.S.; Ahmed, M. Selective Detection of Isomers with Photoionization Mass Spectrometry for Studies of Hydrocarbon Flame Chemistry. *J. Chem. Phys.* **2003**, *119*, 8356-8365.

37. Trott, W.M.; Blais, N.C.; Walters, E.A. Molecular beam photoionization study of acetone and acetone-d6. *J. Chem. Phys.* **1978**, *69*, 3150.

38.   Cool, T.A.; Wang, J.; Nakajima, K.; Taatjes, C.A.; McIlroy, A. Photoionization cross sections for reaction intermediates in hydrocarbon combustion. *Int. J. Mass Spec.* **2005**, *247* (1-3), 18-27.

39.   Savee, J.D.; Borkar, S.; Welz, O.; Sztaray, B.; Taatjes, C.A.; Osborn, D.L, Multiplexed Photoionization Mass Spectrometry Investigation of the O(^{3}P) + Propyne Reaction. *J. Phys. Chem. A* **2015**, *119* (28), 7388-7403.

40.   Parr, A. C. J., A.J.; Stockbauer, R.; McCulloh, K.E., Photoionization and threhold photoelectron-photoion coincidence study of propyne from onset to 20 eV. *Int. J. Mass Spec. Ion Phys.* **1979**, *30*, 319.

41.   Person, J. C.; Nicole, P. P. Isotope Effects in the Photoionization Yields and the Absorption Cross Sections for Acetylene, Propyne, and Propene *J. Chem. Phys.* **1970**, *53*, 1767–1774.

42.   Bieri, G.; Burger, F.; Heilbronner, E.; Maier, J.P., Valence ionization energies of hydrocarbons, *Helv. Chim. Acta,* **1977**, *60*, 2213.

43.   Yang, B.; Wang, J.; Cool, T.A.; Hansen, N.; Skeen, S.; Osborn. D.L. Absolute photoionization cross-sections of some combustion intermediates *Int. J. Mass Spectrom.* **2012**, *309*, 118-128.

44.   Holmes, J.L.; Lossing, F.P., The need for adequate thermochemical data for the interpretation of fragmentation mechanisms and ion structure assignments, *Int. J. Mass Spectrom. Ion Phys.,* **1983,** 47, 133.

45.   Wang, J.; Yang, B.; Cool, T. A.; Hansen, N.; Kasper, T. Near-Threshold Absolute Photoionization Cross-Sections of Some Reaction Intermediates in Combustion *Int. J. Mass Spectrom.* **2008**, *269*, 210– 220.

46.   Watanabe, K., Ionization potentials of some molecules, *J. Chem. Phys.,* **1957**, 26, 542.

47.   Masclet, P.; Mouvier, G. Etude par spectrometrie photoelectronique d'aldehydes et de cetones ethyleniques conjugues. *J. Elec. Spec. Rel. Phenom.* **1978,** *14* (2), 77-97.

5. Study of the Synchrotron Photoionization Oxidation Initiated by O(^{3}P) of 2-Methylfuran (2-MeF) under Low-Temperature Conditions at 550 and 650 K

Yasmin Fathi and Giovanni Meloni*

Department of Chemistry, University of San Francisco, San Francisco, California 94117 United

States

5.1 Abstract

The initiated O(^{3}P) oxidation of 2-methylfuran (2-MF) is investigated using vacuum ultraviolet (VUV) synchrotron radiation from the Advanced Light Source (ALS) of the Lawrence Berkeley National Laboratory. Reaction species are studied by multiplexed photoionization mass spectrometry at 550 and 650 K. Mass-to-charge ratios, photoionization spectra, and adiabatic ionization energies for each primary reaction species are obtained and used to characterize their identity. Using electronic structure calculations, potential energy surface scans of the different species produced throughout the oxidation are examined and presented in this paper to further validate the primary chemistry occurring. Branching fractions of primary products at the two temperatures are also provided.

*Corresponding author: gmeloni@usfca.edu

5.2 Introduction

The burning of different fuels, gasoline, diesel, and more attractive biofuels release different species in the atmosphere together with ground state oxygen atoms due to the continuous reaction of $H + O_2$.[74] Consequently, it is essential to analyze how $O(^3P)$ atoms react once these gases are released and what products are formed. This type of reaction has not been studied extensively in comparison to other combustion reactions. However, previous research[75-76] has found two possible pathways of interest: (1) hydrogen abstraction, and (2) oxygen addition pathways that follow intersystem crossing (ISC) into the singlet surface. Cvetanovic[2-76] found that the oxygen addition occurs at the less-substituted unsaturated carbon atom and the H-abstraction is a less energetically favorable pathway. The oxygen addition to an unsaturated hydrocarbon forms a triplet diradical species, which undergoes intersystem crossing (ISC) to form a singlet epoxide.[2-3] Recently, different studies have confirmed this finding.[4-7] Using multiplexed synchrotron photoionization mass spectrometry (MPIMS)[77-78] and crossed molecular breams (CMBs),[79] researchers concluded product formation occurs through the singlet epoxide species.

The interest in studying the $O(^3P)$ reaction with different compounds, which can be used as biofuels or fuel additives, arise from the paramount attention generated by the necessity of understanding and reducing the harmful effects of burning fuels. The United States Environmental Protection Agency (US EPA) reports that approximately 67% of the electricity used in every day life comes directly from burning fossil fuels.[7] Leading close behind is transportation, where almost 90% of the fuel used is petroleum based (gasoline and diesel).[7] In order to make day-to-day energy, electricity, and transportation, fossil fuels are burned in power plants and internal combustion engines.[9] This, however, releases harmful substances into the environment, such as particulate matter (PM), nitrogen oxides (NO_x), and carbon dioxide (CO_2) and hydrocarbons.[9]

Petroleum sources over the past decades have begun to diminish, further increasing the need to find alternative fuel sources. Biofuels have become progressively attractive due to their readily available resources and easy to process. Furan and alkylfurans have been identified as potential alternative biofuels.[80-181] 2,5-Dimethylfuran (2,5-DMF) is an alkylfuran that can be used as a biofuel due to some similarities with ethanol.[81-82] Previous research has found that the emission of carbon monoxide (CO) and hydrocarbons (HC) burning 2,5-DMF are higher in ethanol and lower than gasoline, increasing the need to find other alkylfurans with better combustion properties than both gasoline and ethanol.[13-14]

In general, biofuels and fuel additives have become increasingly of interest due to their high octane numbers, which indeed decrease the chance of engine knocking. In particular, alcohols have

the potential to lessen engine knocking and the emission of particle matter due to higher energy density and lower hygroscopicity.[15-83]   To this day, bioethanol has been the most commonly used biofuel due to its renewable nature. However, recent research has found that 2-methylfuran (2-MF) can be used as a novel biofuel.[81,18-84] When compared to commercial fuel and ethanol, 2-MF has a high octane number of 95 and a drop in HC emission of 61%.[81-82, 85] Similar to 2,5-DMF, it exhibits the same behavior with greater nitrous oxide emissions compared to ethanol.[13-20]

Wei et al.[11] conducted experiments on 2-MF and oxygen flames, in which they identified combustion intermediates using tunable synchrotron vacuum ultraviolet photoionization and molecular beam mass spectrometry. They found that furfural is one of the main oxidation products coming from the hydrogen abstraction pathways, which was not observed in this present investigation. Also, a study presented by Villanueva and co-workers[21] concluded that furfural is one of the combustion products reaction of 2-MF by analyzing FTIR absorption spectra in conjunction with mass spectrometry, electron capture, and solid phase microextraction on the system. They found furfural is an oxidation product yielded through the hydrogen abstraction from 2-MF and reacted with O_2.

The work presented here is focused on the combustion reaction of 2-MF at 550 and 650 K initiated through the ground state oxygen atom, $O(^3P)$, using a tunable synchrotron multiplexed photoionization mass spectrometer, which has the ability to identify isomeric species via photoionization spectra. Computations are also carried out to explain the formation of the observed products with the aid of the CBS-QB3 composite model.

5.3 Experimental

The experiments reported in this work are performed at the Chemical Dynamics Beamline of the Advanced Light Source (ALS) held at the Lawrence Berkeley National Laboratory. The ALS photoionization source produces tunable synchrotron radiation that is coupled with a multiplexed time- and energy-resolved mass spectrometer detecting and probing reaction species, intermediates, and products. Further detail about these types of experiments is discussed in previous work.[7,22-24]

The vapors of 2-MF (Sigma-Aldrich; purity $\geq$ 98%) along with He gas are collected into a gas cylinder to reach an overall 1% reaction mixture. In this work, 2-MF reacts with $O(^3P)$ at different temperatures, 550 and 650 K, and a pressure of 7 Torr. 2-MF, NO_2 (photolytic precursor), and He are introduced in the 62 cm long slow-flow reactor using calibrated mass flow controllers. The reaction species then form an effusive molecular beam through a 650 μm wide pinhole located on the side of the reactor tube and flow into a differentially vacuumed ionization region. The reaction temperature can be varied using a 18 μm thick nichrome heating tape that wraps the reactor tube.

Additionally, a feedback controlled throttle valve connects a roots pump to the reaction cell that allows the pressure to be changed and maintained throughout the different experiments. The reaction is photolytically intiated using a 4 Hz-pulsed unfocused 351 nm (XeF) excimer laser:[86]

$$NO_2 \xrightarrow{\text{351 nm}} O(^3P) + NO$$

The concentration of NO_2 used throughout these experiments are calculated to be 5.35 x 10^{16} molecules cm^{-3} at 550 K and 3.47 x 10^{16} molecules cm^{-3} at 650 K. Along with the concentration values calculated from the experiment and the previous reported quantum yield of $O(^3P)$, 1.00^{25}, at 351 nm as well as the absorption cross-section, 4.62 x 10^{-19} cm^{2},[26] the concentrations of $O(^3P)$ is 8.03 x 10^{13} molecules cm^{-3} at 550 K and 5.21 x 10^{13} molecules cm^{-3} at 650 K.

Once the reactions species are ionized, they are accelerated, collimated, focused, and detected via a 50 kHz pulse orthogonal acceleration time-of-flight mass spectrometer with a current mass resolution of approximately 1,600.[86]

The data analysis begins with taking two-dimensional slices of the resulting three-dimensional data block consisting of the ion signal being a function of photon energy (eV), time (ms), and mass-to-charge (m/z) ratio. The data is background subtracted for the pre-photolysis signal and normalized at individual photon energies using a calibrated photodiode. A negative ion signal is expected for depleting species (reactants) and a positive ion signal for formation of products. Primary products are identified through their kinetic time plots (ion signal (arb. units) vs. kinetic time (ms)). An example is provided in Figure 1a for the primary product m/z 42. Secondary chemistry is eliminated through analysis when the initial kinetic rise is slower than the inverse kinetic time trace of the depleting reactant. Figure 1b provides an example of a secondary product at m/z 58.[40] The identified primary species are then characterized through their photoionization (PI) spectra and adiabatic ionization energies (AIE). The AIE's are determined by taking the linear extrapolation of the initial onset of the experimental PI spectrum.[23] The photon energy step size in this work is 25 meV, therefore, with the possible presence of hot bands and energy resolution, the estimated AIE uncertaint is 0.05 eV.[23]

The photoionization spectra are obtained through a vertical slice of the two- dimensional image m/z vs. photon energy (eV). In order to obtain an accurate PI spectrum and minimize the presence of signal due to any possible secondary products, the data is integrated in the time range of 0-30 ms at 550 K and 0-10 ms at 650 K. Identification begins through the "fitting" of literature PI spectra when available or the integration of a computed simulated Franck-Condon photoelectron spectrum.

In addition to characterizing and identifying the primary chemistry occurring throughout this oxidation, it is essential to determine the thermodynamic feasibility of the pathways to form these species (their exothermicity). Product quantification is also achieved calculating branching fractions, which represent the quotient of the concentration of the products with respect to the concentration of the reactant. Equation 1 below shows how branching fractions are obtained experimentally:

$$\frac{C_P}{C_R} = \frac{S_P \sigma_R \delta_R}{S_R \sigma_P \delta_R} = \frac{S_P \sigma_R (m_R)^{0.67}}{S_R \sigma_P (m_P)^{0.67}} = \frac{S_P \sigma_R}{S_R \sigma_P} * MDF \tag{1}$$

where C_P is the concentration of the product, C_R the concentration of the reactant (measured as change in the initial reactant concentration), S_P and S_R are the signal of the product and reactant, respectively, at a specified photon energy, σ_P and σ_R are the photoionization cross-section of the product and reactant, respectively, at a specified photon energy, and the mass discrimination factor (MDF) is the quotient of reactant and product mass to the power of 0.67,[27] which takes into account the mass-dependent response of the detector.

For the branching fraction determination, the ion signals and photoionization cross-sections are used at 11 eV. In addition, the ion signal is averaged for 250 laser shots at each energy step. The overall branching fractions uncertainties are calculated using the propagation of errors of the quantities in equation 1. Specifically, the uncertainties of the photoionization cross sections and the mass discrimination factor are from the literature, whereas the uncertainty of each ion signal is estimated by taking the difference between the measured upper value at 11 eV of a specific species and its reference (literature or simulation) spectrum used in the assignment. The same procedure is applied using the lower ion signal value at 11 eV and the average of the two differences is used.

5.4 Computational

The products identified in this work are optimized through electronic structure calculations utilizing the complete basis set CBS-QB3[28-29] composite model with the Gaussian09[30] program. The CBS-QB3 is used due to its high energetics accuracy with a reported mean average deviation of 4-5 kJ/mol.[28-29] Within this composite method, the molecular parameters, bond lengths and angles, harmonic vibrational frequencies, force constants, and rotational constants are optimized at the B3LYP density functional level. The computational methods of this work are first used for further identification of primary products in calculating the AIE of particular molecules. The CBS-QB3 zero-point vibrational corrected total electronic energy (E_0) for the neutral and cation ground state are used to compute the adiabatic ionization energies (AIE) as seen in equation 2:

$$AIE = E_{0(cation)} - E_{0(neutral)} \tag{2}$$

117

The identification of primary products occurs when the AIE and the overall photoionization spectrum are in good agreement with the literature values. In some instances, however, PI spectra are unavailable and computational methods are used to run a spectral simulation. This is achieved using the optimized molecular parameters to simulate a photoelectron spectrum within the Franck-Condon (FC) and Franck-Condon-Herzberg-Teller[31-33] (FCHT) approximations through the Gaussian 09 program. In this methodology the vibrational normal modes are expressed using the Duschinsky[31] rotation matrix. The FC overlap integrals are calculated using recursive formulae developed by Ruhoff,[35] based on Lermé[33] and Sharp-Rosenstock[54] methods for the overlap integrals calculations.

Then, mechanisms to prove that primary products are formed from the oxygen addition pathway are computed and, based on the pathway exothermicity, they are determined to be thermodynamically feasible. PES scans using the B3LYP/6-31G(d) level of theory and basis set are carried out as a function of bond lengths and bond angles, to visualize whether transition state barriers occur at different steps of each pathway.[52] Each transition state barrier and minimum are recalculated using the CBS-QB3 and the obtained ZPE corrected total electronic energies are used. In order to further verify the forward and reverse steps of the different potential energy surface scans as well as the local minima and saddle points, intrinsic reaction coordinate (IRC) calculations are also performed.[37]

5.5 Results

The initiated oxidation of 2-MF with O(^{3}P) has two main pathways, oxygen addition to the unsaturated carbons as well as hydrogen abstraction. In this work all the primary products are formed from the singlet epoxide species that form from the triplet diradicals that occur through the oxygen addition and a secondary product is formed from the initial hydrogen abstraction. As visualized in Scheme 1, there are four different possible triplet diradicals. The heat of formation computed and presented in this work are calculated at 0 K. They undergo intersystem crossing to yield the singlet epoxide species at -315 kJ/mol (E) and -317 kJ/mol (F). The primary products observed in this work are only presented from epoxide E and F. Triplet diradical A is the most favorable with an enthalpy of -138 kJ/mol and triplet diradical D falls close behind at -134 kJ/mol. The radicals B and C are less favorable with a heat of reaction of -57 kJ/mol and -54 kJ/mol, respectively.
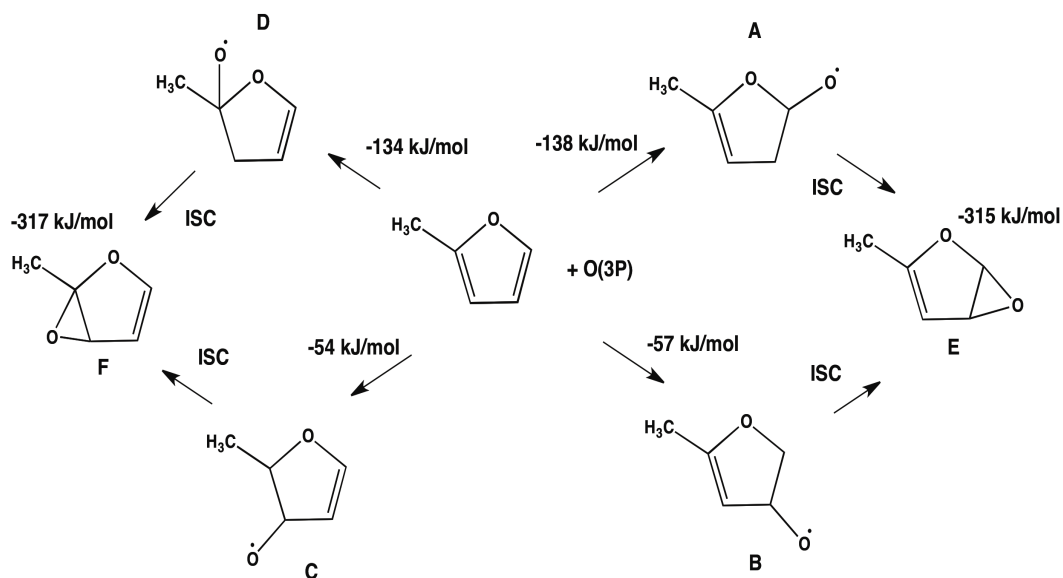
Scheme 1. The four possible triplet diradicals forming from the oxygen addition pathway are presented along with the singlet epoxide species forming.
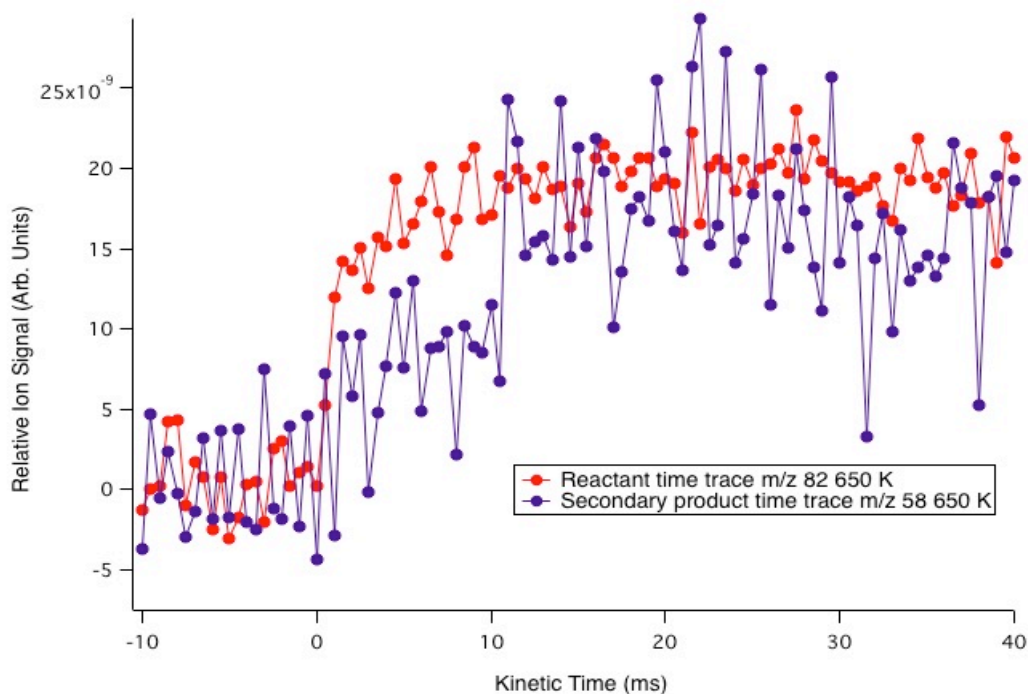
5.5.1 Product Identification

In the 2-MF + O(^{3}P) reaction the same products are observed at both temperatures. They are m/z 30, 42, and 70. As mentioned above, the characterization of primary products is completed through the observation of kinetic time plots (Figure 1a and 1b).

a)
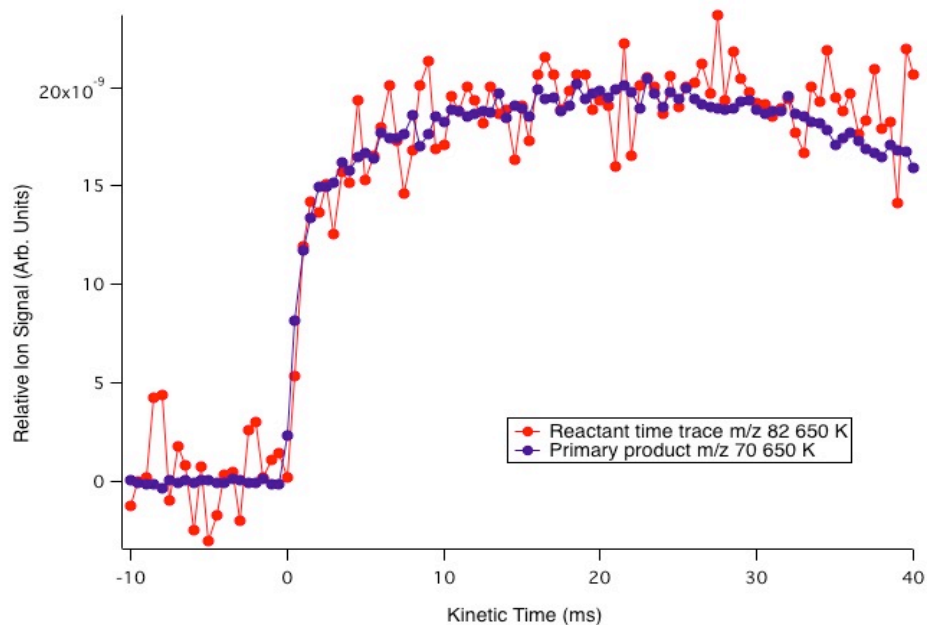
b)

Figure 1. a) Kinetic time trace of primary product, m/z 70, (full blue circles) superimposed onto the inverse of the temporal plot of the parent (red full circles); b) kinetic time trace of secondary product, m/z 58, (full blue circles) superimposed onto reverse reactant time trace (red full circles).

From the photolysis of NO_2 to generate $O(^3P)$, NO is produced as well and it shows at m/z 30. However, at m/z 30 formaldehyde is also formed. Its literature spectrum[38] summed to the reference PI spectrum of NO^5 fits very well the experimental data (Figure 2a and 2b).

a)
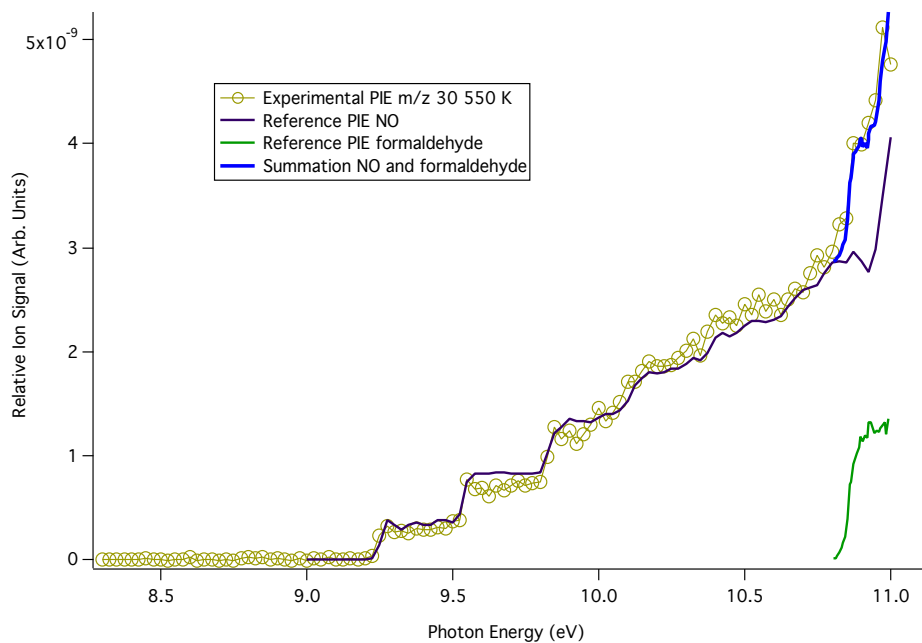
b)
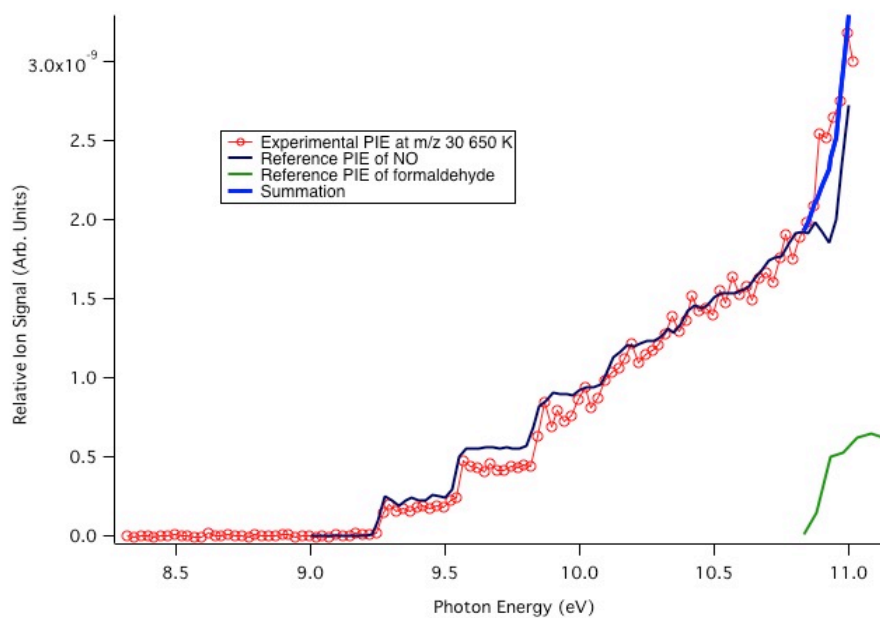
Figure 2. The reference PI spectrum of NO in purple and formaldehyde in green superimposed onto the m/z 30 experimental PI spectrum (a) at 550 K (yellow open circles) and (b) and 650 K (red open circles); the summation of the two literature spectra is in blue.

Signal at m/z 42 is assigned to propene and cyclopropane. m/z 42 kinetic time trace is presented in Figure 3. The literature PI spectrum of the Person and Nicole[39] of propene fits well the initial part of the experimental PI spectrum at m/z 42 at both 550 and 650 K (Figure 4a and 4b). The ionization onset of 9.70 ± 0.05 eV matches the reference AIE of 9.74 ± 0.01 eV.[39] At higher photon energies, the experimental spectrum is matched by the literature spectrum of cyclopropane[41] with an ionization energy of 9.90 ± 0.05 eV. The summation of both literature spectra fits well the overall shape of the experimental spectrum.
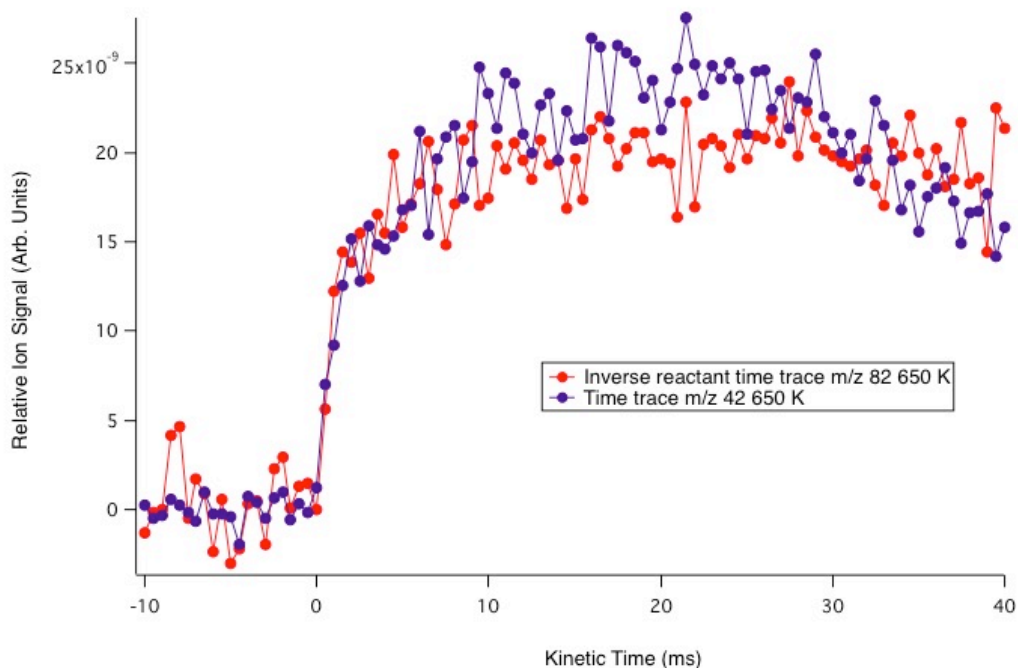
Figure 3. Kinetic time trace of m/z 42 (full blue circles) superimposed onto the inverse of the temporal plot of the parent (red full circles) at 650 K.

a)
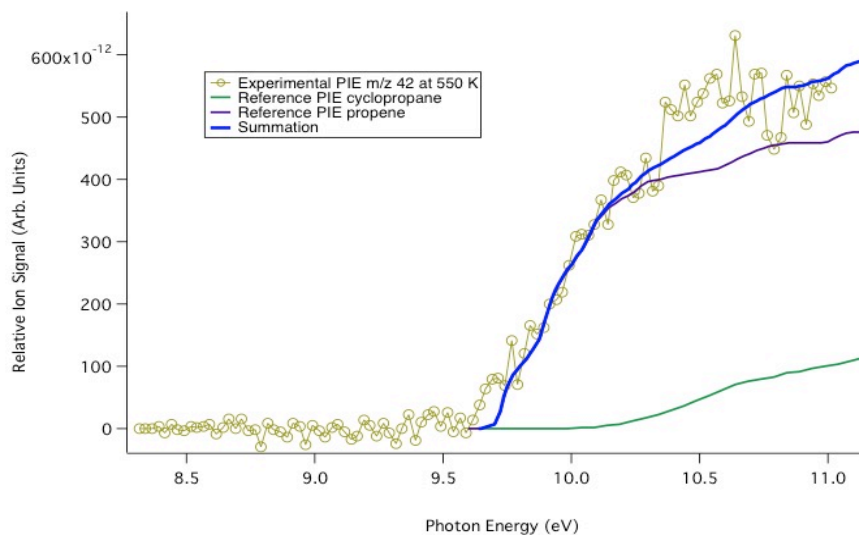
b)
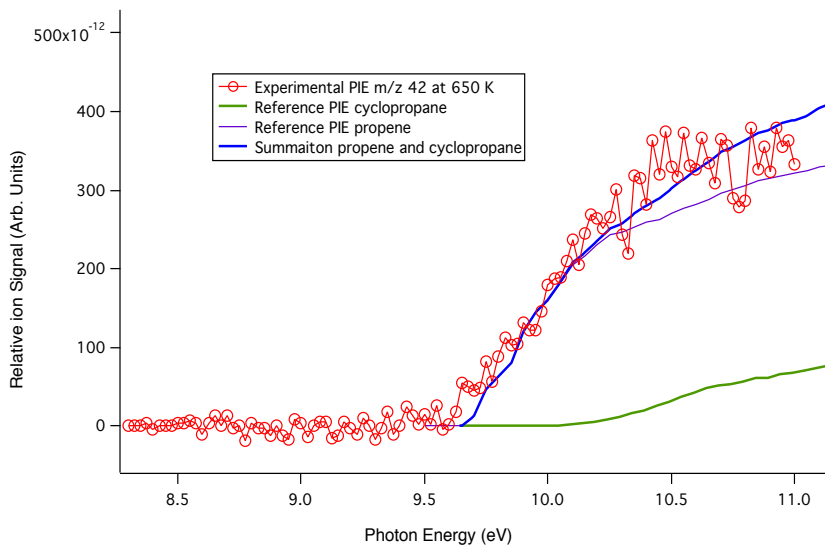
Figure 4. a) The literature PI spectra of propene and cyclopropane superimposed onto the experimental PI spectrum of m/z 42 at (a) 550 K and (b) 650 K.

Two species are identified forming at m/z 70. The summation of the reference PI spectrum of methyl vinyl ketone[40] and 2-butenal[40] is in very good agreement with the experimental PI spectrum at both temperatures (Figure 5a and 5b). The m/z 70 signal onset matches methyl vinyl ketone at 9.64

123

eV[40] and at higher photon energy 2-butenal spectrum, which has a literature AIE of 9.73 ± 0.01 eV,[41] is in good agreement with the experimental data.

a)
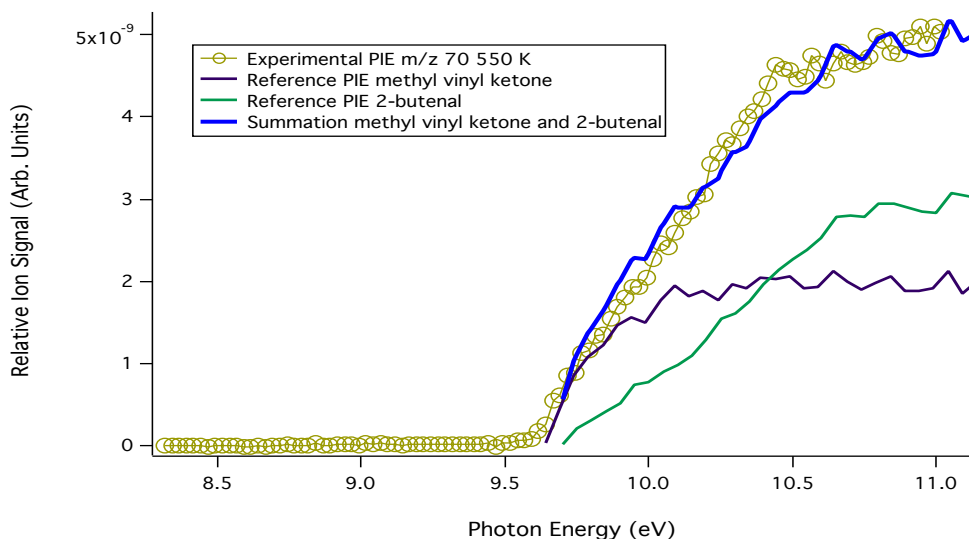
b)
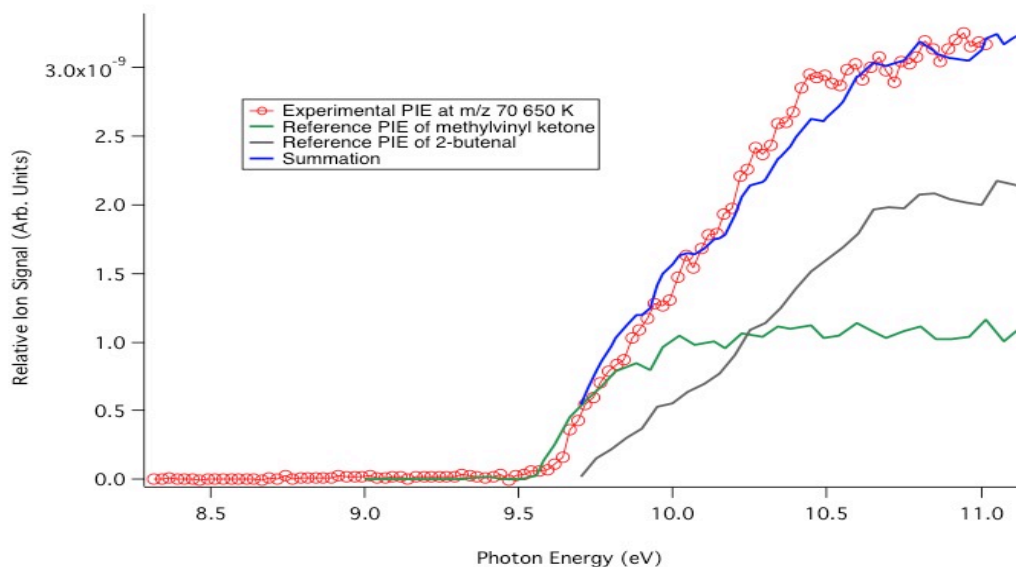
Figure 5. The summation (blue line) of the reference PI spectra of methyl vinyl ketone (green line) and 2-butenal (gray line) is fit to the experimental PI spectrum at a) 550 K (yellow open circles), and b) 650 K (red open circles).

As mentioned before, previous studies have found that furfural is a primary oxidation product forming from the hydrogen abstraction of 2-MF. This is observed in this study as well, however it is not a primary product. The time trace of m/z 96 superimposed onto the inverse of the reactant is a bit

slower indicating a slower formation (Figure 6a and 6b). A reference PIE of furfural is fit to the experimental PIE at m/z 96 at both temperatures. Additionally, the reported AIE of furfural is 9.21 $\pm$ 0.01 eV[42] which fits well with the experimental AIE of 9.20 $\pm$ 0.05 eV. Only the onset of this signal is observed experimentally at both temperatures (Figure 7a and 7b).

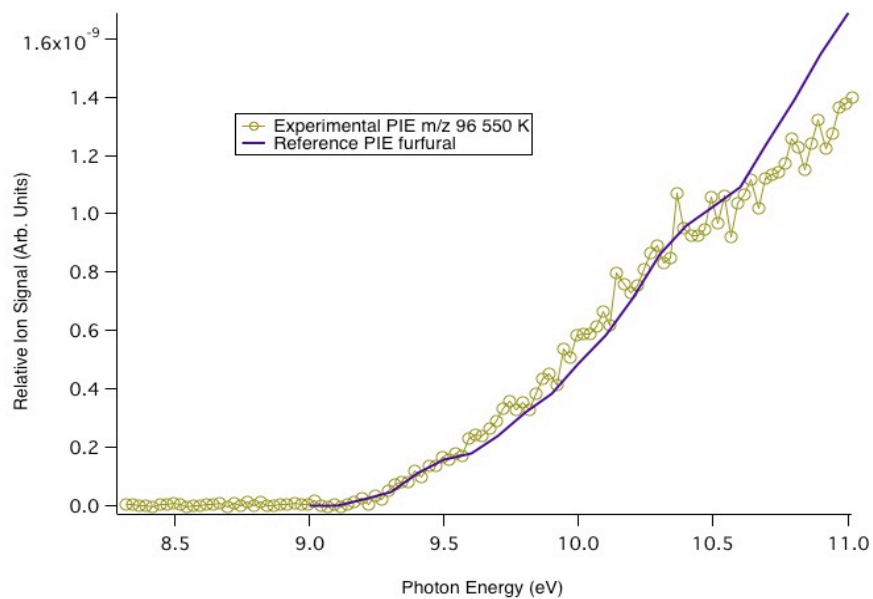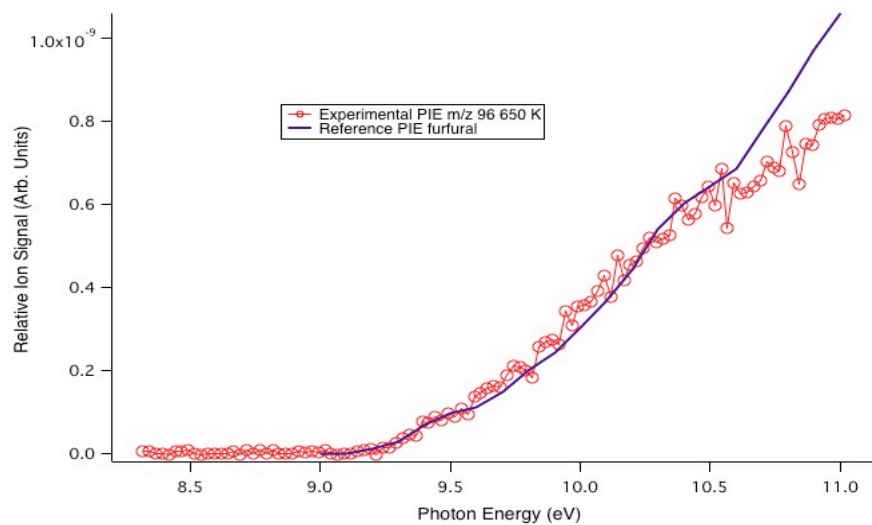**a)**
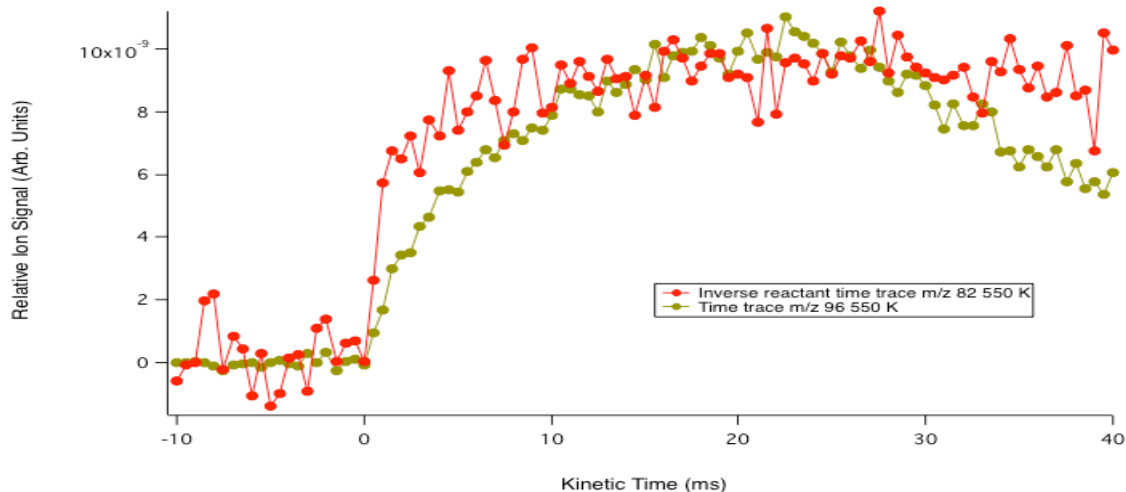
b)
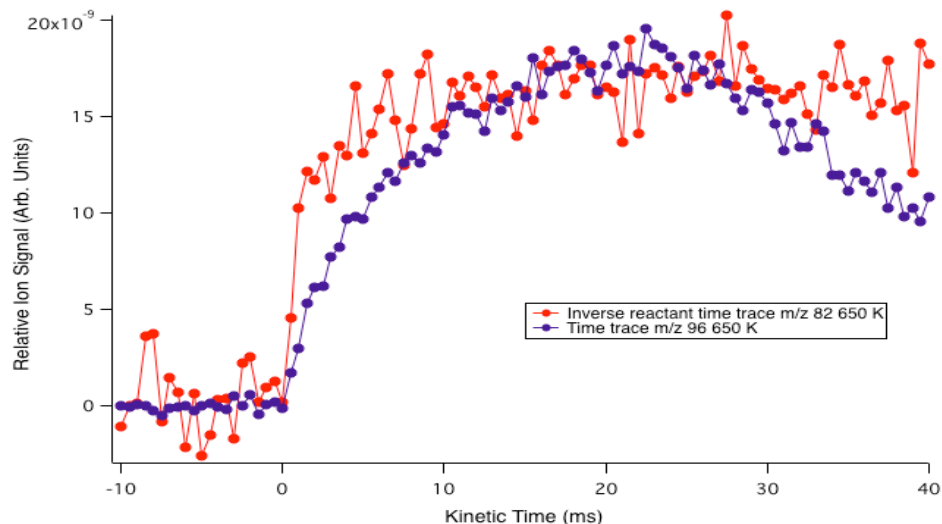
Figure 6. a) Kinetic time trace of m/z 96 (full yellow circles) superimposed onto the inverse of the temporal plot of the parent (red full circles) at 550 K. b) Kinetic time trace of m/z 96 (full purple circles) superimposed onto the inverse of the temporal plot of the parent (red full circles) at 650 K.

a)

b)

Figure 7. a) A Franck-Condon PI simulation spectrum of furfural (purple line) fit to the experimental PI spectrum onset at m/z 96 at a) 550 K (yellow open circles), and b) 650 K (red open circles).

5.5.2 Thermodynamic Mechanism for Primary Products

The O(^{3}P) addition pathway in this work yields the observed primary products, no contribution was observed from the hydrogen abstraction pathways. The hydrogen abstraction radical reacting with O$_2$ forms secondary chemistry. A study performed on the chemical kinetic of the hydrogen abstraction from allylic sites by molecular absorption reported the activation barrier to the hydrogen abstraction to be 167 kJ/mol.[43] The primary products in this work form from two different singlet epoxide species thermodynamically feasible (E and F in Scheme 1). The initial reaction of O(^{3}P) with 2-MF forming triplet diradicals is used as the reference point (the zero energy) for the energetic calculations of the primary characterized species. Any molecular species or energetic barrier above the red line in the potential energy surface diagrams is thermodynamically or kinetically, respectively, unfavorable.

As seen in Scheme 1, the oxidation reaction of 2-MF starts with four possible different energetically favorable triplet diradicals, from which two-singlet epoxide species forms. The most energetically favorable triplet diradical A and the diradical B both yield the epoxide E, which has an unbound cation and dissociatively ionizes, therefore, is not observed in this work. This epoxide is responsible for the formation of formaldehyde, cyclopropane, methyl vinyl ketone, and 2-butenal. From epoxide E to E1, an activation barrier of 249 kJ/mol occurs through the hydrogen transfer from the alpha to the beta carbon forming a radical species with a heat of reaction of 118 kJ/mol. Methyl vinyl ketone forms from the loss of CO. This formation consists of a transition state of 20 kJ/mol and an enthalpy of -204 kJ/mol (Figure 8).
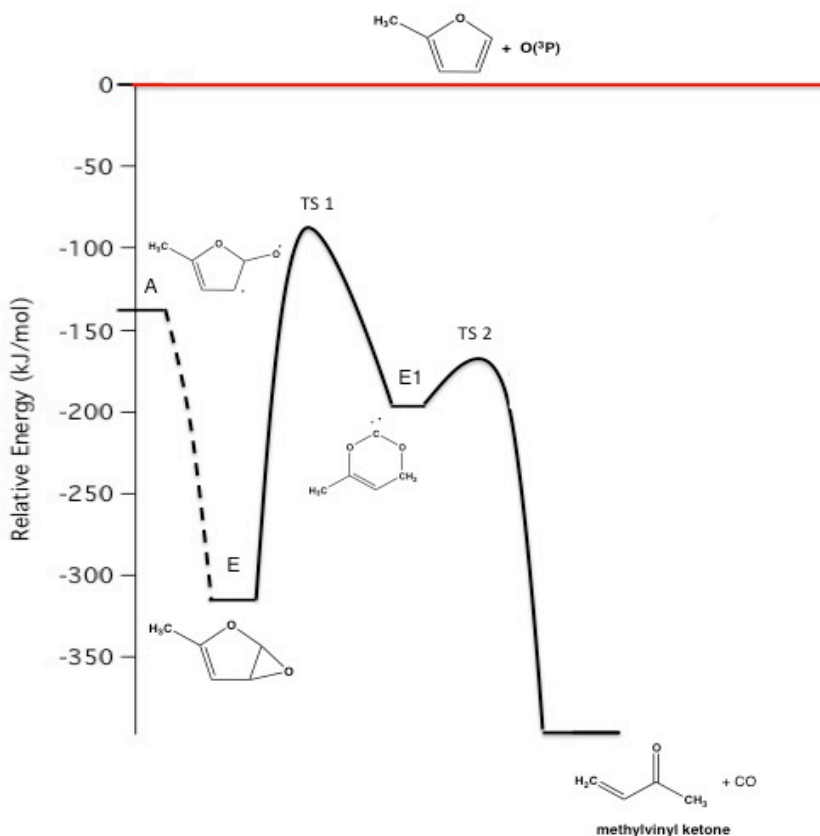
Figure 8. A potential energy surface diagram is displayed representing the formation of methyl vinyl ketone from epoxide E. The dashed line from the triplet diradical A represents the intersystem crossing to the singlet surface.

The formation of 2-butenal, propene, and cyclopropane are represented in Figure 9. The epoxide E breaks to form 4-ketopentenal with a heat of reaction of -68 kJ/mol, associated with an activation barrier of 63 kJ/mol. This species has an unbound cation and, therefore, it is not observed experimentally throughout this reaction. With a transition state barrier of 294 kJ/mol, 4-ketopentenal forms E2* through the hydrogen transfer of the methyl group to the γC forming a species also not observed throughout this experiment because it has an unbound cation. The heat of reaction of this hydrogen transfer is 106 kJ/mol. With an activation barrier of 146 kJ/mol, CO cleaves of forming prop-2-enal at 86 kJ/mol. Prop-2-enal is not observed at m/z 70 in this work due to poor Franck-Condon factors that occur from geometrical differences between its neutral and cation state. It forms 2-butenal with a barrier of 299 kJ/mol through a hydrogen transfer. The associated heat of reaction forming 2-butenal is of 1 kJ/mol. Prop-2-enal can also lose CO to form cyclopropane and propene. The associated transition state barrier of TS1 is 267 kJ/mol with an enthalpy of 19 kJ/mol for cyclopropane Figure 9). Propene is formed with a heat of reaction and a barrier of 192 kJ/mol and -18

kJ/mol, respectively. From prop-2-enal a hydrogen transfer to the ketocarbon with a barrier of 192 kJ/mol cleaves the C-C bond forming formaldehyde with a heat of reaction of 232 kJ/mol (Figure 10).
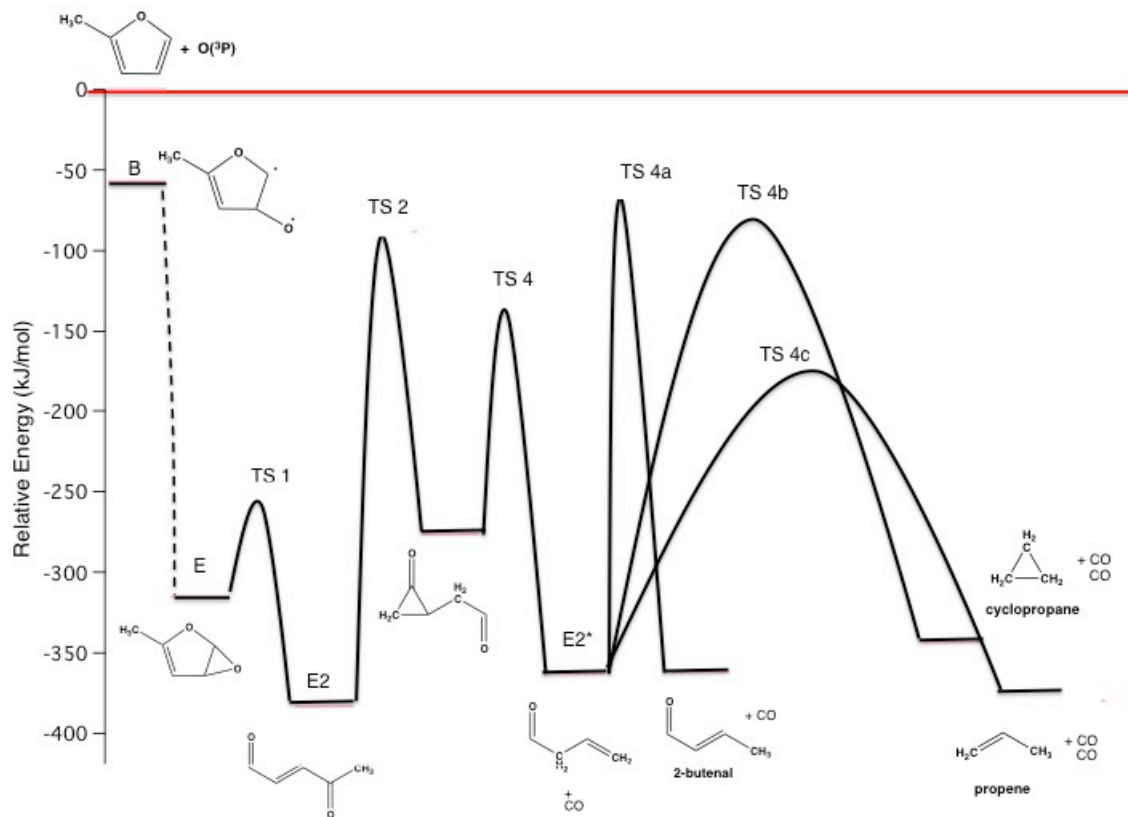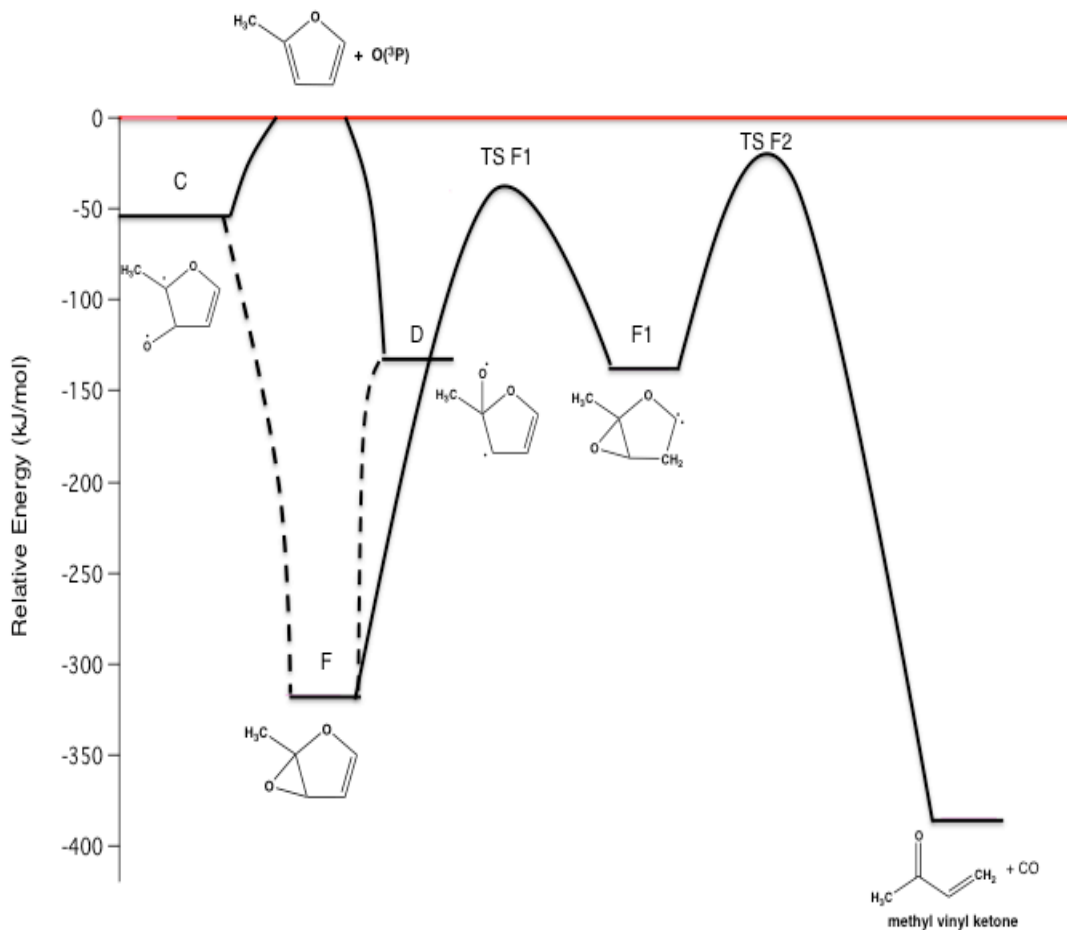

Figure 9. The energy diagram presents the formation of 2-butenal from epoxide E, which further decomposes to forming cycloporpane and propene. The dashed line from the triplet diradical B represents the intersystem crossing to the singlet surface.
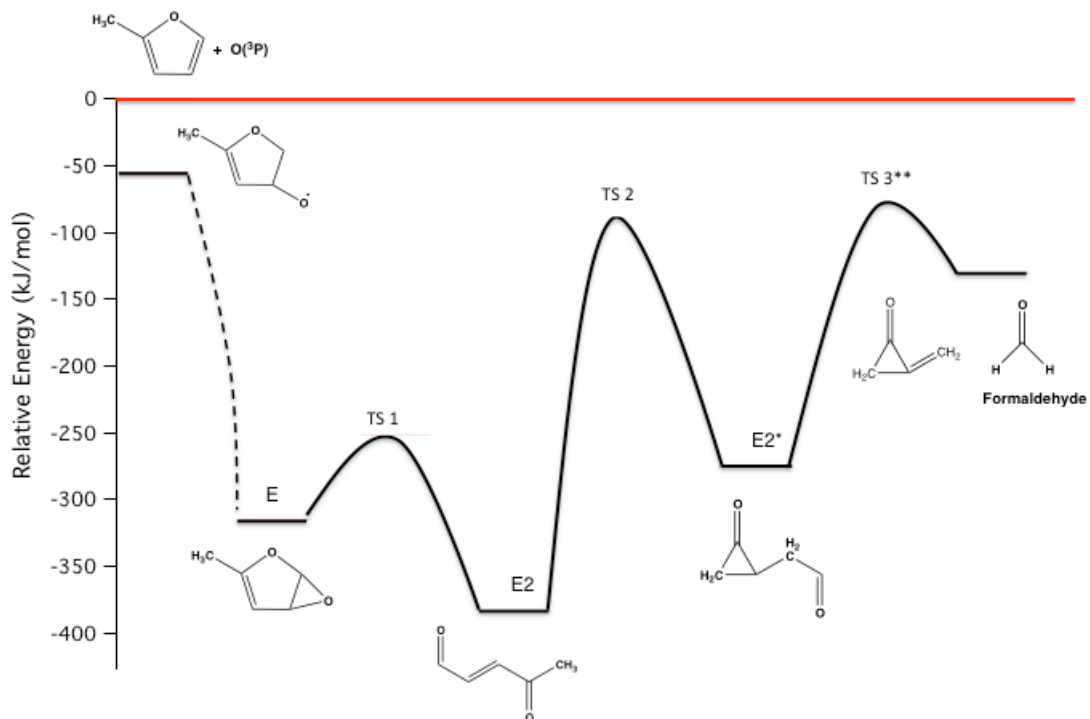
Figure 10. The energy diagram presents the formation of formaldehyde from epoxide E. The dashed line from the triplet diradical B represents the intersystem crossing to the singlet surface.

Methyl vinyl ketone is also formed from epoxide F observed in Figure 9. As mentioned before epoxide F, heat of reaction -317 kJ/mol, forms from the triplet diradical D (-134 kJ/mol) and C (-54 kJ/mol). With a transition state barrier of 289 kJ/mol, a hydrogen transfer forms a radical species, F1, at an enthalpy of 179 kJ/mol. Methyl vinyl ketone forms through a CO cleavage with transition state barrier of 127 kJ/mol. The formation of this product has an enthalpy of 251 kJ/mol (Figure 11).

Figure 11. The energy diagram presents the formation of methyl vinyl ketone from epoxide F forming from triplet diradical C and D.

5.5.3 Branching Fractions

The primary products in this work are identified using kinetic time trace and characterized through their PI spectra. It is essential to know the concentration of the reactant and how much of each product is actually formed to compute the branching fractions. Using equation 1 presented in the computational section, the branching fractions of each product is presented in Table 1 for all three temperatures. The photoionization signal and photoionization cross-section are used at 11 eV for each measurement.

Table 1. Branching fractions of the primary products observed throughout this oxidation at 550 and 650 K.

Signal	Identified species	550 K	650 K
m/z 30	Formaldehyde	39.3 ± 12.9	27.8 ± 9.7
m/z 42	Cyclopropane	1.05 ± 0.5	0.87 ± 0.3
m/z 42	Propene	9.0 ± 2.9	26.3 ± 9.0
m/z 70	2-Butenal	16.6 ± 6.3	32.9 ± 12.3
m/z 70	Methyl vinyl ketone	29.2 ± 10.5	13.4 ± 4.9

The largest contribution is given from formaldehyde at 550 K, 39.3 ± 12.9 % where at 650 K it contributes a little less than 27.8 ± 9.7 %. 2-Butenal's contribution increases with the increase in temperature from 16.6 ± 6.3 % at 550 K to 32.9 ± 12.3 % at 650 K. Interestingly, methyl vinyl ketone follows the opposite path, decreasing its contribution with the increase in temperature from 29.2 ± 10.5 % at 550 K to 13.4 ± 4.9 % at 650 K. This means that m/z 70 signal consists of a higher portion of 2-butenal as the temperature rises. A small contribution of cyclopropane is given at 550 K as 1.05 ± 0.5 % and at 650 K is 0.87 ± 0.3%. Propene increases from 9.0 ± 2.9 % at 550 K to 26.3 ± 9.0 % at 650 K.

5.6 Conclusions

This work used the synchrotron radiation at the Lawrence Berkeley National Laboratory to investigate the $O(^3P)$ initiated oxidation of 2-MF at 550 and 650 K. The primary products of this work are identified using time traces and characterized through reference photoionization spectra. The oxygen addition pathway is favored in this reaction forming four triplet diradicals that undergo intersystem crossing into singlet epoxide species that lead to the formation of m/z 30, 42, and 70. Using the CBS-QB3 composite method, theoretical calculations are performed to determine energetically favorable pathways leading to the formation of these primary products. Their branching fractions contributed 95.2 ± 18.0 % at 550 K and contributed 101.3 ± 18.7 % at 650 K. At 550 K, formaldehyde contributes for 39.3 ± 12.95 %, cyclopropane and propene for 1.05 ± 0.5 % and 9.0 ± 2.9 %, respectively, and methyl vinyl ketone and 2-butenal for 29.2 ± 10.5 % and 16.6 ± 6.3 %, respectively. At 650 K, formaldehyde contribution decreases to 27.8 ± 9.7 %, cyclopropane is almost identical (0.87 ± 0.3 %), propene becomes three times larger (26.3 ± 9.0 %), methyl vinyl ketone decreases to 13.4 ± 4.9 %, and 2-butenal contribution doubles to 32.9 ± 12.3 %.

5.7 Acknowledgements

5.8 References

1. Miller, J. A.; Kee, R. J.; Westbrook, C. K., Chemical Kinetics and Combustion Modeling. *Annu. Rev. Phys. Chem.* **1990,** *41*, 345-387.
2. Cvetanovic, R. J. Biradical intermediate in the addition of the ground state oxygen atoms, O(3P), to olefins. *J. Phys. Chem. 74* (13), 2730– 2732.
3. Cvetanovic, R. J.; Singletoon, D. L. Evaluated Chemical Kinetics Data for the Reactions of Atomic Oxygen O(3P) with Unsaturated Hydrocarbons. *J. Phys. Chem. Ref. Data* **1987,** *1*, 261-326.
4. Taatjes, C. A.; Osborn, D. L.; Selby, T. M.; Meloni, G.; Trevitt, A. J.; Epifanovsky, E.; Krylov, A. I.; Sirjean, B.; Dames, E.; Wang, H. Products of the benzene + O(3P) reaction. *J. Phys. Chem. A* **2010,** *114* (9), 3355-70.
5. Savee, J. D.; Welz, O.; Taatjes, C. A.; Osborn, D. L. New mechanistic insights to the O(3P) + propene reaction from multiplexed photoionization mass spectrometry. *Phys. Chem. Chem. Phys.: PCCP* **2012,** *14* (30), 10410-23.
6. Ng, M. Y.; Nelson, J.; Taatjes, C.A.; Osborn, D. L.; Meloni, G. Sycnhrotron Photoinization Study of Mesitylene Oxidation Initiated by Reaction with Cl(2P) or O(3P) Radicals. *J. Phys. Chem.* **2014,** *118*, 3735-3748.
7. Fathi, Y.; Price, C.; Meloni, G. Low-Temperature Synchrotron Photoionization Study of 2-Methyl-3-buten-2-ol (MBO) Oxidation Initiated by O(3P) Atoms in the 298-65 K Range. *J. Phys. Chem. A* **2017,** *121* (15), 2963-2950.
8. Leonori, F.; Occhiogrosso, A.; Balucani, N.; Bucci, A.; Petrucci, R.; Casavecchia, P. Crossed Molecular Beam Dynamics Studies of the O(3P) + Allene Reaction: Primary Products, Branching Rations, and Dominant Role of Intersystem Crossing. *J. Phys. Chem.* **2012,** *3*, 75-80.
9. Agency, E. P. Sources of Greenhouse Gas Emissions. http://www.epa.gov/ghgemissions/sources-greenhouse-gas-emissions.
10. EPA Motor Vehicle-Related Air Toxis Study.
11. Wei, L.; Li, Z.; Tong, L.; Wang, Z.; Jin, H.; Yao, M.; Zheng, Z.; Wang, C.; Xu, H. Primary combustion intermediates in lean and rich low-pressure premixed laminar 2-methylfuran/oxygen/argon flames. *Energy Fuels* **2012,** 26, 6651-6660.
12. Eldeep, M. A.; Akih-Kumgeh, B. Reactivity Trends in Furan and Alkyl Furan Combustion. *Energy Fuels* **2014,** 28 (10), 6618-6626.
13. Somers, K. P. et al. A high temperature and atmospheric pressure experimental and detailed chemical kinetic modeling study of 2-methylfuran and oxidation. *Proc. Combust. Inst.* **2013,** *34*, 225-232.
14. Dutta, S.; Mascal, M. Novel Pathways to 2,5-Dimethylfuran via Biomass-Derived 5-(Chloromethyl)furfural. *Chem. Sus. Chem.* **2014,** 7, 3028-3030.
15. Atsumi, S. Hanai, T.; Liao, J. C. Non-fermentative pathways for synthesis of branched-chain higher alcohols as biofuels. *Nature* **2008,** *451* (7174), 86-89;
16. Demirbas, A. Progress and recent trends in biofuels. *Prog. Energy Combus. Sci.* **2007,** *33*, 1-18.
17. Agarwal, A. K. Biofuels (alcohols and biodiesel) applications as fuels for internal combustion energies. *Prog. Energy Combus. Sci.* **2008,** 33 (3), 233-271.
18. Davis, A. C.; Sarathy, S. M. Computational study of the combustion and atmospheric decomposition of 2-methylfuran. *J. Phys. Chem.* **2013,** 117, 7670-7685.
19. Ma, X.; Jiang, H.; Xu, H.; Ding, H.; Shuai, S. Laminar burning characteristics of 2-methylfuran and isooctane blend. *Fuel* **2013,** *116*, 281-291.
20. Wang, C. Combustion characteristics and emissions of 2-methylfuran compared to 2,5-dimethylfuran, gasoline and ethanol in a DISI engine. *Fuel* **2012,** *103*, 200- 211.
21. Villanueva, F.; Cabanas, B.; Monedero, E.; Salgado, S.; Bejan, I.; Martin, P. Atmospheric degradation of alkylfurans with chlorine atoms: Product and mechanistic study. *Atoms. Environ.* **2009,** *43*, 2804-2813.

22. Ray, A. W.; Taatjes, C. A.; Welz, O.; Osborn, D. L.; Meloni, G. Synchrotron Photoionization Measurements of OH-Intitiated Cyclohexene Oxidation: Ring- Preserving Products in OH + Cyclohexene and Hydroxycyclohexyl + O2 Reaction. *J. Phys. Chem.* **2012,** *116* (25), 6720-6730.
23. Ng, M. Y.; Bryan, B. M.; Nelson, J.; Meloni, G. Study of tert-Amyl Methyl Ether Low Temperature Oxidation Using Synchrotron Photoionization Mass Spectrometry. *J. Phys. Chem. A,* **2015,** *119* (32), 8667-82.
24. Osborn, D. L. et al. The multiplexed chemical kinetic photoionization mass spectrometer: A new approach to isomer-resolved chemical kinetics. *Rev. Sci. Instrum.* **2008**, *79* (10) 104103
25. Troe, J. Primary Quantum Yields of NO2 Photolysis at λ ≤ 398 nm Smaller Than Unity? Z. *Phys. Chem*. **2000,** 214, 573-581.
26. Vandaele, A. C. Hermans, C.; Simon, P. C.; Carleer, M.; Colin, R.; Fally, S.; Merienne, M. F.; Jenouvrier, A.; Coquart, B., Measurements of the NO2 Absorption Cross-Section from 42000 cm-1 to 10000 cm-1 (238-1000nm) at 220 K and 294 K. *J. Quant. Spec. Ra.* **1998,** 59, 171-184.
27. Savee, J. D.; Soorkia, S.; Welz, O.; Selby, T. M.; Taatjes, C. A.; Osborn, D. L. Absolute Photionization Cross-Section of the Propargyl Radical. *J. Chem. Phys*. **2012,** 136 (13), 134307/1-134307/10.
28. Montgomery Jr., J. A.; Frisch, M. J.; Ochterski, J. W.; Petersson, G. A. A complete basis set model chemistry. VI. Use of density functional geometries and frequencies. *J. Chem. Phys.* **1999,** *110* (6), 2822-2827.
29. Montgomery Jr., J. A.; Frisch, M. J.; Ochterski, J. W.; Petersson, G. A., A complete basis set model chemistry. VII. Use of the minimum population localization method. *J. Chem. Phys.* **2000,** *112* (15), 6532-6542.
30. Frisch, M. J. et al, Gaussian 09. *Gaussian Inc. Wallingford, CT* **2009**.
31. Duschinsky, F. Physicochim. *URSS* **1937,** *7* (551-566).
32. Sharp, T. E.; Rosenstock, H. M. Franck-Condon Factors for Polyatomic Molecules. *J. Chem. Phys.* **1964,** *41*, 3453-3463.
33. Lerme, J. Iterative Methods to Compute One- and Two-Dimensional Franck-Condon Factors. Tests of Accuracy and Application to Study Indirect Molecular Transitions. *Chem. Phys.* **1990,** *145*, 67-88.
34. Fukui, K. The Path of Chemical Reactions - the IRC Approach. *Acc. Chem. Res.* **1981,** *14*, 363-36
35. Ruhoff, P. T. Recursion relations for multi-dimensional Franck-Condon overlap integrals. *Chem. Phys* **1994**, *186* (2-3) 355-374
36. Tirado-Rives, J.; Jorgensen, W. L. Performance of B3LYP Density Functional Methods for a Large Set of Organic Molecules. *J. Chem. Theory Comp.* 2008, 4 (2) 297-306
37. Fukui, K. The Path of Chemical Reactions - the IRC Approach. *Acc. Chem. Res.* **1981,** 14, 363-368.
38. Guyon, P. A.; Chupka, W. A.; Berkowitz, J., Photoionization mass spectrometric study of formaldehyde H2CO, HDCO, and D2CO*. *J. Chem. Phys.* **1976,** 64 (1419-1436).
39. Pearson, J. C. N., P. P., Isotope Effects in the Photoionization Yields and the Absorption Cross Sections for Acetylene, Propyne, and Propene. *J. Chem. Phys*. **1970,** 53, 1767-1774.
40. Yang, B. W., J.; Cool, T. A.; Hansen, N.; Skeen, S.; Osborn, D. L., Absolute photoionization cross-sections of some combustion intermediates. *Int. J. Mass. Spectrom.* **2012,** *309*, 118-128.
41. Watanabe, K., Nakayama, T.; Mottl, J. Ionization potentials of some molecules. *J. Quant. Spectrosc. Rad. Trans.* **1962,** *2*, 369.
42. Smith, A. R. Absolute Photoionization Cross Sections of Furanic Fuels: 2-Ethylfuran, 2-Acetylfuran and Furfural. *J. Mass. Spec.* **2015** *50* (1) 1206-1213
43. Zhou, C-W.; Simmie, J. M.; Somer, K. P. Goldsmith, C. F.; Curran, H. J. Chemical Knetics of Hydrogen Atom Abstraction from Allylic Sites by O; Implication for Combustion Modeling and Simulation. *J. Phys. Chem. A*. **2017** *121* (9) 1890-1899

6. Photoionization and Photodissocation of Xylyl (Methylbenzyl) Bromide Radicals using VUV Synchrotron Radiation

Yasmin Fathi,[§] Patrick Hemberger,[⌘] and Giovanni Meloni[§,*]

[§]Department of Chemistry, University of San Francisco, San Francisco, CA 94117 United States

[⌘]Laboratory for Femtochemistry and Synchrotron Radiation, Paul Scherrer Institute, Villigen 5232, Switzerland

6.1 Abstract

The dissociative photoionization of energy-selected xylyl (methylbenzyl) bromide isomers is investigated by imaging (iPEPICO) and double imaging (i²PEPICO) photoelectron coincidence spectroscopy using the vacuum ultraviolet (VUV) synchrotron radiation at the Swiss Light Source. In the photon energy range 8.88 -10.25 eV, only one dissociation channel is observed, corresponding to the bromine loss. All three isomers, ortho-, para-, and meta- show a slow photodissociation. Breakdown diagrams and time-of-flight distributions are used to derive the 0 K appearance energies of the bromine loss dissociation channels. Along with literature thermochemical information known for the bromine atom and the daughter ion dissociating from the parent molecules, the heat of formation for the three cationic isomers is obtained.

*Corresponding author: gmeloni@usfca.edu

6.2 Introduction

Gasoline, a mixture of organic compounds resulting from the distillation of petroleum, is used for internal combustion engines in motor vehicles. As the global consumption of gasoline has increased every year for decades, it has become increasingly important to consider the effect that burning gasoline has on the global environment.[87] In 2015, motor vehicles produced more than 1.1 billion metric tons of CO_2 in the United States alone.[14] While the harmful atmospheric effects of CO_2 are well established, the burning of gasoline presents many other environmental and health concerns. It is only in recent years, however, that the United States government has begun to regulate the composition of gasoline.[88] For example, twenty years ago the United States banned leaded gasoline due to inhalation risk, the consequences of which have been known for decades.[88]

Additives such as lead have been added to gasoline to reduce engine knock, wherein excess fuel is prematurely ignited during the combustion cycle of an engine.[14] Gasoline is gauged on its anti-knock characteristics using an octane rating, comparing the fuel to a mixture of iso-octane and heptane with similar anti-knocking capacity.[89] A higher octane rating indicates gasoline's ability to withstand higher pressures, thereby mitigating knock. Yet, lead and other anti-knock additives have proven harmful to humans and the environment.[89] In recent years, other anti-knock additives of lower toxicity have been identified, such as ether, alcohols, and aromatic hydrocarbons.[90] The most promising of these additives, so far, have been aromatic hydrocarbons. Aromatic hydrocarbons have a high energy density and high octane ratings, making them attractive fuel additives because these properties help decrease engine knock.[31]

One of the difficulties in finding a better gasoline additive is balancing the anti-knock requirements against the potential health and environmental risks. Benzene is a natural component of petroleum and has a high octane rating. However, benzene alone is highly carcinogenic and harmful to the environment. In many countries, fuel compositions are now regulated to contain no more than 1% benzene. Toluene, also referred to as methylbenzene, is another often used additive in gasoline, but has a relatively low octane rating, prompting researchers to look for other aromatic hydrocarbons to be used as gasoline additives. Toluene is employed as a replacement for benzene because it is metabolized differently than benzene through its methyl side groups. It can reach a mol fraction of 10% in premium fuels compared to other aromatic compounds.[91-92] Next to benzene and toluene, different polyalkylated benzenes, which can form radicals quicker than benzene and are generally unreactive towards O_2, are used nowadays to increase antiknock properties and better the combustion of gasoline. Example are xylenes, trimethylbenzes, and ethylbenzenes.[93] The unreactive behavior of these species provides a higher chance of side reactions that may lead to forming polycyclic aromatic hydrocarbon (PAH) formation.[93] PAHs are a large class of aromatic molecules created from the burning of crude oil and gasoline and are the main source of the formation of particulate matter (PM) in the air. Soot is a substance of largely amorphous carbon atoms that

137

occurs through the incomplete burning of organic matter. Toluene pyrolysis, however, has been found to create radicals that can be further decomposed. It is important to study different aromatic hydrocarbon dissociations due to their role in the formation of PAHs.

Much research has been devoted into finding different additives that can lower the harmful effects of gasoline with elevated octane number. Increase in these numbers helps an engine with a high compression by keeping it from autoigniting.[94] As mentioned before, other promising additives are aromatics, such as xylene (methylbenzene) isomers due to their higher energy density and anti-knock rating. Meta-xylene and para-xylene have higher octane ratings than toluene and thus can be good replacements as fuel additives.[95] On the other hand, the octane rating of ortho-xylene is a full 25 points lower than meta- and para-xylyne.[96] The isomeric xylene compounds react differently in combustion and their decomposition has not been studied. Previous experiments were conducted in a shock tube in the temperature range of 1330-1800 K and no distinct differences were found regarding the xylene isomers autoigniton.[97] Several studies have been carried out to investigate the behavior of the xylyl isomer radicals since they are a key intermediate in the combustion behavior of xylenes.[98,99,100] The laminar burning velocities of the o- and p-xylyl radicals have similar behavior, however m-xylyl is much slower. The two similar radicals form a conjugated intermediate; however, it is not formed in the case for m-xylyl radical concluding that it is a very reactive free radical species.[98] Fernandes et al.[99] and da Silva et al.[100] further studied the behavior of the radical isomers and concluded that m-xylyl ionizes much slower and slowly undergoes a hydrogen abstraction thus it is harder to analyze than the other two. In a different study m-Xylyl bromide was also investigated to generate m-xylyl radical in a pyrolysis source.[98] The conclusions of this study were surprising in that m-xylylene was not identified, however, p-xylylene was the primary observed species.[98]

In the present investigation the photoionization and photodissociation of the ortho-, para-, and meta xylyl bromide isomers has been studied at the vacuum ultraviolet (VUV) beamline of the Swiss Light Source using Imaging Photoelectron Photoion Coincidence Spectroscopy (iPEPICO) as well as double Imaging Photoelectron Photoion Coincidence Spectroscopy (i^{2}PEPICO). Threshold photoelectron spectra of the decomposition of xylyl bromide isomers were analyzed and used to determine highly accurate dissociative photoionization onsets and explain the dissociation dynamics of internal energy selected gas phase ions.

6.3 Experiment

The experiments presented in this work are performed using the X04DB VUV beamline at the Swiss Light Source (Paul Scherrer Institute) in Villigen Switzerland. Ortho-xylyl bromide and para-xylyl bromide are measured using the double imaging photoelectron-photoion coincidence (i^{2}PEPICO) spectrometer. Meta-xylyl bromide is measured using the imaging photoelectron-photoion coincidence (iPEPICO)

spectrometer. These experimental apparatuses have been described in detail elsewhere and only a short description will be given here.[36,38,37,101]

Briefly, PEPICO is a versatile spectroscopic technique with which the internal energy of selected ions ($E_{internal}(AB^+)$) is measured through the time-of-flight mass spectra in coincidence with the kinetic energy of the electrons ($e^-(KE)$) presented in equation (1):

$$AB + h\nu \rightarrow E_{internal}(AB^+) + e^-(KE) - IE \tag{1}$$
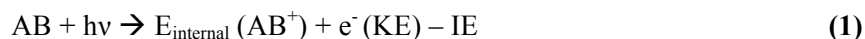
The iPEPICO and i^{2}PEPICO experiments are similar, except i^{2}PEPICO has a double imaging apparatus so that the imaging of both photoelectrons and photoions is performed simultaneously. The main purpose of these experiments is to study the unimolecular dissociation dynamics by creating selected ions with a specific internal energy. Both PEPICO experiments combine velocity map imaging (VMI) of the electrons along with Wiley McLarren time-of-flight (TOF) mass spectrometry.[37] The key feature of the iPEPICO experimental setup is small electric fields that enable to resolve threshold electrons up to 5 meV to measure unimolecular dissociations rate constants. iPEPICO is powerful in determining the thermochemistry of different ion cycles due to its highly accurate measurement of appearance energies (AE). i^{2}PEPICO is an improved apparatus based off of the experimental components of the iPEPICO endstation. This experimental set up allows for fast alignment along with grating change.[39] i^{2}PEPICO can be used in pyrolysis experiments to create radicals much quicker and from non-volatile solids.[39] Two fast position sensitive detectors detect in delayed coincidence the velocity map imaged photoelectron as well as the photoion.[39]

The three samples, meta-, ortho-, and para-xylyl (methylbenzyl) bromide are obtained from Sigma Aldrich with a purity of $\geq$ 99%. Without any further purification, the samples are placed into a temperature-controlled bubbler and their vapor is directly flowed into the reaction chamber, a resistively heated SiC reactor, from a 30 cm long 6 mm o.d. teflon tube through a 150 μm pinhole, where the pressure is maintained around 5.5-9.5 x 10^{-7} mbar using Argon as backing gas. The temperature of the gas samples is held at room temperature with the help of a lamp heating the needle valve. The interaction region is a 2 mm x 2 mm and the photon energy resolution is 3-5 meV.

Initially, a photoelectron is ejected and velocity map imaged onto a position-sensitive delay-line Roentdek DLD40 detector (1 meV kinetic energy resolution at threshold). Based off of lateral and axial velocity, threshold, energetic or hot electrons are separated. A constant electric field of 120 V cm^{-1} forces the photoelectrons and photoions to accelerate in opposite directions. The experimental time-of-flight (TOF) spectra generated experimentally are measured with the ejection of the photoelectron acting as the "start" signal. This is because the TOF of the electrons are shorter than the TOF of ions by three orders of

magnitude, thus the initial time of ionization is determined through the onset of electron detection. The lateral velocities of the photoelectrons throughout the experiments are separated with the use of the velocity map imaging. Threshold electrons consist of only axial velocity and are focused on the center spot of the detector. The mass spectrometer used to space focus and mass-analyze the photoions generated consists of a 5.5 cm long extraction, 1 cm long acceleration, and 55 cm long drift region that detects the ions with a non-imaging Jordan TOF C-726 microchannel place (MCP) detector (iPEPICO apparatus).[38] The relatively long extraction region of the TOF spectrometer correlates with the extraction field to allow ion residence times in microseconds that gives metastability to parent ions. Parent ions that are metastable can therefore dissociate in the extraction region and are detected between the parent and corresponding daughter ion time-of-flight yielding asymmetric peaks.[37,102,103,104]

The background-noise signal is subtracted from the intensity of the parent cation and fragment at the respective photon energy to generate a breakdown diagram, which is created through the fractional ion abundance in the threshold photoionization mass spectra as a function of photon energy. There are two types of dissociations that occur throughout these types of experiments: slow and fast. The 0 K appearance energy (AE) is obtained from fitting the statistical model of the breakdown diagram of fast dissociations or the breakdown diagram together with the time-of-flight distributions for slow dissociations. For fast reactions, there are no time-of-flight distributions analyses because the fractional ion abundance of the parent ion lowers as the photon energy goes up therefore the first daughter ion reaches 100%. In a fast dissociation this is referred as the photoionization threshold energy, E_0, in which 100% of the cation of the parent molecule dissociate.[105] In the case of slow dissociations not all of the parent ion has dissociated within the given time frame thus the TOF will exhibit an asymmetric fragment ion peak shape, the modeling of which will provide the absolute rate constants. This study observed slow dissociations of the three isomers.

6.4 Computational and Modeling

All quantum chemical calculations presented in this work are performed using Gaussian 09.[106] Rotational and vibrational constants, and zero-point corrected total electronic energies of the ionic and neutral species of the three isomers and the three isomeric dissociative fragments are computed. Using the B3LYP/6-31G(d) level of theory, different stationary points are found from the Synchronous Transit Guided Quasi-Newton (STQN) method.[57b] In order to determine the optimized energies and their relative energies, the G4 composite method is used.[107] It is the fourth in a series of Gx methods to calculate molecular energies through performing a series of molecular orbital calculations.[107] The level of theory used is the Møller-Plesset (MP) perturbation theory up to fourth-order in conjunction with coupled cluster theory.

The G4 method takes into account the extrapolation procedure to obtain the Hartree-Forck (HF) limit with a root mean squared error of 1.19 kcal/mol.[58]

Potential energy surfaces have been scanned using the B3LYP/6-31G(d) level of theory and basis set in order to visualize and determine whether the bromine loss from the three isomeric compounds has a reverse barrier for dissociation.[108-109] In these experiments the Br loss from the isomeric compounds is a slow dissociation leading to a kinetic shift. When the parent molecule is not fully dissociated within the original time scale of the experiment a kinetic shift occurs experimentally.

The studied processes can be summarized concisely in the following reaction

$$AB + h\nu \rightarrow AB^+ \rightarrow A^+ + B \tag{2}$$

where the neutral molecule AB is ionized (AB^+), and consequently dissociated into a daughter ion (A^+) and a neutral fragment (B). The formed daughter ion is the species that has the lowest ionization energy. The AE of the daughter ion is found through the miniPEPICO program[66] and is used in determining the thermochemistry. The appearance energy can also be calculated theoretically through the adiabatic ionization energy and bond dissociation energy (BDE) of the daughter ion and neutral fragment if no reverse barrier for dissociation is present. In the case where there is no barrier, the energy needed to form the daughter ion can be computed using the following equation:

$$AE = AIE + BDE = \Sigma E_{fragments} - E_{neutral\ parent} \tag{3}$$

The bond dissociation energy can be added to the adiabatic ionization energy to find the appearance energy of the daughter ion. From the appearance energy along with literature heat of formation of the neutral fragment and daughter ion, thermochemical information for the cationic and neutral parent can be determined.[61,110,111]

$$AE - AIE = BDE_{0K}^0(x - C_8H_9^+ - Br) \tag{4}$$

$$BDE_{0K}^0(x - C_8H_9^+ - Br) = \Delta_f^0 H\ (Br) + \Delta_f^0 H\ (C_8H_9^+) - \Delta_f^0 H\ (x - C_8H_9Br^+) \tag{5}$$

$$\Delta_f^0 H(x - C_8H_9Br^+) = \Delta_f^0 H(Br) + \Delta_f^0 H(x - C_8H_9^+) - BDE_{0K}(x - C_8H_9^+ - Br) \tag{6}$$

$$\Delta_f^0 H\ (x - C_8H_9Br) = \Delta_f^0 H(x - C_8H_9Br^+) - AIE \tag{7}$$

The x in the previous equations represents the specific isomer of the xylenes bromide, i.e., ortho- (o-), meta- (m-), or para- (p-).

In this work, the enthalpies of formation of the dissociative neutral fragment and cationic daughter ion are taken from previous studies and helped to determine the unknown heats of formation of the three isomeric cation compounds.[72,63,112] The enthalpy of formation is solved for the unknown using the bond dissociation energy calculation for the cationic reactant from the appearance energy of the daughter ion and the adiabatic ionization energy. Finally, the enthalpy of formation of the neutral isomers can be calculated using the measured adiabatic ionization energy and the obtained enthalpy of formation of the cation isomers. The relative energies of the three isomeric compounds and their relative cationic fragments are calculated using the G4 composite model.

The MiniPEPICO program models a breakdown diagram of the experimental data to obtain the most accurate AE of the daughter ion. The electronic structure calculations results (rotational constants and vibrational frequencies) described in the computational section of this work are entered into the program to calculate the thermal energy distribution of the neutral and daughter ions. There are two types of dissociations that might occur throughout these types of experiments: slow or fast. In this work, the dissociation of all three isomers is slow. For slow dissociations, the miniPEPICO program uses the Rigid Activated Complex (RAC-) RRKM theory to model the dissociation rates.[67,70,71] The rate constants in PEPICO experiments are a function of internal energy:

$$k(E) = \frac{\sigma N^{\mp}(E-E_0)}{\hbar \rho(E)} \tag{4}$$

where $N^{\mp}(E - E_0)$ represents the number of states of the transition state that are in excess energy above the barrier E_0, $\rho(E)$ is the density of the states, $\hbar$ is Planck's constant, and σ represents the symmetry number of the TS.[23,27, 69,57b, 99, 109] The slope of the breakdown diagram, provides a visual whether a dissociation is fast or slow and is further determined through the TOF distributions. A slow dissociation means that the daughter ion or ions have never fully dissociated from the parent molecule within the given time frame, also causing kinetic shifts as mentioned above. In this work, bromine slowly dissociates from the three cationic isomers. In this case, it is important to fit the breakdown diagram to the time-of-flight distributions.

6.5 Results

For ortho-xylyl bromide the experiment is performed at room temperature and data is collected in the 8.49-12.0 eV range, 8.45-14.0 eV range for para-xylyl bromide, and 8.50-10.25 eV range for meta-xylyl bromide using a 120 V cm^{-1} constant extraction field. The general dissociative photoionization scheme is observed in Scheme 1 for all three isomers.
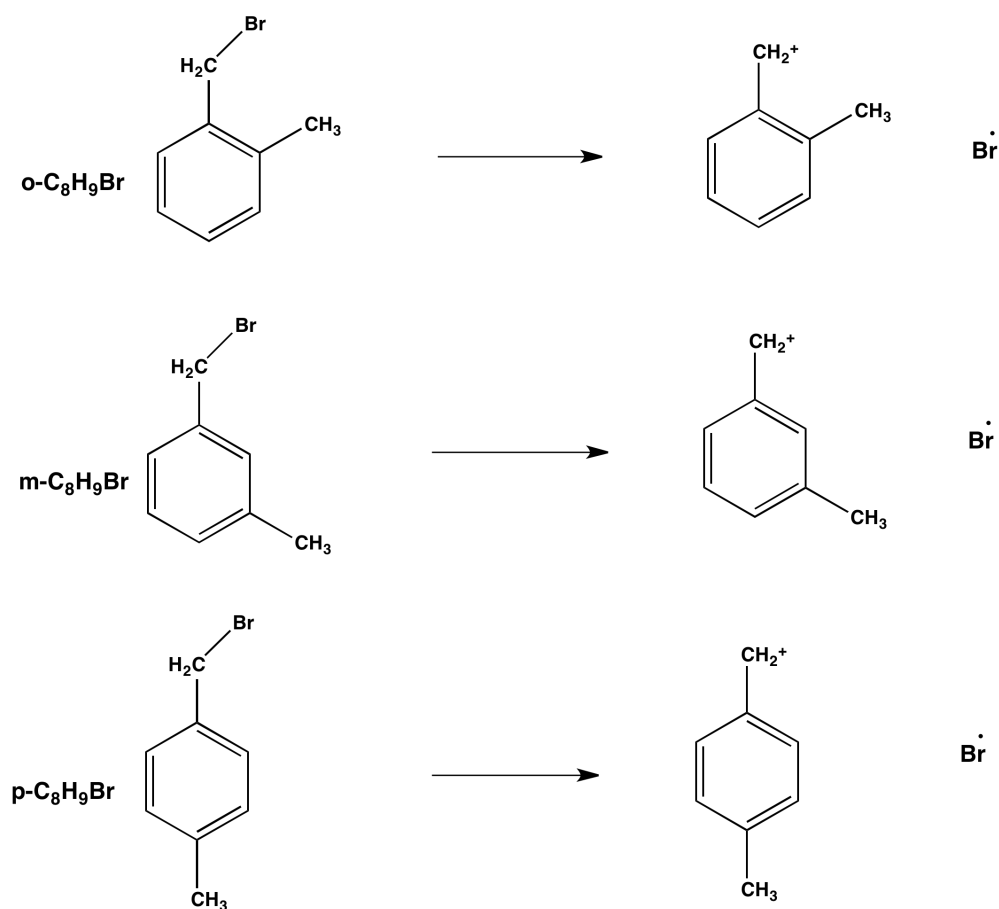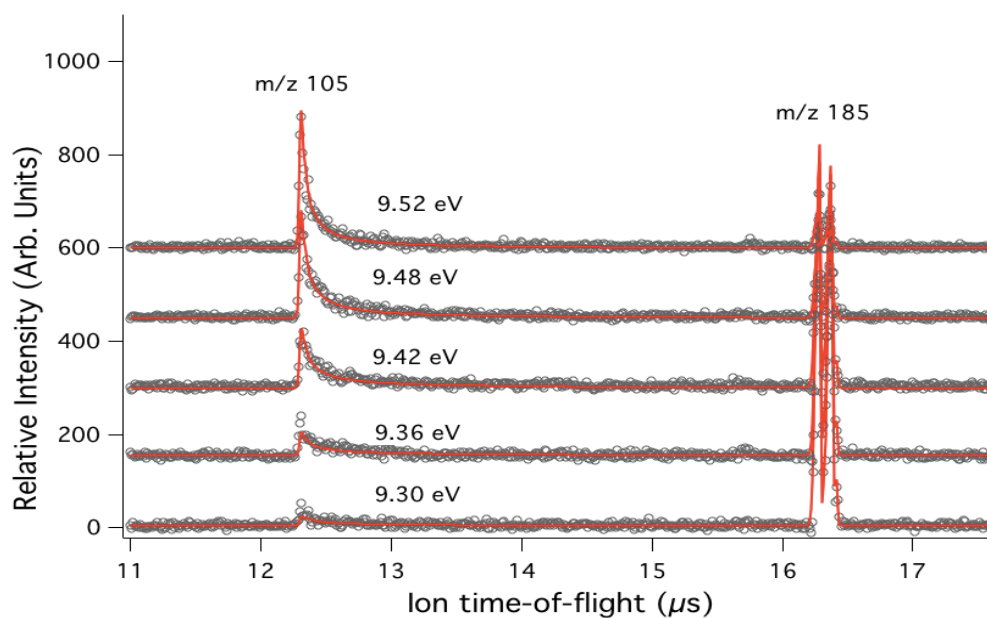
Scheme 1. Dissociative Photoionization Scheme for the xylyl bromide isomers at 298 K.

The breakdown diagram for o-xylyl bromide is shown within the photon energy range of 8.8-10.2 eV (Figure 1a). In order to calculate the density state of the ion and transition state, the frequencies and rotational constants of the optimized geometries of the parent and cation of o-xylyl bromide are used. The obtained 0 K appearance energy for the Br loss from o-xylyl bromide is 9.50 $\pm$ 0.025 eV with a kinetic shift of ~588 meV. The $C_8H_9^+$ time-of-flight is asymmetric as the parent peak at 16-17 μs indicating a slow dissociation, specifically the rate constant lies between 1.0 x 10^9 s^{-1}, with a kinetic shift. The time-of-flight data for o-xylyl bromide within the 9.30-9.52 eV photon energy range is shown in Figure 1b. Since, the dissociation is slow, the states ion density depends on the ion internal energy as a function of the ionization energy. The two asymmetric peaks correspond to ^{79}Br and ^{81}Br parent isotopologues. From the B3LYP calculations, the bromine loss does not have a barrier. The temperature at which the fit is done is 290 K.
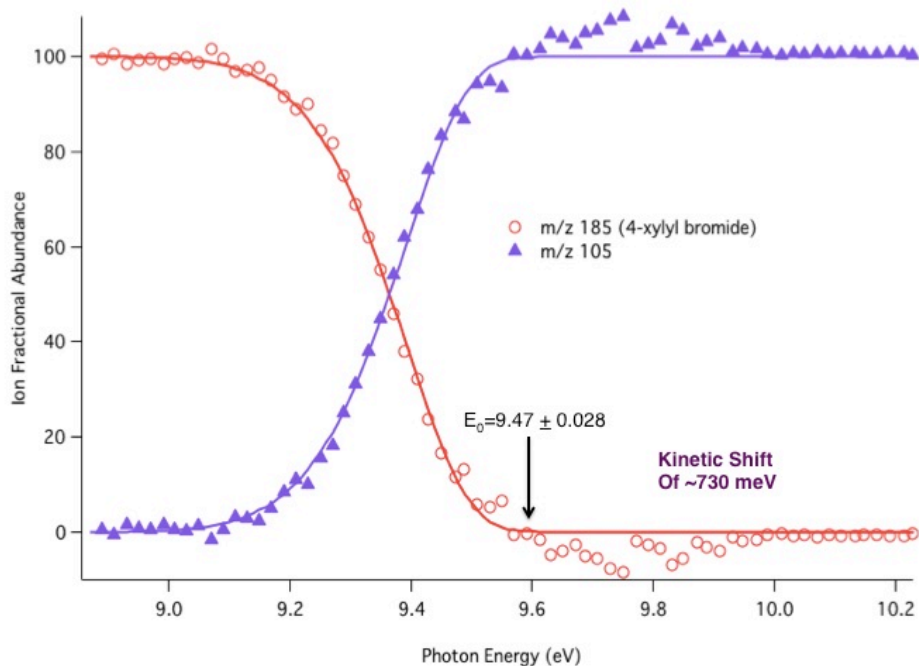
(a)
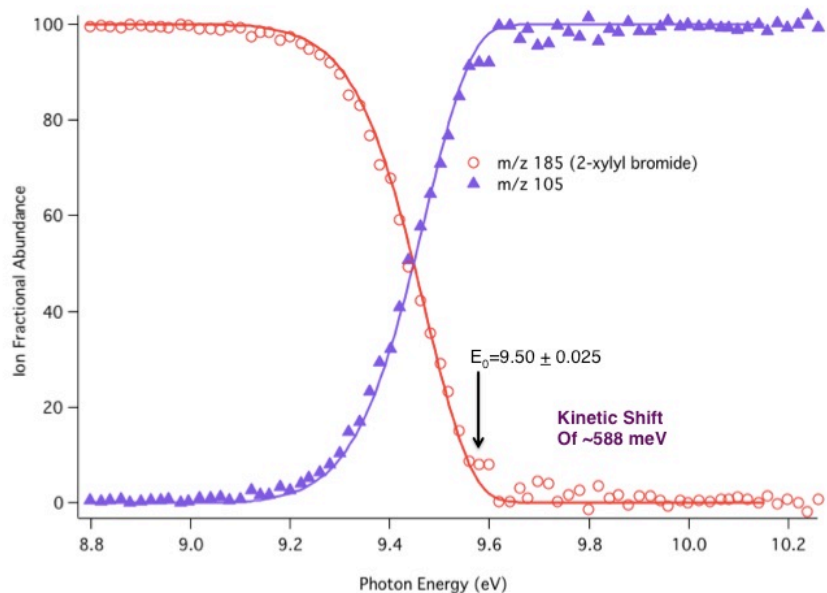
(b)

Figure 1. (a) Breakdown diagram showing the bromine loss in the dissociative photoionization of o-xylyl bromide. The red open circles represent the experimental dissociation of o-xylyl bromide and red solid line represents the calculated miniPEPICO dissociation. The filled purple triangles represent the appearance of $C_8H_9^+$ daughter ion along the calculated purple solid line. (b) Time-of-flight distributions for o-xylyl bromide in the vicinity of the bromine loss onset. The open grey circles represent the experimentally measured ion abundances and the solid red line represents the best fit modeled in the miniPEPICO program.

144

The dissociation of p-xylyl bromide is similar to o-xylyl bromide. The breakdown diagram is presented within the photon energy range of 8.81-10.25 eV (Figure 2a). In this case the temperature used for the fitting is relaxed to 310 K in order to obtain the best fit of the time-of-flight distributions in reference to the dissociation of the breakdown diagram. The time-of-flight spectra for p-xylyl bromide are collected in the photon energy range of 9.29-9.55 eV also using the i^2PEPICO instrument. Once again, the two parent isotopologues (m/z 184 and m/z 186) are detected in the time-of-flight range of 14-15 μs, indicating that the $C_8H_9^+$ ion appears slowly. The daughter ion, $C_8H_9^+$ (m/z 105), is highly metastable and it is detected in the range of 11-12 μs, the rate constant from the specified photon energy range lie between 1.0×10^{-9} s^{-1} (Figure 2b). The 0 K appearance energy of the p-$C_8H_9^+$ ion is 9.47 ± 0.028 eV with a kinetic shift of ~730 meV.
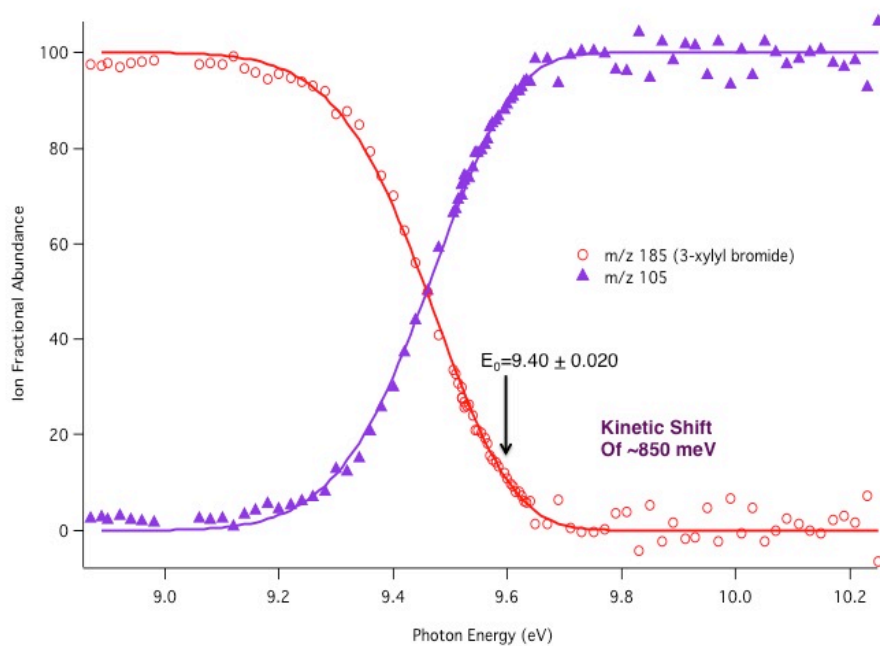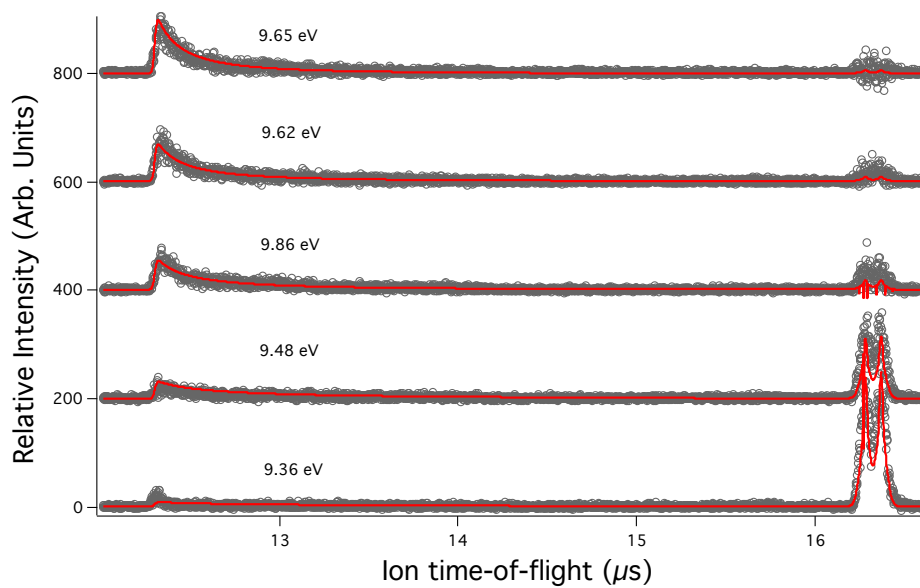
(a)

(b)
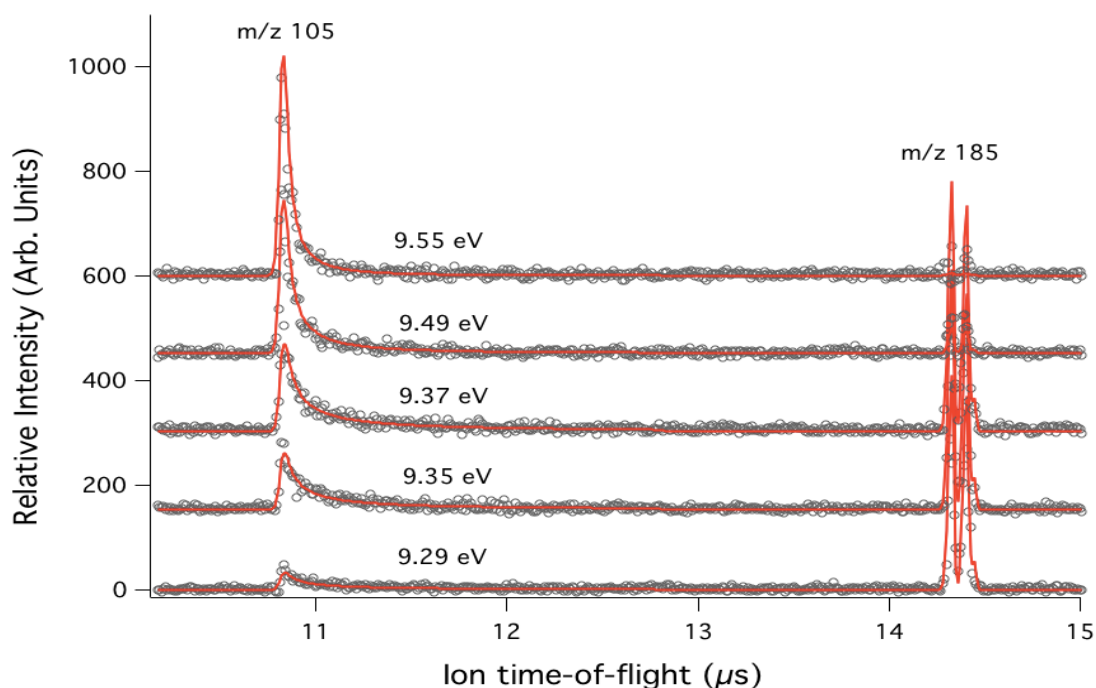
Figure 2. (a) Breakdown diagram showing the bromine loss in the dissociative photoionization of para-xylyl bromide. The red open circles represent the experimental dissociation of p-xylyl bromide and red solid line represents the calculated miniPEPICO dissociation. The filled purple triangles represent the appearance of $C_8H_9^+$ daughter ion along the calculated purple solid line. (b) Time-of-flight distributions for p-xylyl bromide in the onset of the dissociation. The metastable parent peaks and asymmetric daughter ion indicate a slow dissociation. The open grey circles represent the experimentally measured ion abundances and the solid red line represents the best fit modeled in the miniPEPICO program.

m-Xylyl bromide is measured using iPEPICO. This experimental data is also taken at room temperature. The photon energy range is from 8.87 to 10.25 eV represented in Figure 3a, where the rate constant lies begins at $1x10^{-9}$ s^{-1}. The TOF distributions are asymmetric, indicating a slow dissociation similar to the other two isomers as well. Previous studies proved that indeed it is a more stable free radical species, which confirms the results of this study.[98,99,100] The TOF distributions presented in Figure 3b are fitted in the energy range of 9.3-9.7 eV. The 0 K AE of the m- $C_8H_9^+$ ion is derived as 9.450$\pm$ 0.020 eV with a kinetic shift ~850 meV.

a)

b)

Figure 3. (a) Breakdown diagram showing the bromine loss in the dissociative photoionization of meta-xylyl bromide. (b) Time-of-flight distributions for m-xylyl bromide in the onset of the dissociation. The metastable parent peaks and asymmetric daughter ion indicate a slow dissociation.

147

A summary of the computed AIE and AE of the daughter ion formation from the three neutral isomers is presented in Figure 4. Although the daughter ion formation is established, the decomposition of the xylyl bromide isomers could also form the methyl-tropylium ion with an appearance energy comparable to the experimental values. However, the transition state barrier to form this ion is too high to be considered. In Scheme 2 a), the decomposition of o-xylyl bromide is presented, the reactive intermediate has an AE of 9.46 eV but the first transition state barrier TS1 is 10.20 eV and TS2 is 10.25 eV. These barriers are too high to actually form the tropylium ion and intermediate.
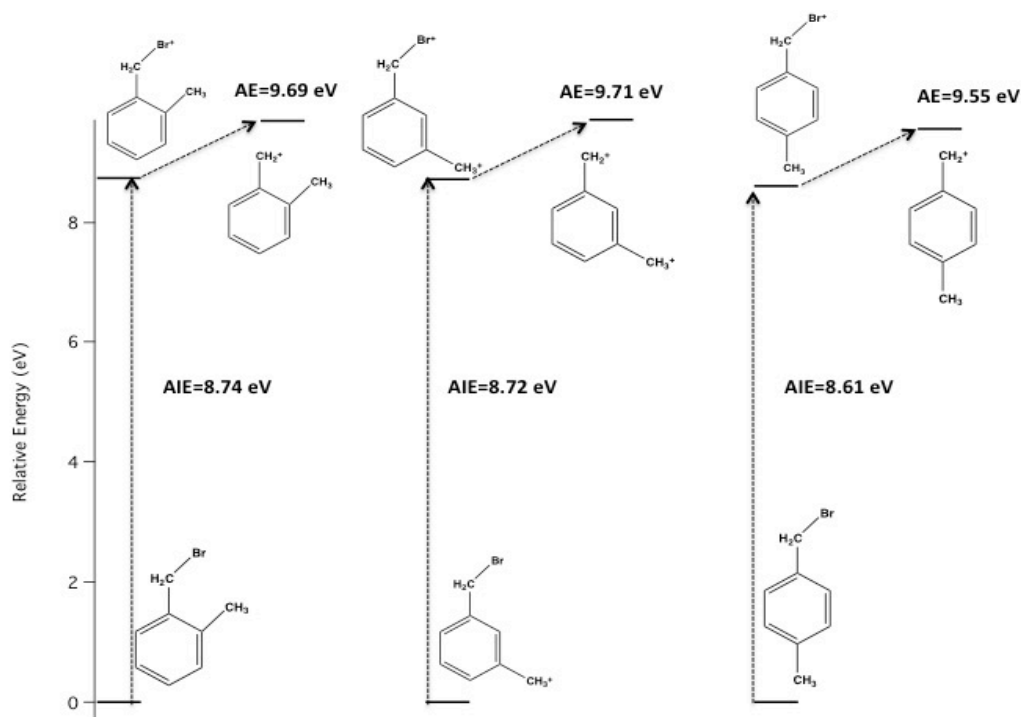

Figure 4. Energy diagram that represents the AIE of neutral and cationic isomers and the AE of the three daughter ions that form throughout this work.

The other two isomers have similar appearance energies and transition state barriers for the formation of the methyl-tropylium. For m-xylyl bromide reactive intermediate the TS1 barrier is at 10.19 eV and the TS2 at 10.20 eV, although the appearance energy of the reactive intermediate is 9.56 eV (Scheme 2 b)). For p-xylyl bromide, two reactive intermediates form with the same appearance energy, 9.56 eV and the same transition state barrier (Scheme 2 c)). These results can rule out the possibility of the formation of the tropylium ion.
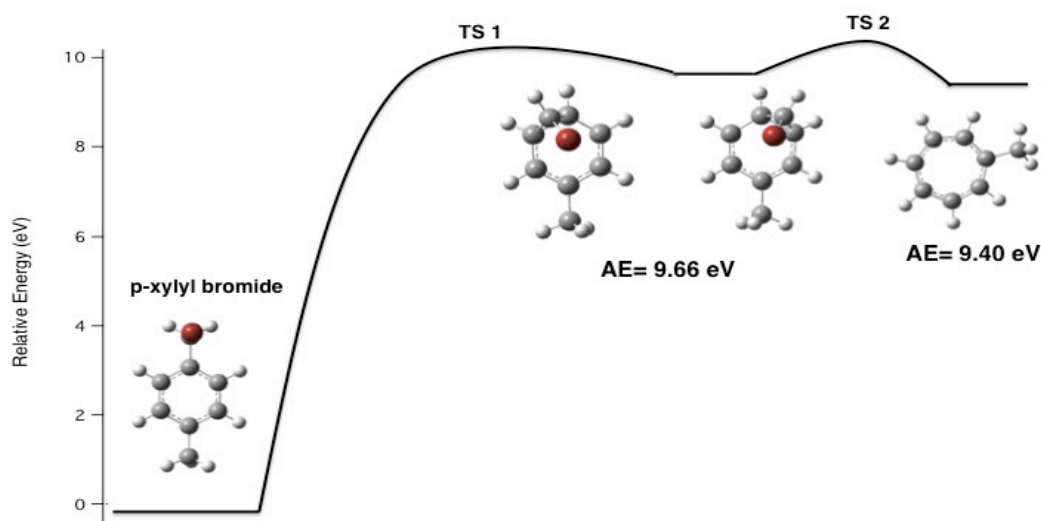
a)

b)

149
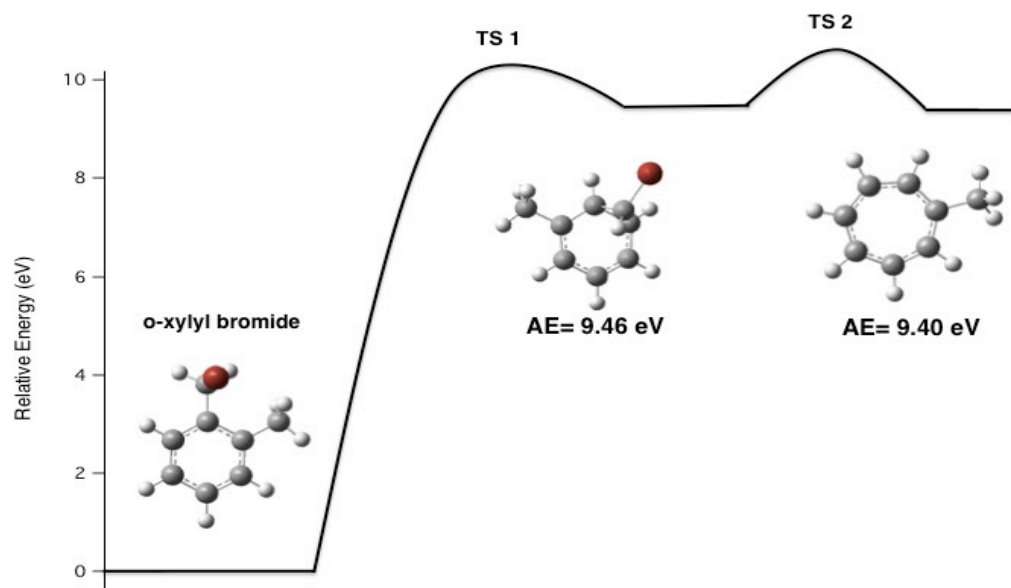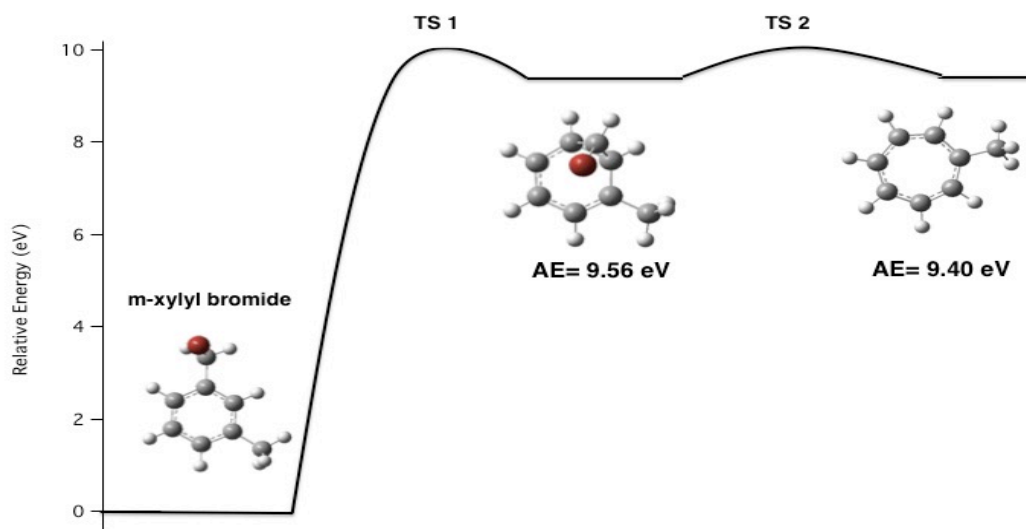
c)

Scheme 2. Dissociative Photoionization Scheme for the a) o-xylyl bromide b) m-xylyl bromide and c) p-xylyl bromide to form the methyl-tropylium ion.

6.6 Thermochemistry

In order to determine the enthalpies of formation for neutral isomeric species, the available thermochemical data of the bromine atom and $C_8H_9^+$ ion (o-, m-, and p-) are used. The enthalpy of formation of the Br fragment published by NIST-JANAF[113] thermochemical data is 117.92 ± 0.06 kJ/mol at 298.15 K and 111.86 ± 0.06 kJ/mol at 0 K.

Hayashibara[114] reported the heat of formation for o-xylyl ion as 849 ± 0.84 kJ/mol at 298.15 K. The set of equations (4) – (7) presented in the Computational and Modeling part are used in order to obtain the enthalpy of formation of the compounds under study. For ortho-xylyl bromide, the calculated BDE^o_{0K} is 0.95 eV. Along with the thermochemical data known from the daughter ion and bromine fragment, the calculated bond dissociation energy is used to find the Δ_f^0H (RX$^+$) = $966 + 5.0$ kJ/mol. The adiabatic ionization energy of ortho-xylyl bromide is subtracted from the Δ_f^0H (o-$C_8H_9Br^+$), to calculate the Δ_f^0H (o-C_8H_9Br)= 957 ± 7.0 kJ/mol.

The reported heat of formation at 298.15 K for para-xylyl ion is 837 ± 0.84 kJ/mol.[44] The calculated BDE^o_{0K} of 0.94 eV is used to determine the Δ_f^0H (p-$C_8H_9Br^+$) to be 954 ± 5.0 kJ/mol. Following the same pathway as ortho-xylyl bromide, the heat of formation of the neutral para-xylyl bromide species is derived as Δ_f^0H (p-C_8H_9Br) = 945 ± 7.0 kJ/mol.

The reported heat of formation at 298.15 K for meta-xylyl ion is 854 ± 0.84 kJ/mol.[44] The calculated BDE^o_{0K} of 0.99 eV is used to determine the $\Delta_f^0 H$ (p-$C_8H_9Br^+$) to be 971 ± 5.0 kJ/mol. Following the same pathway as mentioned above, $\Delta_f^0 H$ (m-C_8H_9Br) = 962 ± 7.0 kJ/mol.

6.7 Conclusions

The unimolecular dissociation of C_8H_9Br isomers was investigated using iPEPICO for meta-xylyl bromide and i²PEPICO for ortho- and para-xylyl bromide. These experiments are known for finding accurate appearance energies. Accurate dissociation onset of Br- loss from all three isomers forming the isomeric daughter ions are obtained through these experiments. The results also show slow photodissociations for all three isomers. The 0 K appearance energy of o-xylyl daughter ion is 9.50 ± 0.025 eV, which is used to find the $\Delta_f^0 H$ (o-C_8H_9Br) to be 311 ± 4.0 kJ/mol. The heat of formation is computed using the literature values of the heat of formation of the o-,p-, and m- isomers as well as the bromine neutral species. For p-xylyl bromide the 0 K appearance energy of the daughter ion is 9.47 ± 0.028 eV, which is used to compute the heat of formation 309 ± 3.5 kJ/mol. Lastly, for m-xyly bromide the heat of formation was calculated to be 314 ± 4.4 kJ/mol using the 0 K appearance energy of the daughter ion 9.450 ± 0.020 eV.

6.9 References

1.   (a) Agency, U. E. P., Gasiline Sulfur & Benzene Credits. **August 16, 2016**; (b) Business, I. C., Benzene and Tolune Market Update **July 3 2015**.
2.   Ronald F. Colwell, P. E., Benzene in Gasoline.
3.   Canada, E. et al. Benzene in Gasoline Regulations. **12-16-2015**.
4.   Piparelli, R. Anti-Knock Agent and Fuel Additves. *3rd Word Petroleum Congress* **1951**.
5.   Boundless, Properties of Aromatic Compounds. **Sep 2016**.
6.   ExxonMobil, Hydrocarbon & Oxygenated Fluids.
7.   Humerm S.; Frassoldati, S.; Granata S. Faravelli, T. Ranzi E. Seiser R. Seshadri, K., Experimental and kinetic modeling study of combustion of JP-8, its surrogates and reference components in laminar nonpremixed flows. *Proc. Combust. Inst.* **2007,** *31*, 393-400.
8.   Yahyaoui, M.; Djebaili-Chaumeix, N.; Dagaut, P.; Paillard, C.-E. Gail, S. Experimental and modelling study of gasoline surrogate mixtures oxidation in jet stirred reactor and shock tube. *Proc. Combust. Inst.* **2007,** *31*, 385-391.
9.   Hemberger, P.; Trevitt, A. J.; Gerber, T.; Ross, E.; da Silva, G. Isomer-specific product detection of gas-phase xylyl radical rearrangement and decomposition using VUV synchrotron photoionization. *J. Phys. Chem. A* **2014,** *118* (20), 3593-   604.
10.   Lores, M. T.; de la Torre, J.; Burguet, M. C.; Montón, J.B., Vapor−Liquid Equilibria for the Binary Systems Isobutanol with m-Xylene, o-Xylene and p-Xylene at 101.3 kPa. *J. Chem. Eng. Data* **1999,** *44* (4), 869-872.
11.   Farmer, J. B. L., F. P.; Marsden, D. G. H.; McDowell, C.A., Free radicals by mass spectrometry. VIII. The ionization potentials of p-, o-, and m-xylyl radicals. *J. Chem. Phys.* **1956,** *24*, 52-55.
12.   Farmer, J. B.; Marsden, D. G. H.; Lossng, F. P. , Thermal Stability of o-,p-,m-xylyl radicals and the formation of quinodimethans. *J. Chem. Phys.* **1955,** *23*, 403-404.
13.   Battin-Leclerc, F.; Bouncaceuer, N.; Glaude, P. A. Experimental and modeling study of the oxidation of xylenes. *Int. J. Chem. Kinet.* **2006,** *38*, 284-302.
14.   Hemberger, P.; Trevitt, A. J.; Ross, E.; da Silva, G. Direct Observation of para-Xylylene as the Decomposition Product of the meta-Xylyl Radical Using VUV Synchrotron Radiation. *J. Phys. Chem. Lett.* **2013,** *4*, 2546-2550.
15.   Fernandes, R. X.; Gebert, A.; Hippler, H. The pyrolysis of 2-,3-, and 4-methylbenzyl radicals behind shock waves. *Proceed. Combust. Inst.* **2002,** *29*, 1337-1343.
16.   da Silva, G.; Moore, E. E.; Bozzelli, J. W. Decomposition of Methylbenzyl Radicals in the Pyrolysis and Oxidation of Xylenes. *J. Phys.Chem.* **2009,** *113* (38), 10264-10278.
17.   Johnson, M.; Bodi, A.; Schultz, L.; Gerber, T. Vacuum Ultraviolet Beamline at the Swiss Light Source for Chemical Dynamics Studies. *Nuclear Instrumentaion Methods* **2009,** *610*, 597-603.
18.   Bodi, A.; Sztaray, B.; Baer, T.; Johnson, M.; Gerber, T. Data acquisition schemes for continuous two-particle time-of-flight coincidence experiments. *Rev. Sci. Instrum.* **2007,** *78* (8), 084102/1-084102/7.
19.   Bodi, A.; Johnson, M.; Gerber, T.; Gengelliczki, Z.; Sztaray, B.; Baer, T. Imaging photoelectron photoion coincidence spectroscopy with velocity focusing electron optics. *Rev. Sci. Instrum.***2009,** *80* (3), 034101/1-034191/7.
20.   Bodi, A.; Hemberger, P.; Osborn, D. L.; Balint, S. Mass-Resolved Isomer-Selective Chemical Analysis with Imaging Photoelectron Photoion Coincidence Spectroscopy. *J. Phys. Chem. Lett.* **2013,** *4* (17), 2948-2952.

21.   Bodi, A.; Hemberger, P.; Gerber, T.; Sztaray, B. A new double imaging velocity focusing coincidence experiment: i²PEPICO. *Rev. Sci. Instrum.* **2012,** *83* (8), 083105/1-083105/8.

22.   Sztaray, B.; Baer, T. Suppresion of hot electrons in threshold photoelectron photoion coincidence spectroscopy using velocity focusing optics. *Rev. Sci. Instrum.* **2003,** *74* (8), 3763-3768.

23.   Voronova, K.; Mozaffari Easter, C. M.; Covert K. J.; Bodi, A.; Hemberger, P.; Sztaray, B. Dissociative Photoionization of Diethyl Ether. *J. Phys. Chem. A* **2015,** *119* (43), 10654-10663.

24.   Wiley, W. C., McLaren, I. H. Time-of-flight mass spectrometer with improved resolution. *Rev. Sci. Inst.* **1955,** *26*, 1150.

25.   Winfough, M.; Voronova, K.; Muller, G.; Laguisma, G.; Sztaray, B.; Bodi, A.; Meloni, G. Furfural: The Unimolecular Dissociative Photoionization Mechanism of the Simplest Furanic Aldehyde. *J. Phys. Chem. A* **2017,** *121* (18), 3401-3410.

26.   Frisch, M. J., et al. Gaussian 09. *Gaussian Inc. Wallingford, CT* **2009**.

27.   Montgomery, J. A. Jr.; Frisch, M. J.; Ochterski, J. W.; Petersson, G. A., A complete basis set model chemistry. VI. Use of density functional geometries and frequencies. *J. Chem. Phys.* **1999,** *110* (6), 2822-2827.

28.   Curtiss, L. A.; Redfer, P. C.; Raghavachari, K. Assessment of Gaussian-3 and Density Funcitonal Theories on the G3/05 Test Set of Experimental Energies. *J. Chem. Phys.* **2005,** *123*, 12.

29.   Curtiss, L. A.; Redfern, P. C.; Raghavachari, K. Gaussian-4 Theory. *J. Chem. Phys.* **2007,** *126*, 084108.

30.   Pend, C. et al. Using redundant internal coordinates to optimize equilibrium geometries and transition states. *J. Comput. Chem.* **1998,** *17* (1), 49-56.

31.   Beynon, J. H.; Gilbert, J. R. Application of transition state theory to unimolecular reactions: An Introduction. *Wiley Interscience, Chister* **1984**.

32.   Sztaray, B.; Bodi, A.; Baer, T., Modeling unimolecular reactions in photoelectron photoion coincidence experiments. *J. Mass Spect.* **2010,** *45*, 1233-1245.

33.   Baer T.; Bodi, A.; Satzaray, B. Photoelectron-Photoion Coincidence Methods in Mass Spectrometry (PEPICO). *Eslevier Reference Module in Chemistry, Molecular Science and Chemical Engineering.* **2014**.

34.   Harvey, J. et al. Dissociation Dynamics of fluorinated ethene cations: from time bombs on a molecular level to double-regime dissociators. *Phys. Chem. Chem. Phys.* **2012,** *12*, 3935-3948.

35.   Gengelicski, Z. B., S.N.; Sztaray, B, Dissociation of Energy-Selected 1,1-Dimethylhydrazine Ions. *J. Phys. Chem.* **2010,** *114*, 6103-6110.

36.   Borkar, S. N. Very Accurate Gas-Phase Thermochemistry Through Photoelectron Photoion Coincidence (PEPICO) Spectroscopy. *Chemistry, University of the Pasicifc, Stockton, California* **2013**.

37.   Shuman, N. et al. Heat of formation of the allyl ion by TPEPICO spectroscopy. *J.Phys. Chem.* **2009,** *113* (40), 10710-10716.

38.   Chase, M. W. J. NIST-JANAF Thermochemical Tables, Fourth Edition. *J.Phys. Chem.* **1998,** *Reference Data*, 1-1951.

39.   Marcus, R. A.; Rice, O. K. The kinetics of the recombination of methyl radicals and iodine atoms. *J. Phys. Chem.* **1951,** *55*, 894.

40.   Rice, O. K.; Ramsperger, H. C. Theories of unimolecular reactions at low pressures II. *J. Ame. Chem. Soc.* **1927,** *49* (1617).

41.   Rice, O. K.; Ramsperger, H. C. Theories of unimolecular reactions at loew pressures II. *J. Ame. Chem. Soc.* **1928,** *50*, 617.

42.   Baer, T.; Hase, W. L. Unimolecular Reaction Dynamics: Theory and Experiments. *Oxford University Press. New York* **1996**.

44.   Hayashibara, K. K., G. H.; Beauchamp, J. L. Photoelectron spectroscopy of the o-,m- and p-methylbenzyl radicals. Implication for the thermochemistry of the radicals and ions. *J. Ame. Chem. Soc.* **1986,** *108* (18), 5441-5443.